SIMULATION AND MECHANICAL ANALYSIS OF THE CROSS-WEDGE ROLLING PROCESS

A Thesis Submitted to
the Graduate School of Engineering and Sciences of
İzmir Institute of Technology
in Partial Fulfillment of the Requirements for the Degree of

MASTER OF SCIENCE

in Mechanical Engineering

by
Metin ÇAKIRCALI

June 2010
İZMİR

We approve the thesis of **Metin ÇAKIRCALI**

Prof. Dr. Mustafa GÜDEN
Supervisor

Assoc. Prof. Dr. Bülent YARDIMOĞLU
Committee Member

Assoc. Prof. Dr. Hasan YILDIZ
Committee Member

25 June 2010

Prof. Dr. Metin TANOĞLU
Head of the Department of
Mechanical Engineering

Assoc. Prof. Dr. Talat YALÇIN
Dean of the Graduate School of
Engineering and Sciences

ACKNOWLEDGMENTS

I would like to express my great gratitude to my supervisor, Prof. Dr. Mustafa GÜDEN. His patience, knowledge, and constant support added considerably to my graduate experience.

I also wish to express my appreciation to “The Scientific and Technological Research Council of Turkey” for the scholarship granted during my study, and for funding the present thesis (Grant no.: 107M628) and a short-term visit to Republic of Belarus. Furthermore, I must acknowledge “The Physical-Technical Institute of the National Academy of Sciences of Belarus” for carrying out the experiments and their hospitality.

Finally, my sincere gratitude to my family for their endless love and support throughout my life, I acknowledge a debt, an appreciation, that extends beyond any words at my command. This thesis could not have been accomplished without them.

ABSTRACT

SIMULATION AND MECHANICAL ANALYSIS OF THE CROSS-WEDGE ROLLING PROCESS

The effect of process parameters including forming angle, stretching angle, area reduction and friction coefficient on the cross-wedge rolling (CWR) of AISI 1045 steel and Ti6Al4V alloy workpiece was investigated numerically using thermo-mechanical model analysis. The numerical simulations were further validated experimentally. The thermo-mechanical analysis showed the general trends of the variations of the temperature, effective strain and stress, maximum principal stress, mean stress, stress triaxiality and strain rate of the workpiece during high and low temperature CWR process. The temperature distribution in the workpiece was shown to be non-uniform during CWR process. When the initial temperature of the workpiece was relatively low, the workpiece temperature increased, a heating effect of the plastic deformation, while higher initial temperatures caused the cooling of the workpiece. The most significant process parameters on the deformation of the workpiece in CWR were shown, for the studied range of parameters, to be the area reduction and stretching angle. Both were found to increase the tool forces. The friction coefficient between tool and workpiece was found not to affect the workpiece deformation significantly after a value of 0.3. The failure in CWR was shown to occur numerically in the midsections of the workpiece, where the stress triaxiality was maximum. The determined cruciform shaped crack also agreed with the experimentally observed crack shape. Finally, it was shown that the final microstructure of the workpiece was greatly affected by the workpiece initial temperature.

ÖZET

ÇAPRAZ KAMA HADDELEME İŞLEMİNİN SİMÜLASYONU VE MEKANİK ANALİZİ

AISI 1045 çeliği ve Ti6Al4V alaşımı iş parçalarının çapraz kama haddeleme (ÇKH) işlemi üzerindeki şekillendirme açısı, açma açısı, alan redüksiyon ve sürtünme katsayısı işlem parametrelerinin etkileri ısıl-mekanik model analiziyle nümerik olarak araştırılmıştır. Yapılan nümerik analizler ayrıca deneysel olarak doğrulanmıştır. İş parçasının düşük ve yüksek sıcaklıklarda ÇKH işlemi sırasındaki sıcaklık, efektif birim şekil değişimi, efektif gerilim, maksimum temel gerilim, ortalama gerilim, gerilim üç-eksenliği (stres triaxiality) ve birim şekil değişim hızı değişimi genel eğilimleri ısıl-mekanik analizle belirlenmiştir. İş parçası üzerindeki sıcaklığın işlem sırasında homojen olarak dağılmadığı gösterilmiştir. Düşük sıcaklıkta yapılan ÇKH işleminde iş parçası sıcaklığı artarken yüksek sıcaklıkta yapılan işlemde iş parçası sıcaklığı düşmektedir. Çalışılan parametre aralığı için en etkin işlem parametreleri alan redüksiyon ve açma açısıdır. Her iki parametrenin artışı da kalıp kuvvetlerinin yükselmesine sebep olmaktadır. Sürtünme katsayısının 0,3'ün üzerine çıktığı durumda iş parçası deformasyonuna olan etkisinin önemsiz olduğu bulunmuştur. Gerilim üç-eksenliliğinin en yüksek olduğu iş parçası orta kesitinde kırılma gerçekleştiği nümerik olarak gösterilmiştir. Çapraz biçimli kırılma şekli deneysel olarak gözlenen kırılma şekli ile örtüşmektedir. Son olarak, iş parçası mikroyapısının ilk işlem sıcaklığı tarafından etkilendiği gösterilmiştir.

TABLE OF CONTENTS

LIST OF FIGURES

LIST OF TABLES

CHAPTER 1

INTRODUCTION

The Cross-Wedge Rolling (CWR) is a plastic forming process, in which a cylindrical workpiece is formed into stepped rotational parts between two wedge type tools moving tangentially relative to the workpiece. The wedge tools assembled on rolls, called roll CWR, or on a plate, called flat CWR, deform the workpiece plastically usually at an elevated temperature. Finite Element Model (FEM) analyses were previously performed in order to understand the relations between the process geometrical parameters and the deformation and failure of the workpiece in the CWR process. An explicit FEM analysis showed that the interfacial slip between workpiece and tools increased with increasing durations of the forming process and at smaller frictional coefficients (μ), larger forming angles (α) and smaller area reductions (Δ_A) [1-3]. Furthermore, a positive first principal stress was numerically shown to exist at the center of the workpiece throughout the rolling process, while the stress at the mid-radius showed cyclic variation, leading to axial annular cracks and well-known Mannesmann effect due to low cycle fatigue [4]. The stress and strain values were shown to increase with increasing the area reduction and not to be sensitive to μ when μ=0.3 [4]. Using experimentally verified FEM analysis results, it was further shown that the effective plastic strain was the best failure criterion for predicting the internal cavities initiated at center of the workpiece [5]. The FEM analysis in the abovementioned studies however did not take into account the effect of the workpiece heating due to interfacial friction and the plastic deformation and cooling through convection and conduction. The coupled thermo-mechanical models are therefore expected to monitor the deformation behavior of the workpiece more accurately in the CWR process. A recent conducted coupled thermo-mechanical analysis has clearly showed that the touching surface of the workpiece was cooled down gradually when it was in contact with the tools and it was re-heated after losing the contact with the tools. The temperature of the center and surface of the workpiece either increased or decreased depending on the initial workpiece temperature and tools temperature because of the heat losses by convection and conduction [6-8]. In the present thesis, a coupled thermo-mechanical FEM analysis was carried out, using LS-DYNA commercial software, to determine the effect of the CWR process parameters on the strain, mean stress, temperature and deformation rate of the workpiece. The used model differed from the previous models in including thermal analysis, adiabatic heating and the associated workpiece softening and strain rate sensitivity of the workpiece.

CHAPTER 2

CROSS-WEDGE ROLLING PROCESS

The CWR is a plastic forming process, in which a cylindrical workpiece (billet) is formed into stepped rotational parts between two wedge type tools moving tangentially relative to the billet (Figure 2.1). The wedge tools assembled on rolls, called roll CWR, or on a plate, called flat CWR, deform the billet plastically usually at an elevated temperature.

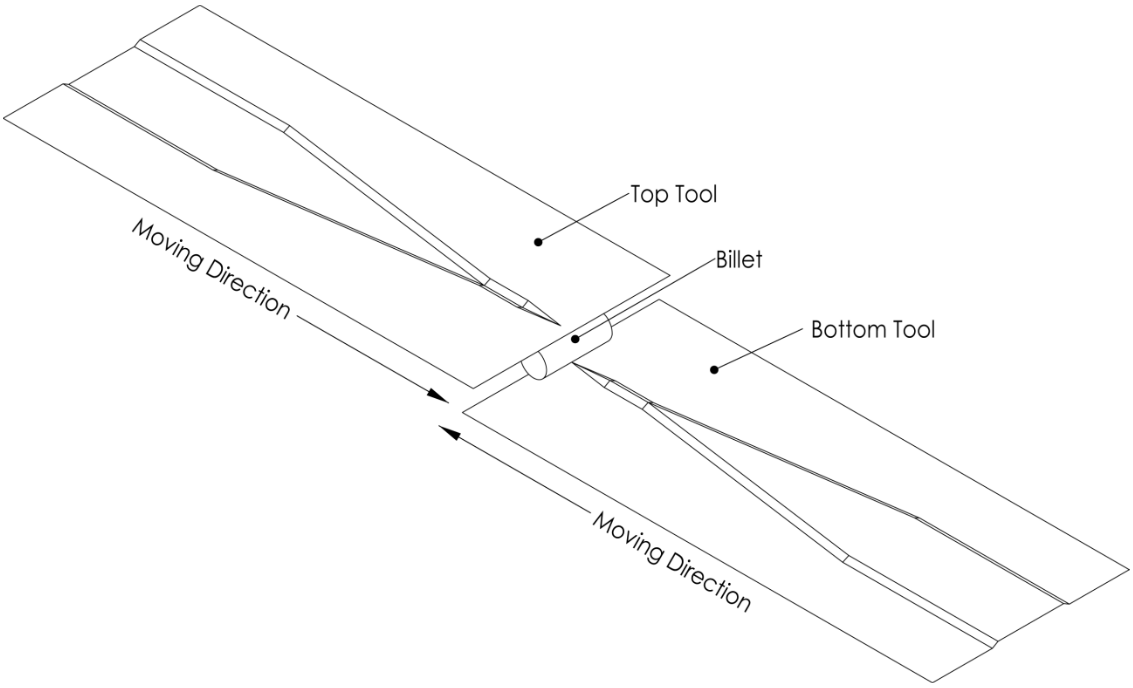

Figure 2.1. Illustration of flat-wedge type CWR process.

The CWR process has several important advantages over the conventional forming processes, including [9-12];

1. Process automation and lower operation cost: final sizing and surface refining are automatically carried out in one rolling cycle. As a result, less operator, knowledge and auxiliary equipments are required.
2. Higher production rates and lower material cost: more than one workpiece can be formed in each production cycle. Productivity is 5 to 20 times higher than that of conventional forming processes.

3. Higher rate of material utilization: less than 10% material is wasted in end cutting and possible grinding.
4. Better product quality: since the CWR is a metal forming process in which the desired product shape is made by the plastic flow of the metal, the metal fabric is continuous, and finer grains are obtained, resulting in stronger final products.
5. Less hazardous material disposal to the environment: no additional environment-polluting lubricating fluid is used.

Despite well-known advantages, the CWR has not been widely accepted by the metal forming industry. This is partly due to the lack of the adequate technical knowledge on the workpiece deformation, friction and the failure mechanisms in the process as well as the complexity of the tool design. Since the interactions between the tool and the workpiece are not predicted accurately and reliably, the automation of the CWR process is difficult. Several trial products are required in order to produce a single product design. These design techniques are based on the experience and trial-and-error methods, which are often unreliable, time consuming and expensive. [12]

2.1. Types

During CWR, a cylindrical workpiece is plastically deformed into an axisymmetrical product by the action of wedge shape dies moving tangentially relative to the workpiece. Shafts with tapers, steps, shoulders, and walls with almost no draft angles can be made by the CWR. The CWR machine is typically composed of one to three rollers on which wedge-shaped tooling are mounted. Figure 2.2(a-e) show the five most popular CWR machine configurations available [12]. In hot rolling, the workpiece is preheated to a prescribed temperature and is then fed into the tool gap in the axial direction of the rollers.

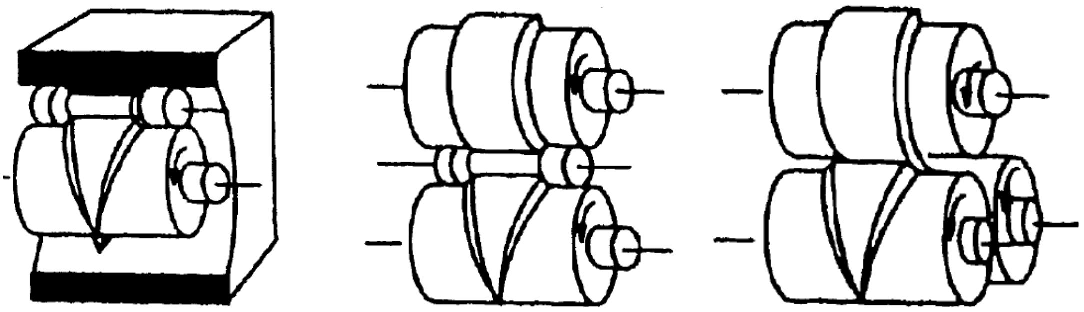

(a) One-roll (b) Two-roll (c) Three-roll

(d) Concave wedge (e) Flat wedge

Figure 2.2. Most common types of CWR tool configurations.
(Source: Fu and Dean 1993)

2.2. Tooling

In CWR, there are four stages of the workpiece deformation corresponding to four zones of the wedge tool geometry (Figure 2.3). These stages are [9, 13]:

1. Knifing zone: This is the initial zone, which has an incline (γ) starting at zero and increases to the total reduction of height for the workpiece. The cylindrical workpiece is driven in this zone and a V-shaped groove is formed into its circumference.
2. Guiding zone: This is the second zone in which a uniform V-shaped groove is formed around the workpiece surface. The wedge profile does not change in this zone. The area reduction is constant starting from this zone up to end of the sizing zone.
3. Stretching zone: In this zone, the workpiece is deformed (stretched) by increasing the width of the wedge because of stretching angle. The workpiece is forced to enlarge through the both ends by the tool angles.
4. Sizing zone: The workpiece is formed into its final geometry, dimensions and surface quality in this finishing zone. In this zone, β is zero and the wedge

shape is uniform. At the end of the sizing zone, the side cutters cut the scrapped ends of the workpiece.

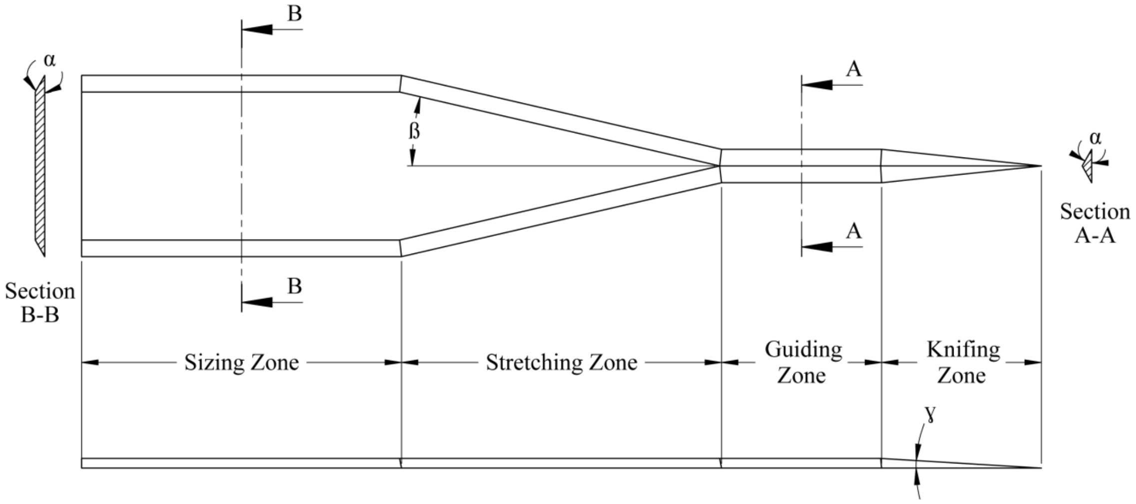

Figure 2.3. CWR tool geometry and deformation zones.

2.3. Failure Mechanisms

In CWR process, there are several different failure mechanisms. These failure mechanisms are the main obstacles preventing CWR process from being a commonly preferred method by the metal forming industry. Johnson and Mamalis [14] previously identified several different failure mechanisms in CWR process as shown in Figure 2.4. In one study [15], authors categorized the failure in CWR into three main types (Figure 2.5). These are: (a) excessive slip, (b) surface defects (necking, spiral grooves and lapping) and (c) internal voids.

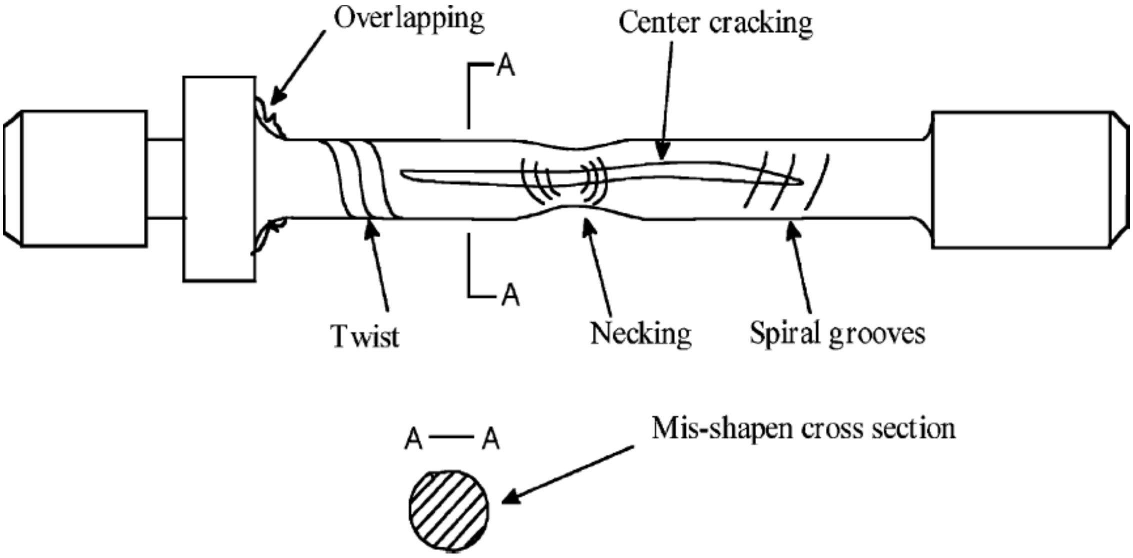

Figure 2.4. The common failure mechanisms in CWR process.
(Source: Li, et al. 2002)

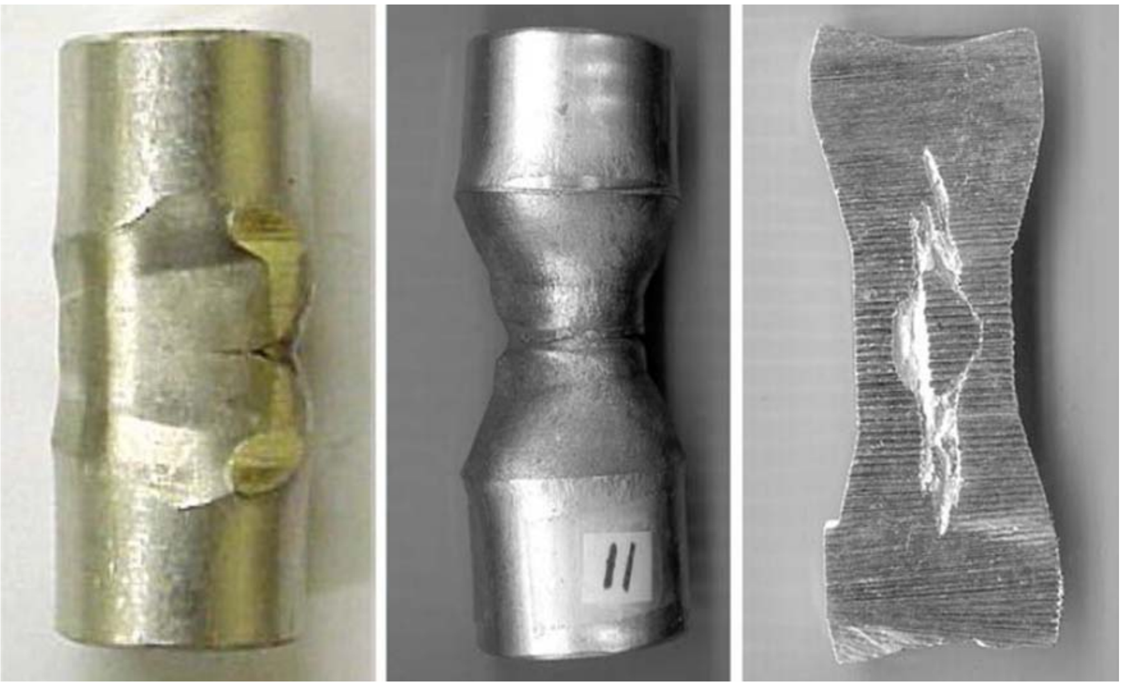

(a) Excess slip (b) surface defect (necking) (c) Internal void

Figure 2.5. Three main failure mechanisms in CWR: (a) excess slip, (b) surface defect (necking), and (c) Internal void. (Source: Q. Li, et al. 2002)

2.3.1. Excessive Slip

The slip is defined as the difference between the tool displacement and workpiece rotation. The ratio of the total tool liner displacement, U_t, normalized with circumference of the workpiece gives the normalized tool translation (U_t) as,

$$U_t = \frac{u_t}{\pi d_o} \tag{2.1}$$

The linear displacement of the workpiece (u_w) is given by

$$u_w = \frac{\pi d_o \theta}{360} \tag{2.2}$$

where, θ is the angular rotation. Then the slip (S) between tool and workpiece is defined as

$$S = \frac{u_t - u_w}{\pi d_o} \tag{2.3}$$

Excessive slip between workpiece and tools results in improper deformation, leading to misalignment and irregular deformed cross-section of the workpiece. It was shown both experimentally and numerically that the slip between tool and workpiece increased gradually as the CWR deformation progressed [12]. The effect of friction, area reduction and forming angle on the slip between tool and workpiece was investigated both experimentally and numerically [1, 12]. It was shown that the interfacial slip was very sensitive to friction coefficient and the slip was found to be decreased as the friction coefficient increased over a critical value. For the studied geometry, the critical friction coefficient was found 0.3. In order to form a high friction coefficient and hence to prevent the slip between tool and workpiece, the tools are usually serrated in knifing and guiding zones. The increased forming angle was found to increase the slip; higher values of forming angle lead to sharper tool edge which the reduced the friction between tools and workpiece. As the area reduction decreased, the interfacial slip reduced. This was attributed to the increased friction coefficient between tool and workpiece. The slip rate was also found to increase in the knifing zone, reaching a maximum value and thereafter reached a steady value at the end of the guiding zone. Hayama proposed the following semi empirical relation at a constant friction coefficient of 0.35 for a slipping-free CWR process [16],

$$(0.15+0.0038\alpha)\beta^{0.925} \leq 1.93 \tag{2.4}$$

The nature of interfacial slip in a two-roll CWR operation was characterized using analytical and a three-dimensional FEM [3]. The results showed that the global slip increased with decreasing friction coefficient and a critical friction coefficient was found between μ=0.2 and 0.3. Increased forming angles resulted in larger global slip values and a substantial increase in the global slip was found between α=30° and 40°. The forming angle was found to have the least influence on the global slip in the guiding and sizing zones, where less significant plastic deformations occurred. Increasing the area reduction and the forming velocity was found to increase the global slip. In another study [17], authors investigated a critical friction model for CWR hollow 6061 T6 Al workpieces. It was shown that the critical friction coefficient for the hollow sections was two times greater than that for the solid sections. This tendency was attributed to the substantially lower radial rigidity of the hollow than the solid sections.

2.3.2. Surface Defects

The necking failure of the workpiece occurs due to the excessive thinning of the workpiece at the central region. Necking occurs when the tensile stress is greater than the material tensile strength. The material flow is continuous until the workpiece is broken and this occurs at the central portion of the workpiece where the tensile stress is maximum. Necking was shown to be promoted when the forming and stretching angle and area reduction increased [18]. The following mathematical formulations were proposed for the CWR process stability without necking by [19]:

$$\frac{\sqrt{2\tan\alpha\tan\beta}}{\pi}(1+\sqrt{\frac{1}{\delta}})(\delta-1) \leq 0.2 \tag{2.5}$$

and by [16]:

$$\delta \le \frac{1}{2}\left(2+\pi\tan\alpha\tan\beta+\frac{\sqrt{3\pi/2\tan^{3}\alpha\tan\beta}}{\xi}\right) \tag{2.6}$$

and by [18]:

1. for a process with c ≤ 1:

$$\frac{4\delta^{2}q_{m}}{3\pi\sigma_{0}}\cos\beta\frac{\delta-1}{\delta}\sqrt{3c\frac{\delta-1}{\delta}}\left\{\begin{array}{l}\left(1+\frac{\mu_{b}\sin\beta}{\tan\alpha}\right)\times\left[1-\sqrt{\left(\frac{1+c\delta-c}{\delta}\right)^{3}}+c\frac{\delta-1}{\delta}\right]\\+\frac{\mu_{k}\sin\beta}{\tan\alpha}\left[\frac{3}{2}\left(c-1\right)+\sqrt{\frac{\delta+1}{2\delta}}\right]\end{array}\right\}<1 \tag{2.7}$$

2. for a process with c > 1:

$$\frac{4\delta^{2}q_{m}}{3\pi\sigma_{0}}\cos\beta\sqrt{3c\frac{\delta-1}{\delta}}\left\{\begin{array}{l}\left(1+\frac{\mu_{b}\sin\beta}{\tan\alpha}\right)\times\left[1-\sqrt{\left(\frac{1+c\delta-c}{\delta}\right)^{3}}+c\frac{\delta-1}{\delta}\right]\\+\frac{\mu_{k}\sin\beta}{\tan\alpha}\sqrt{\left(c\frac{\delta-1}{\delta}\right)^{3}\left(\frac{2+c\delta-c}{2\delta}\right)}\end{array}\right\}<1 \tag{2.8}$$

Figure 2.6 shows the necking limits calculated using the above equations for different reduction ratios. The necking limit shown in this figure decreases with increasing reduction ratio and varies with forming and stretching angles.

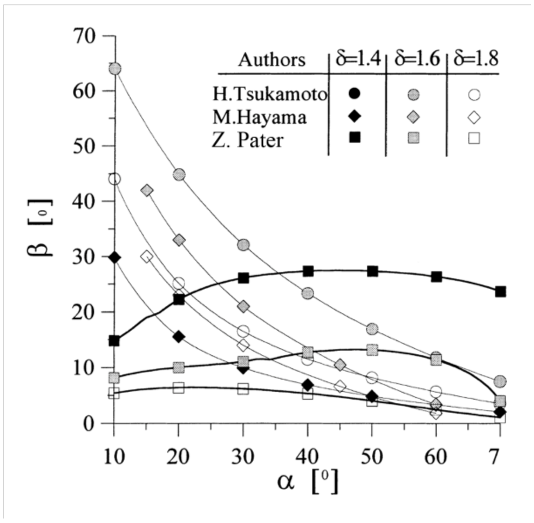

Figure 2.6. The necking limits calculated by various authors.
(Source: Pater, et al. 1999)

Spiral grooves occur due to the opening of the cracks near the surface of the workpiece. Spiral grooves were commonly seen when the frictional forces between tool and workpiece were high [10]. Lapping occurs when there is a extreme material flow through the radial direction and results in elliptical cross-section of the workpiece at sharp forming angles [18].

2.3.3. Internal Voids

Internal void/crack formation is a major obstacle in the CWR process, as it weakens the workpiece and can ultimately lead to workpiece failure. Moreover, these defects cannot be visually detected; hence, often require special inspection such as ultrasonic examination. Two types of internal defects, centerline cracks oriented along the workpiece and annular cracks are known to occur in CWR [1]. If the internal cavities are discontinuities in the microstructure, these are termed porosity or Mannesmann failure. The name originated from the Mannesmann brothers discovery of the internal voids and cracks formation in the forging of the cylindrical steel bars in 1885 [9]. The internal void formation and crack initiation were reported to be caused by (i) large tensile stresses along the central portion of the workpiece, (ii) excessive shear stresses in the knifing zone and (iii) low cycle fatigue [3, 20, 21]. The centerline cracks were observed in the cruciform shape (Figure 2.7) and propagated through the direction of the maximum principal stresses [22].

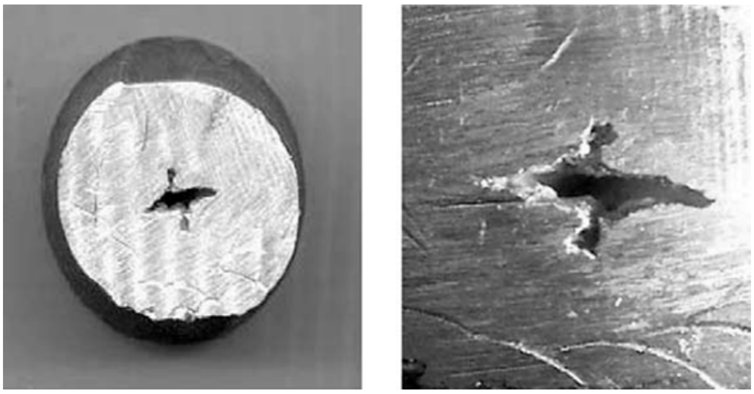

(a) Overall view. (b) Central part (5x).

Figure 2.7. The horizontal cross-section of cross wedge rolled 1100 Al (α=15°, β=7° and Δ_A = 38.2% (a) overall view; (b) central part (5x).
(Source: Li, et al. 2002)

Among the investigated three different failure criteria, which were based on the mean stress, effective stress and effective strain, the failure criterion based on the maximum effective plastic strain was proposed to be the limiting criterion for the maximum possible deformation in the CWR [21]. A deformation coefficient (ε) was also introduced in order to predict the likelihood of a void formation as [21]

$$\varepsilon = \underbrace{\frac{2L_2'}{d'-d}}_{\alpha}\,\underbrace{\frac{L_1'}{L'-L_1'}}_{\beta}\,\underbrace{\frac{A-A'}{A}}_{\Delta_A} \tag{2.9}$$

where, d and A are sequentially the diameter and cross-sectional area before the deformation, L' and A’ are sequentially the length and cross-sectional area after the deformation, and d’, L_1’ and L_2’ are shown in Figure 2.8. It was reported that, void would form when the deformation coefficient exceeded 0.6 in 1100 Al samples.

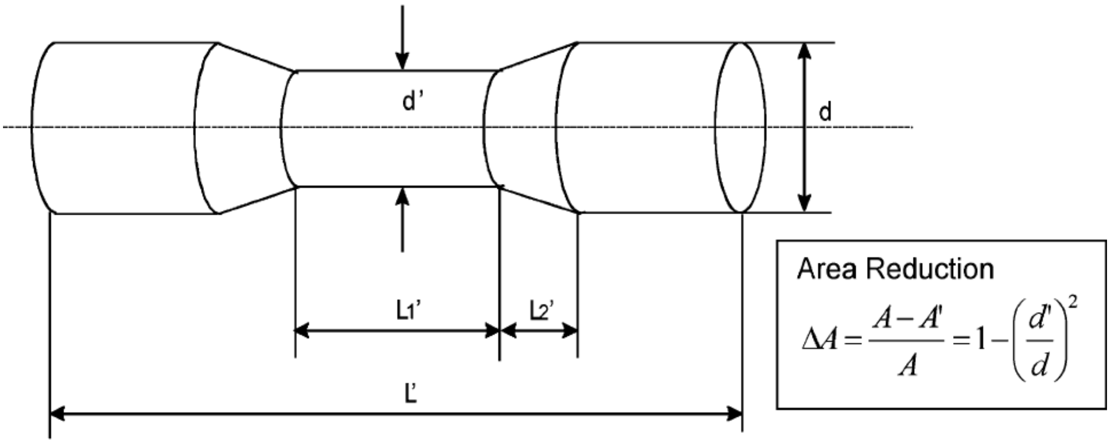

Figure 2.8. The geometrical parameters on deformed workpiece.
(Source: Li, et al. 2002)

Pater investigated the CWR process stability in rotational compression process by dividing the forming zone into several layers in [23] as shown in Figure 2.9. The contact pressures were calculated by taking the based the sum of the moments of forces zero. The model results were further compared with the results of the experimentally tested pure lead alloy with a flow stress-strain behavior of $\sigma(\text{MPa}) = 14.45\varepsilon^{0.04}$. Figure 2.10(a) and (b) show the effect of forming angle and reduction ratio ($\delta = d_0/d$) and spreading angle and reduction ratio on the CWR process stability, respectively. When β is constant and δ is lower, increasing α increases the limit of the slip between tool and workpiece as seen in Figure 2.10(a). Necking limit area increases with increasing α and δ. At a constant α and low values of δ, increasing β increases the limit of the slip between tool and workpiece as seen in Figure 2.10(b), a similar effect is also seen when α increases. The necking limit area increases with increasing β and δ values.

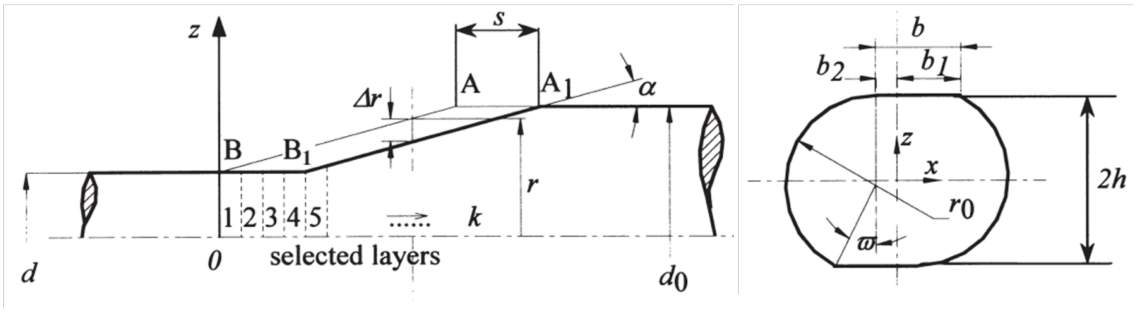

(a) axial sectional view. (b) separated layer

Figure 2.9. Laminar modeling of forming zone in CWR process.
(Source: Pater 2000)

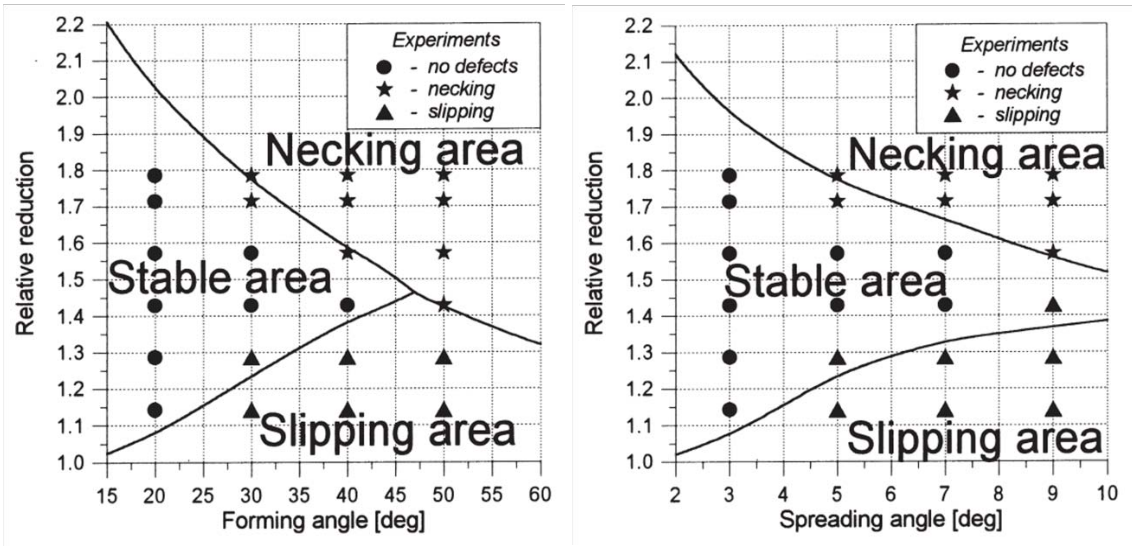

(a) (b)

Figure 2.10. The effect of (a) forming angle and reduction ratio (β=5°, d=14 mm, μ_b=1.0, μ_k=0.7), (b) spreading angle and reduction ratio (α=30°, d=14 mm, μ_b=1.0, μ_k=0.7) on the CWR process stability. (Source: Pater 2000)

The CWR limits of forming hollow tubes of 100 and 6061 Al and copper alloy was investigated by [24]. The workpiece wall thickness and material, area reduction, and tool geometry varied in the analyses. A dimensionless crushing parameter was introduced to predict the operating conditions that leaded to failure as,

$$\psi = \Delta_A \frac{t_f}{t_i} \frac{UTS}{E} \tag{2.10}$$

where, t_i is the initial workpiece wall thickness, t_f is the final workpiece wall thickness, UTS is the ultimate tensile strength, and E is the elastic modulus of the workpiece. The crushing was found to be highly dependent on the area reduction and the workpiece wall thickness and material, while the rolling speed and tool angles (α and β) were found less critical.

2.4. Previous FEM Analysis of CWR Process

A finite-element model was used to characterize the friction and slip in the knifing and guiding zones of the flat-wedge rolling process [12]. Only the knifing and guiding zones of the tool were modeled. Slip was calculated experimentally and numerically for a particular tool geometry and for three different area reductions. The experimentally measured tool-workpiece slip was shown in good agreement with those predicted by the FEM developed. Finally, the slip between tool and workpiece was shown to increase as the forming process progressed and lower area reductions resulted in higher amounts of slip.

The authors of [25] investigated the relationship between the tool-workpiece interfacial slip and CWR process variables for a flat-wedge CWR process using ANSYS/LSDYNA. The model was used to analyze 189 distinct operating conditions, varying workpiece material (aluminum 1100, steel 1018 and brass C21000), forming velocity ~ 0.4; 4.0 m s^{-1} , area reduction (25%, 40% and 55%) and forming angle (20°, 30° and 40°). A coulomb friction model with constant static and dynamic friction coefficient values of 0.5 and 0.46 and the exponential decay coefficient of 1.0 s m^{-1} were used in the FEM simulations. The forming velocity, the area reduction and forming angle were shown to be important variables in determining the interfacial slip characteristics of the CWR process analyzed.

The authors simulated the CWR process using static implicit DEFORM-3D FE program in [26]. In the model, dynamic adaptive re-meshing with tetrahedral solid elements was used. The diameter of the cylindrical workpiece was 40 mm, modeled with a rigid–plastic material model. The wedge dies were considered rigid. It was found that the lateral force of the tool increased, but the thrust force decreased as the oblique angle increased.

Bartnicki and Pater modeled the CWR process of a hollow shaft (pure lead) using SuperForm 2002 software (Figure 2.11) [27]. The results of experimental works were used for the verification of numerical simulations. The authors presented the phenomena that reduced the field of stability of CWR process parameters for hollow shafts. The two flat wedge tools and the workpiece (Figure 2.11) were modeled with 8-nodes hexagonal elements. The wall thicknesses of the simulations were compared with those of the experiments. An example of this comparison is shown in Figure 2.12. In most of the experiments and models, the wall thickness was found to decreases after CWR process. It was found that the greater the initial wall thickness of workpiece, the more intensive material flow was present.

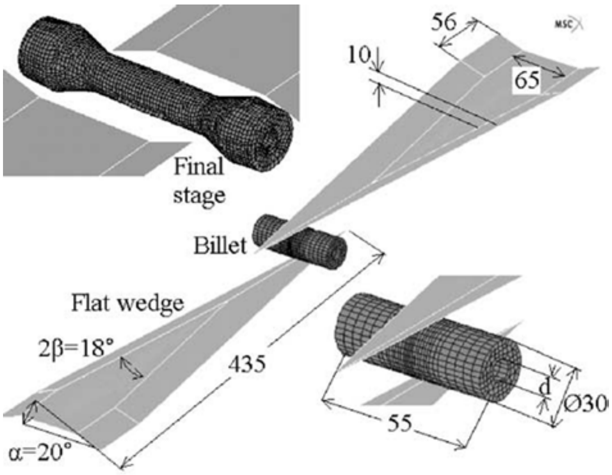

Figure 2.11. The geometrical FEM of CWR process of the hollow shafts. (Source: Bartnicki and Pater 2005)

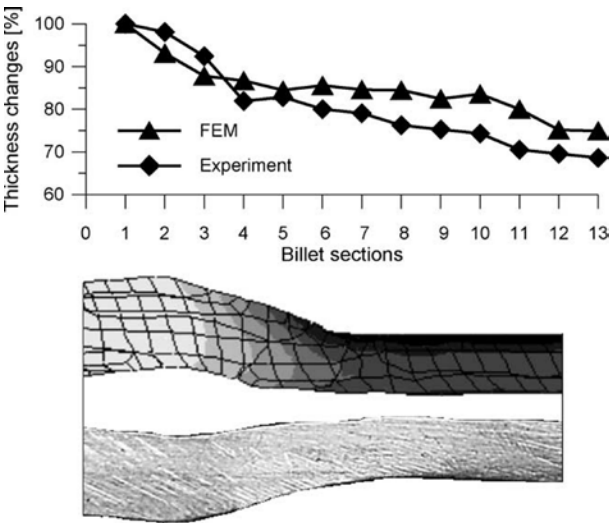

Figure 2.12. The variation of wall thickness of the FEM and experiments of CWR of a hollow section. (Source: Bartnicki and Pater 2005)

The mechanisms of void generation and growth in CWR was investigated using specialized experiments and a explicit dynamic three-dimensional FEM (ANSYS/LS-DYNA) [21]. The morphology of void generation was determined as a function of the workpiece material and three primary parameters in CWR process: the forming angle, the stretching angle, and the area reduction. The cylindrical work piece and two forming tools were meshed with an eight-node structural solid element with six degrees of freedom (u_x, u_y, u_z, w_{xy}, w_{yz} and w_{zx}) per node (Figure 2.13). Single point integration and viscous hourglass control were used for all the elements in the model to reduce the computation time and to ensure robustness during large deformations. The forming tools moved with an equal and opposite velocities in the horizontal (x) direction, the workpiece was left unconstrained and the forming tools were held in the vertical (*y*) and out-of-plane (*z*) directions. The effective stresses at the centroid for aluminum, copper and steel workpiece materials were determined. Several important trends for the variation of the effective stress were shown (Figure 2.14). It was stated that the effective stress curves behaved similarly for all three workpiece materials and for both forming angles. In addition, the effective stress sharply increased in the knifing zone and then maintained a constant maximum value in the guiding zone. The effective plastic strain distributions were evaluated during the first two zones of the tool (Figure 2.15). I was concluded that the effective plastic strain was the best criterion for predicting the internal failure in CWR.

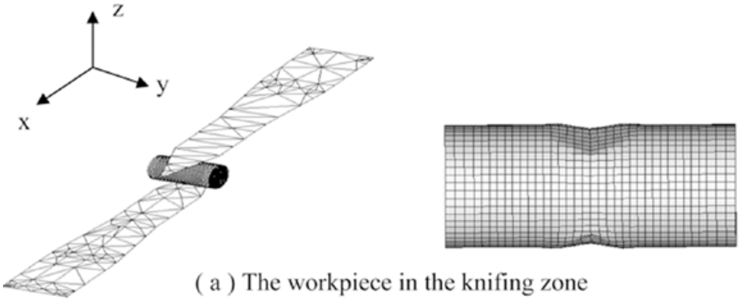

(a) The workpiece in the knifing zone

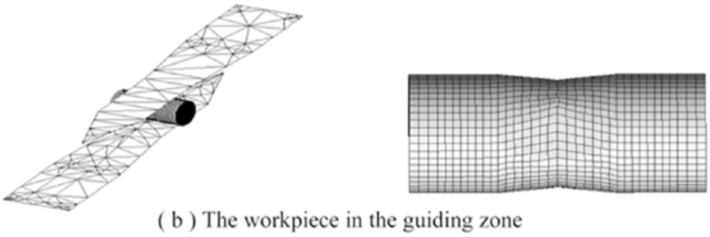

(b) The workpiece in the guiding zone

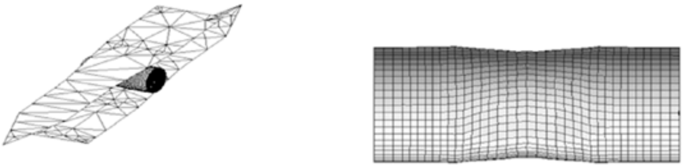

(c) The workpiece in the stretching zone

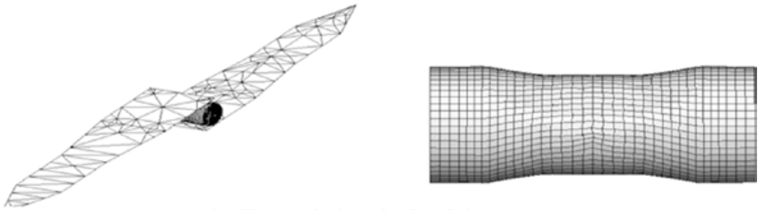

(d) The workpiece in the sizing zone

Figure 2.13. The flat wedge CWR process simulation.
(Source: Li and Lovell 2004)

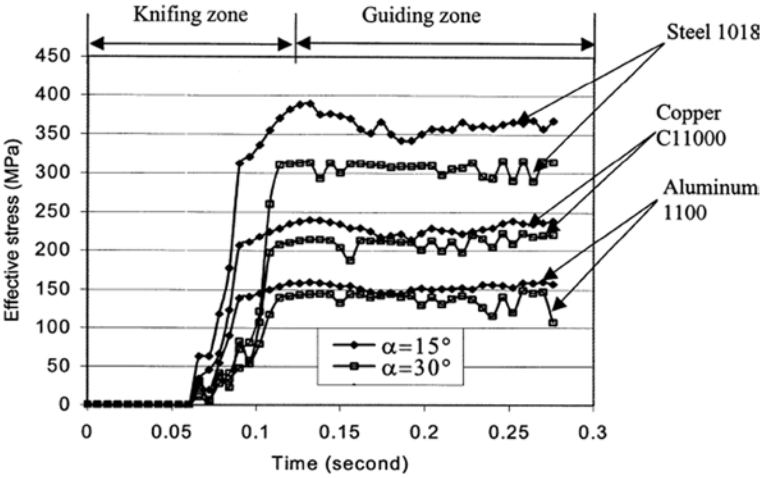

Figure 2.14. The effective stress distribution of the centre point.
(Source: Li and Lovell 2004)

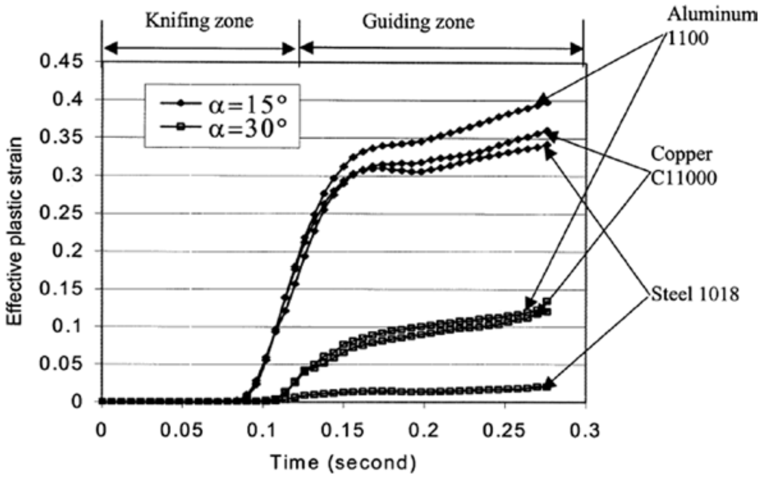

Figure 2.15. The effective plastic strain distribution of the centre point.
(Source: Li and Lovell 2004)

Bartnicki and Pater modeled forming of hollowed shafts in a three-roll type CWR process using SuperForm 2002 and SuperForm 2004 programs [28]. The model consisted of three rolls with wedge tools (moving with the same speed 1 rad s^{-1} each). The workpiece was modeled by eight-node, hexagonal elements and re-meshing was applied. An example for progression of shape of workpiece rolled with the use of three rolls is shown in Figure 2.16. It was shown that the CWR method with three wedges was functional for manufacturing axi-symmetrical hollow parts.

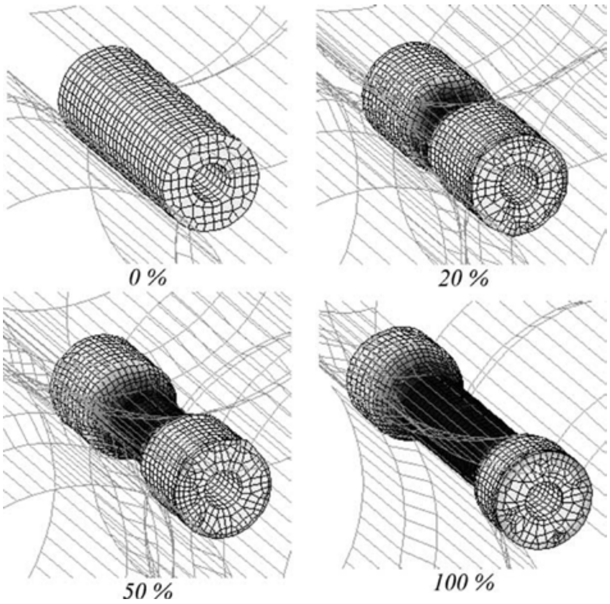

Figure 2.16. Changes of shape of a hollowed shaft calculated for the CWR process with the use of three rolls with shown progress (*d*=12 mm, α=30°, β=15°, δ=1.5). (Source: Bartnicki and Pater 2005)

The authors of [29] modeled the CWR process of ball pins in which two forgings were formed at the same time using SuperForm 2004 program. Tools were assumed rigid and a constant friction coefficient was used in the model. The rounding of wedge edges were omitted in order to minimize the computation time. The largest values of strain were shown to present in the cylindrical part of the ball pin (Figure 2.17). The changes of the tangent force (responsible for wedge pressing) and radial force (directed perpendicularly to tool sizing surfaces) are shown in Figure 2.18. Although the distribution of forces was qualitatively identical, the radial force was four times bigger than tangent force. Maximum values of both forces appeared at the end of forming zone; the free flow of material in the longitudinal direction was blocked by guiding devices. It was concluded that FEM models were necessary in designing of such complex metal forming processes.

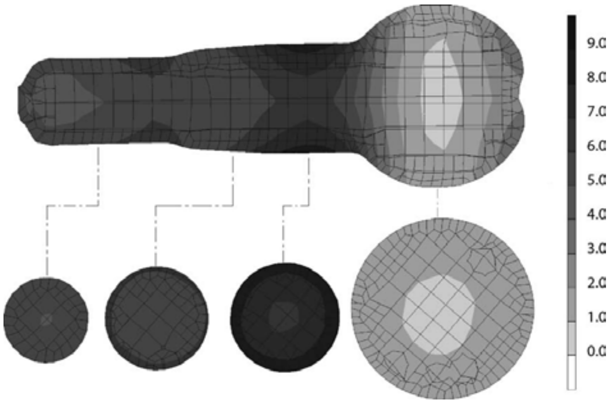

Figure 2.17. Distribution of effective strain in longitudinal and cross-sections of rolled ball pin. (Source: Pater et al. 2005)

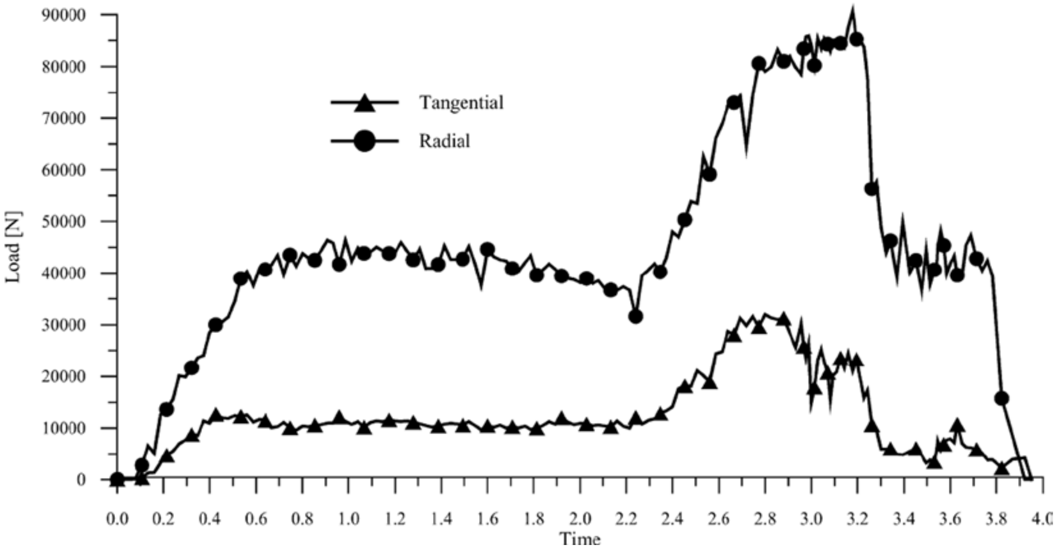

Figure 2.18. Calculated distributions of rolling forces during CWR of ball pin in double configuration. (Source: Pater et al. 2005)

The authors investigated the influence of CWR process parameters on the global slip by the three-dimensional finite element model (FEM) using ANSYS/LS-DYNA program in [3]. The model was composed of a cylindrical Al 1100 workpiece (25.4 mm diameter) and two wedge-shaped rolls (Figure 2.19). The 1045 steel dies and rolls were considered as rigid in the model and all of the components were meshed using eight-node, single point integration solid elements. The workpiece and the rolls were constrained to permit only the rotation about their central axes to replicate the operating conditions in the actual two-roll CWR process. A strain-rate dependent constitutive plasticity model was used for the workpiece in the FEM analysis. Strain rate was accounted by using the Cowper-Symonds model. A surface-to-surface contact algorithm was used to define the contact interaction between the workpiece and dies along with a classical coulomb friction model. CWR experiments were performed under the operating condition of $\alpha = 30°$, $\beta = 5.25°$ and $\Delta_A = 22\%$. The experimentally measured workpiece profile was compared with the FEM model and the average difference in geometry was determined to be less than 2%. FEM model adequately captured the plastic deformation within the workpiece during the two-roll process examined. It was found that the excess interfacial slip failure occurred in the CWR experiments and FEM model when $\mu = 0.149$, but not to occur when $\mu = 0.210$. The influence of the friction coefficient on the global slip in the knifing, guiding, stretching and sizing zones were separated (Figure 2.20). The nature of the global slip in stretching zone, however, was found significantly different from the other zones. In the other three zones (especially in the guiding and sizing zones), the amount of the slip substantially increased when the friction coefficient decreased from 0.3 to 0.2. This demonstrated that in these three zones, the critical friction coefficient was not attained for $\mu = 0.2$. The effect of friction coefficient on the effective plastic strain at internal points within the workpiece is shown in Figure 2.21(a). All of the friction curves behaved identically except $\mu = 0.2$ (Figure 2.21(b)). A same tendency in the experimental results was found where interfacial slip failure occurred at the knifing-guiding zone transition. The friction coefficient curves behaved identically in the first two zones of the tool and the strain was significantly lower for $\mu = 0.2$ in the stretching and sizing zone (Figure 2.21(c)). The primary difference was the point at which the excess slip failures became apparent. For point 2, the excess slip was not found until the sizing zone simply because of its location. Since point 2 was located a short distance away from point 1 in the longitudinal direction, it did not experience significant plastic strain until the stretching zone, where the deviation in strain values occurred. It was concluded that a critical friction coefficient existed between $\mu = 0.2$ and 0.3 and the global slip increased with decreasing friction coefficient. The forming angle had the least effect on the global slip in the guiding and sizing zones. The global slip increased when the area reduction and forming velocity was decreased due to the lower flow resistance of the workpiece material.

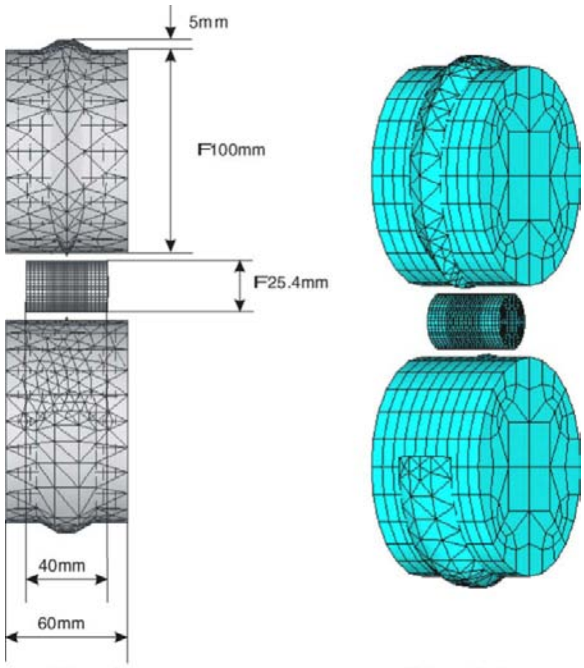

(a) Front view

(b) Isometric view

Figure 2.19. Two-roll FEM of CWR.
(Source: Li and Lovell 2005)

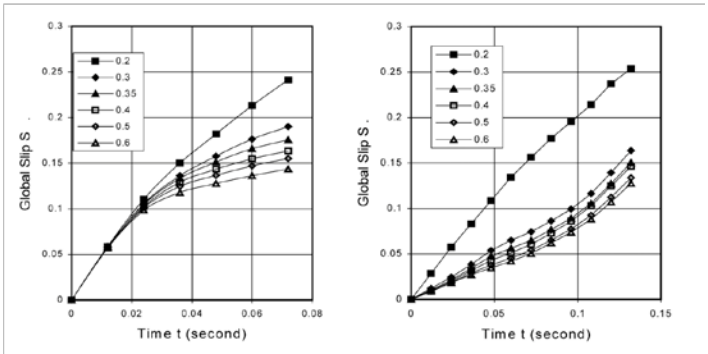

(a) Knifing zone

(b) Guiding zone

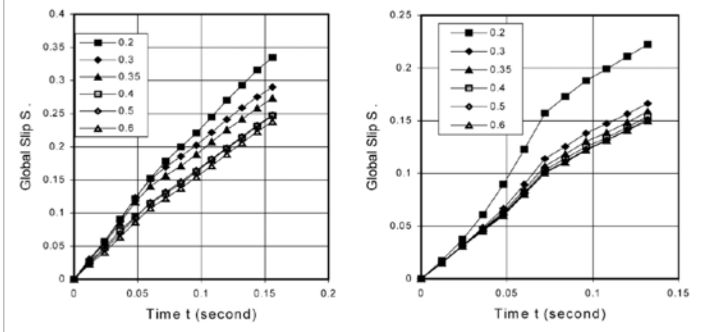

(c) Stretching zone

(d) Sizing zone

Figure 2.20. Variation of interfacial slip with friction coefficient in each zone ($\alpha = 30^\circ$, $\beta = 5.25^\circ$, $\Delta_A = 22\%$, $\nu = 0.4$ m/s). (Source: Li and Lovell 2005)

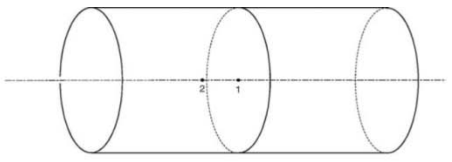

(a) Location of the investigated points

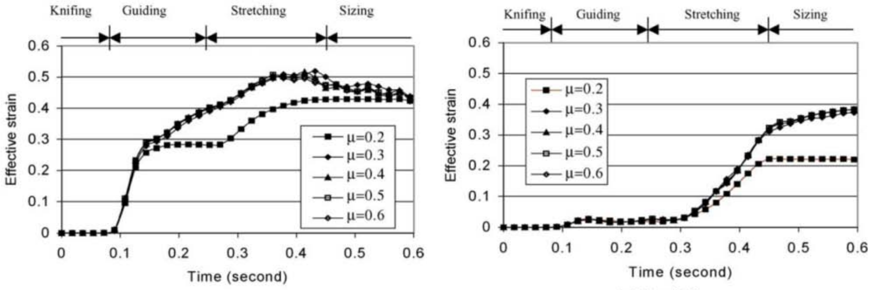

(b) At point 1 (central point)

(c) At point 2

Figure 2.21. The effective strain distribution of the selected points with different friction coefficients ($\alpha = 20^{\circ}$, $\beta = 5.25^{\circ}$, $\Delta_A = 38\%$, $\nu = 0.4$ m/s).
(Source: Li and Lovell 2005)

The authors of [30] combined a 3D non-linear thermo mechanical coupled FEM with material microstructural evolution in CWR of AISI 5140 steel. The model was generated in the commercial FEM software Deform 3D. They also evaluated some empirical equations for recrystallization evolutions and using the Gleeble-3500 thermo-mechanical simulator transformation to use in the simulation. A constant shear friction model close to 1.0 was used for the bulk-forming simulations. Following process parameter was used in the model: initial workpiece diameter: 20 mm, final diameter: 15.6 mm, spreading angle: 5°, forming angle: 30°, initial temperature of workpiece: 900 °C, initial temperature of tools: 20 °C, environment temperature: 20 °C, heat transfer coefficient between tools and workpiece: 11 N/s/mm/° and convection coefficient: 0.02 N/s/mm/°C. The mathematical functions of the microstructure evolution containing dynamic, static recrystallization and grain growth were embedded in the FEM software DEFORM. The equivalent strain was found to be larger on the workpiece surface than the center position. It was determined that the strain rate was highest at the contact area and greatly decreased outside of the contact area while the temperature was highest at middle of the workpiece.

The authors of [31] analyzed a 3D model of the CWR process using ANSYS/LS-DYNA. The mill rolls were assumed rigid and meshed with shell elements (shell163). The axes of rolls were constrained and the two mill rolls were rotated in the same direction. The workpiece was meshed with eight-node solid element (Solid164) with single point integration. The material model was piecewise linear plasticity, 1045 steel. The forming angle was 30°, diameter of workpiece was 60 mm, the spreading angle was 7°, and the area reduction was 30%. They concluded that the large lateral tension stress was generated at the center of rolled part.

The CWR process of 20MnCr5 steel was studied using MARC/AutoForge FEM software in [32]. The process was carried out under isothermal conditions. In this model, the friction coefficient was assumed constant and the tools were rigid. The tool wedges had linear velocities of 0.1 m s^{-1}. A uniform friction model was applied during simulation. The highest of the friction factor was assumed 1.0 for workpiece-tool contact surface. The tools temperature was taken 120 °C. The temperatures of the workpiece and the air surrounding the workpiece were taken 1050 and 50 °C, respectively. The value of heat exchange factor was taken 10 kW $(m^2K)^{-1}$. A comparison of experimental and FEM radial load are shown in Figure 2.22. The experimental and model force values correlated very well.

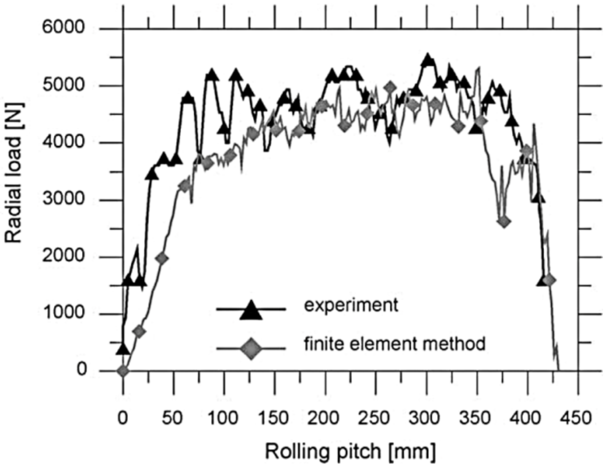

Figure 2.22. The radial load obtained for CWR process at: α=30°, β=5°, d_0=22 mm, d=14 mm, m=1.0, v=0.1 m s^{-1}, workpiece material-commercial pure lead. (Source: Pater 2006)

In one study [33], the author modeled a new cross-wedge rolling method for C45 steel in which only one flat wedge and two shaped rolls were used. The simulations were made using SuperForm 2004. In addition, experimental tests were made on a prototype rolling mill. It was shown that the method allowed for forming full and hollow forgings. The process was analyzed in isothermal condition at a temperature of 1100 °C. The FEM model was verified by comparing the wedge squeezing force (F_x) distributions of measured in experiments with calculated ones (Figure 2.23).

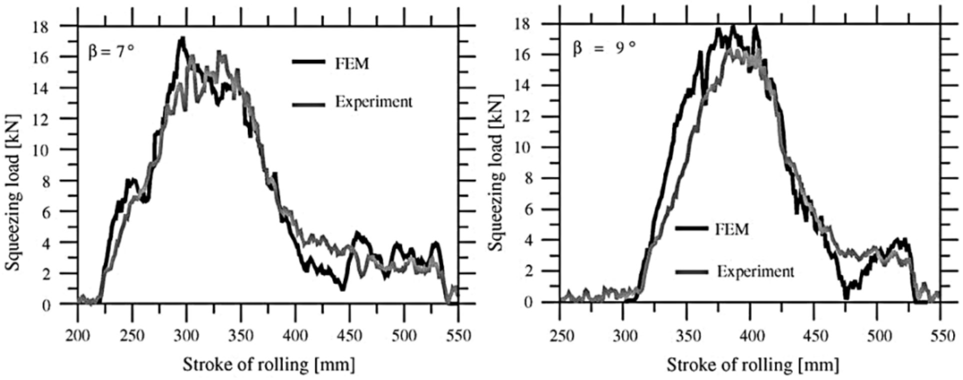

Figure 2.23. Comparison of wedge squeezing forces, measured and calculated, for steel C45 at α=30°, d=19.3 mm, d_0=23 mm, T=1150 °C.
(Source: Pater et al. 2006)

The authors of [34] simulated the equivalent strain and equivalent strain rate over the cross-section of the workpiece during CWR using the Deform-3D simulation software. The variation of equivalent strain and strain rate at different cross-sectional locations of the workpiece with rolling time was determined (Figure 2.24). It was exhibited that the equivalent strain at 1/4 R increased more rapidly. The equivalent strain rate in the stretching stage rapidly increased, resulting in periodic fluctuation at 1/4 and 1/2 R. The fluctuation period was approximately 0.5 s.

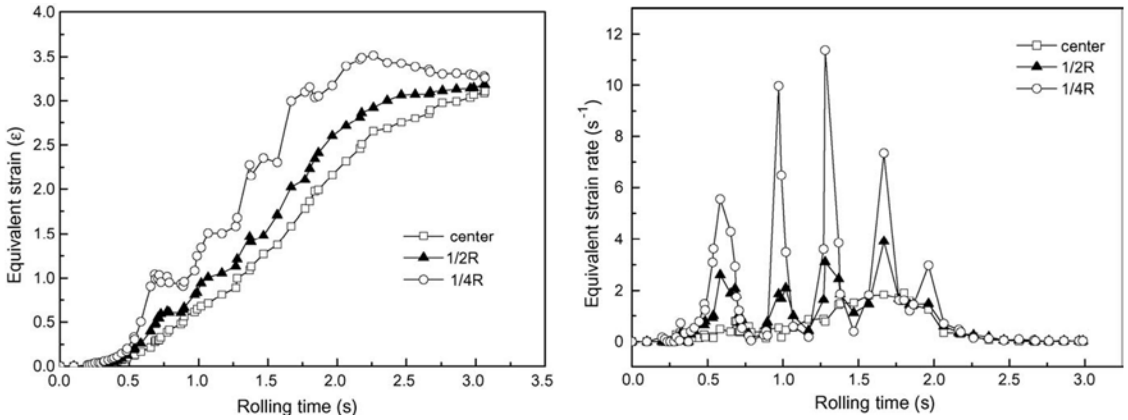

(a) (b)

Figure 2.24. Relation of (a) equivalent strain and (b) equivalent strain rate at different locations with rolling time. (Source: Xiong et al. 2006)

CHAPTER 3

EXPERIMENTAL STUDIES

3.1. Determination of Material Models

The deformation of the studied alloys was modeled using Johnson and Cook (JC) flow stress material and damage models, which are represented by the following relations,

$$\sigma = \left(A + B\varepsilon^{n}\right)\left(1 + c\ln\left(\frac{\dot{\varepsilon}}{\dot{\varepsilon}_0}\right)\right)\left(1 - T^{*^{m}}\right) \tag{3.1}$$

and

$$\varepsilon^{f} = \left[D_1 + D_2 \exp\left(D_3\sigma^{*}\right)\right]\left[1 + D_4 \ln\left(\frac{\dot{\varepsilon}}{\dot{\varepsilon}_0}\right)\right]\left[1 + D_5T^{*}\right] \tag{3.2}$$

where, σ, ε and $\dot{\varepsilon}$ are the flow stress, strain and strain rate, respectively, ε^{f} is the failure strain and A, B, n, c, m, D_1, D_2,D_3, D_4 and D_5 are constants, $\dot{\varepsilon}_0$ is the reference strain rate and T^* may be expressed in terms of temperature (T) as

$$T^{*} = \frac{T - T_r}{T_{melt} - T_r} \tag{3.3}$$

where, r and M refer to reference and melting temperatures. σ^* is the stress triaxiality parameter and for a notched specimen it is formulated as [35],

$$\sigma^{*} = \frac{\sigma_h}{\sigma_{eq}} = \frac{1}{3} + \ln\left(1 + \frac{a}{2R}\right) \tag{3.4}$$

where, σ_h and σ_{eq} are the mean and equivalent stresses, respectively, a and R are the radius of the smallest cross section and the radius of curvature at the neck (Figure 3.1), respectively. The JC flow-stress model data of 1045 steel and Ti6Al4V were studied previously and experimental details are given in ref. [36]. The quasi-static tests at room and at elevated temperature (up to 1100 °C) were conducted using a displacement-controlled SHIMADZU AG-I universal test machine at the strain rate range of 10^{-3}-10^{-1} s^{-1} on the samples 4 mm in diameter and 12 mm in gage length (Figure 3.2(a) and (b)). High strain rate tension tests were performed on the same tension test samples using a 316 L stainless steel bar tension type Split Hopkinson Pressure Bar (SHPB) set up at the strain rates between 250 and 1500 s^{-1}. Notched specimens (Figure 3.3) and unnotched specimens having four different stress triaxialities (Table 3.1) were used to determine the damage model parameter of Ti6Al4V. These samples were tested quasi-statically within the strain rate range of $1x10^{-3}$-$1x10^{-1}$ s^{-1} using the static test machine. The damage model verification was performed with the testing of the notched sample in SHPB at high strain rates. The sample deformation was recorded using a high-speed camera at 15000 fps (frame per second). The variations of the specimen minimum diameter and radius of curvature were measured using the video camera records. For each sample tested, the effective fracture strain was determined. Although the starting values of stress triaxiality, R and a changed during a test near the fracture, the changes were not taken into account. For example, stress triaxiality in a typical experiment changed only 15% near the fracture.

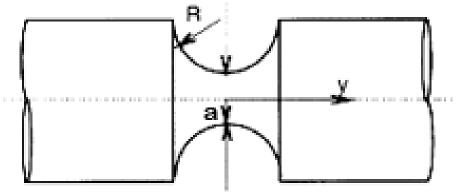

Figure 3.1. Notch specimen geometry: R and a.

(a) (b)

Figure 3.2. (a) Quasi-static and (b) high strain rate Ti6Al4V test samples.

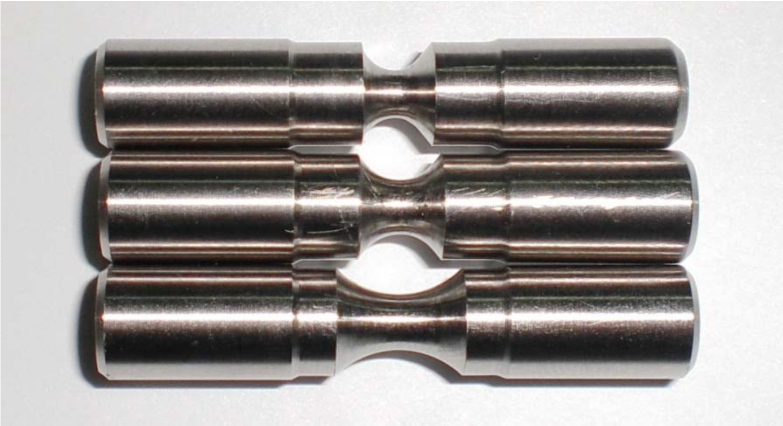

Figure 3.3. Static notch Ti6Al4V samples of R=2, 3 and 6 mm.

Table 3.1. Stress triaxiality of unnotched and notched samples.

R (mm)	unnotched	6	3	2
a (mm)	2	2	2	2
σ^*	0.33	0.486	0.621	0.738

The SHPB tension set-up was used to verify the JC damage model of Ti6Al4V alloy at high strain rates. For this purpose, a high-speed camera (15,000 and 20,000 fps) was used to record the fracture of the notched samples. In Figure 3.4(a-c), the video recordings of R=2, 3 and 6 mm samples are sequentially shown.

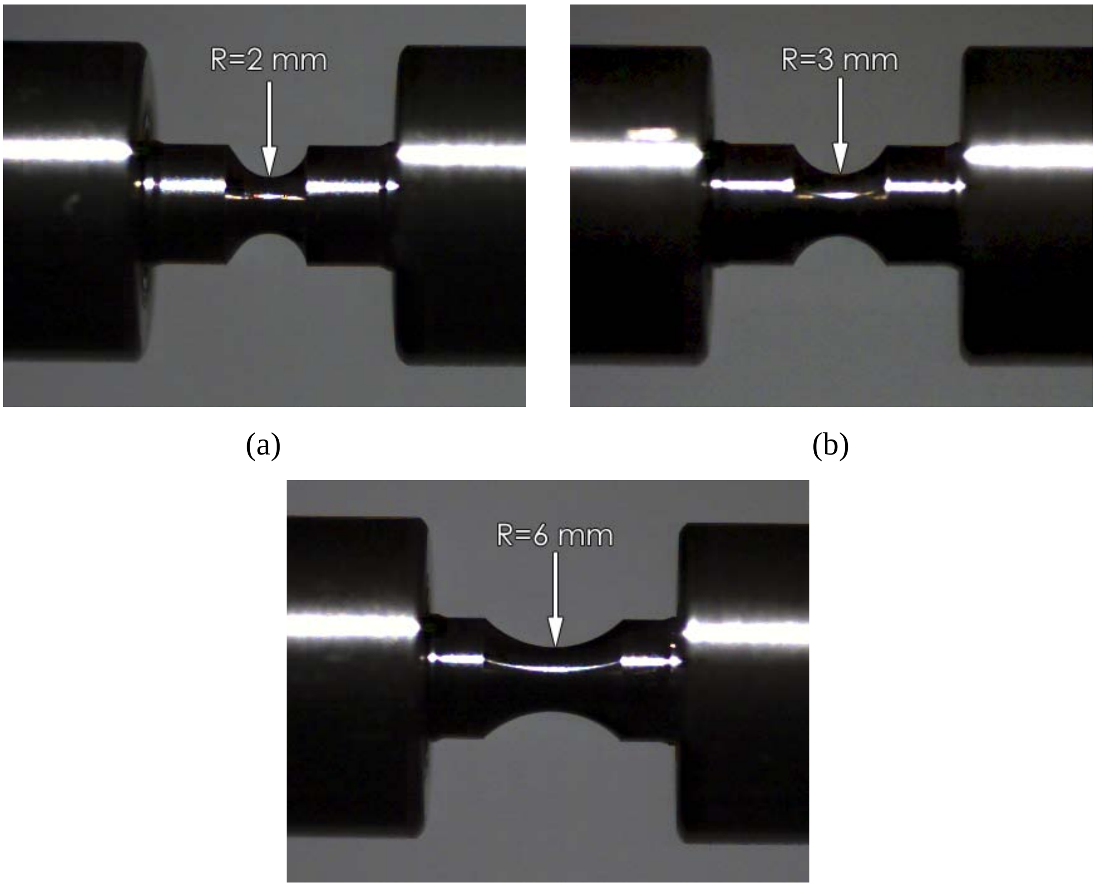

(a) (b)

(c)

Figure 3.4. The high-speed video records of notched Ti6Al4V samples: (a) R=2 mm, (b) R=3 mm and (c) R=6 mm.

3.1.1. AISI 1045 Steel

The JC parameters of 1045 steel between 900-1200 °C and at various strain rates between 0.1 and 100 s^{-1} were determined using the compression true flow stresses-strain data in ref. [37] (Figure 3.5). The model and JC-1 material model parameters are tabulated in Table 3.2 and Table 3.3, respectively. The experimental and JC-1 model compressive stress-strain curves of 1045 steel at 900 and 1100 °C are shown in Figure 3.5. The determined JC-1 model predicts the flow stress values well at 0.1 and 1 s^{-1} between 900 and 1200 °C. However, at high temperatures above 1100 °C the model cannot predict the flow stress values well at 100 s^{-1}. In the numerical model, 1045 JC material model parameters determined at room temperature through tension test at various strain rates were also used [36]. This model is called JC-2. The determined material parameters of JC-2 model are also tabulated in Table 3.3. The m value was taken the same as the m value determined from the high temperature JC-1 model. Figure 3.6 further show JC-2 model and experimental room temperature true stress-strain curves at various strain rates. In Figure 3.7, the flow stress-strain curves of JC-1 and JC-2 models are compared for different strain rates at 900 °C. Both models flow stress values at various temperatures are compared in Figure 3.8(a) at a strain rate of 1.0 s^{-1} and in Figure 3.8(b) at strain rate of 10 s^{-1}. JC-1 model predicts lower stress values than JC-2 model at increasing deformation temperatures.

Table 3.2. Model parameters of AISI 1045 steel.

Parameters	**AISI 1045 (JC-1)**	**AISI 1045 (JC-2)**
Density, kg/m^3	7433	7433
Shear modulus, GPa	14.2	14.2
Melting temperature, °C	1500	1500
Reference temperature, °C	900	25
Specific heat, $J/kg \cdot °C$	460	460
$C_{1,}$ (equation of state)	$15.7x10^9$	$15.7x10^9$

Table 3.3. The JC model parameters of AISI 1045 steel.

Material	**A (MPa)**	**B (MPa)**	**c**	**n**	**m**	**EPSO***
AISI 1045 (JC-1)	105.84	198.61	0.085	0.331	0.52	1
AISI 1045 (JC-2)	451	706	0.018	0.331	0.52	0.001

*Quasi-static threshold strain rate; the highest effective plastic strain rate, which indicates there is no need to adjust rate effects on the flow stress below this value.

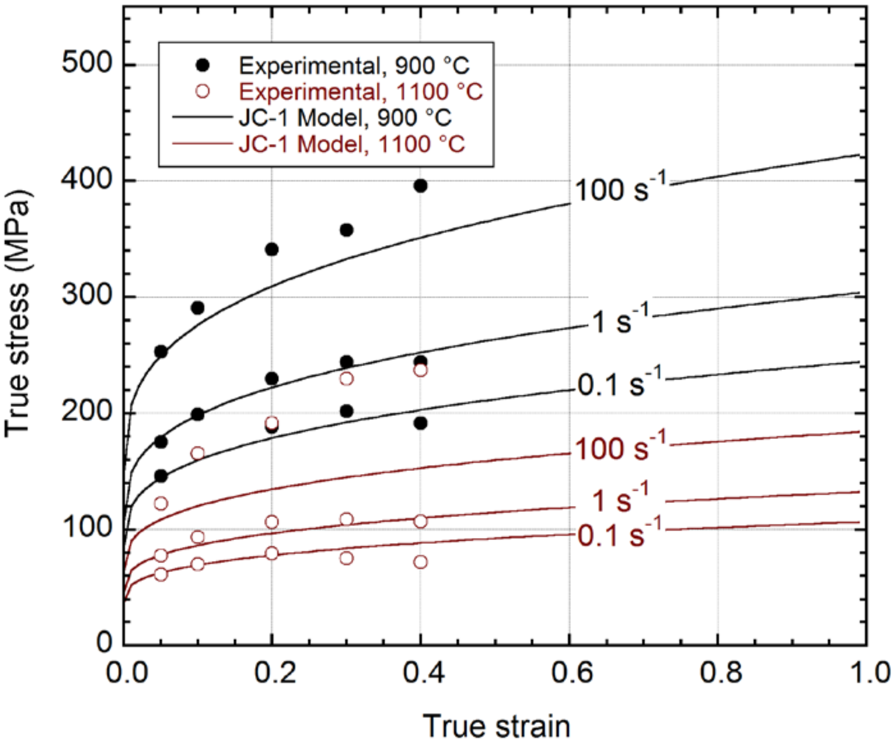

Figure 3.5. Model and experimental flow stress-strain curves of 1045 steel at various strain rates and at 900 and 1100 °C.

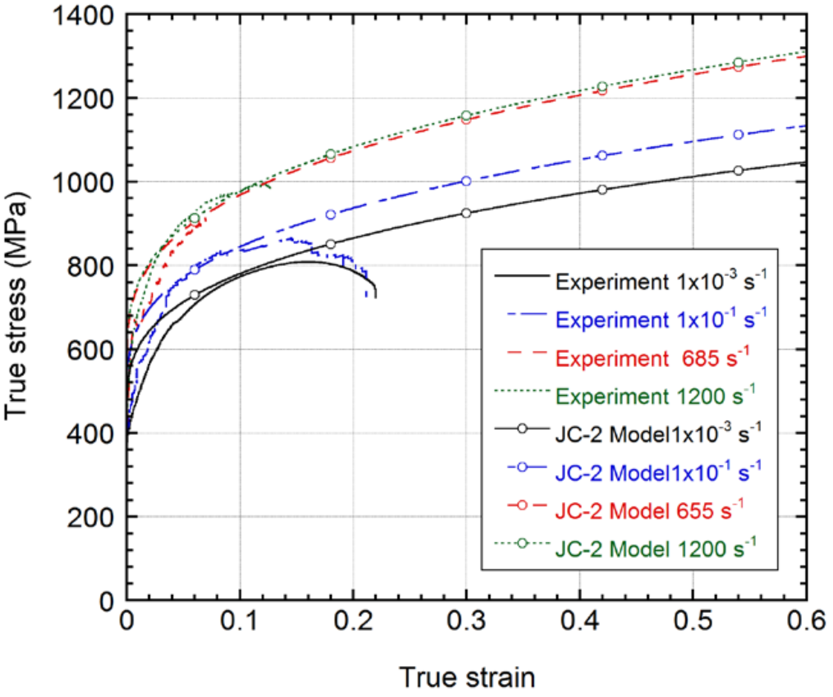

Figure 3.6. JC-2 model and experimental flow stresses at various strain rates at room temperature.

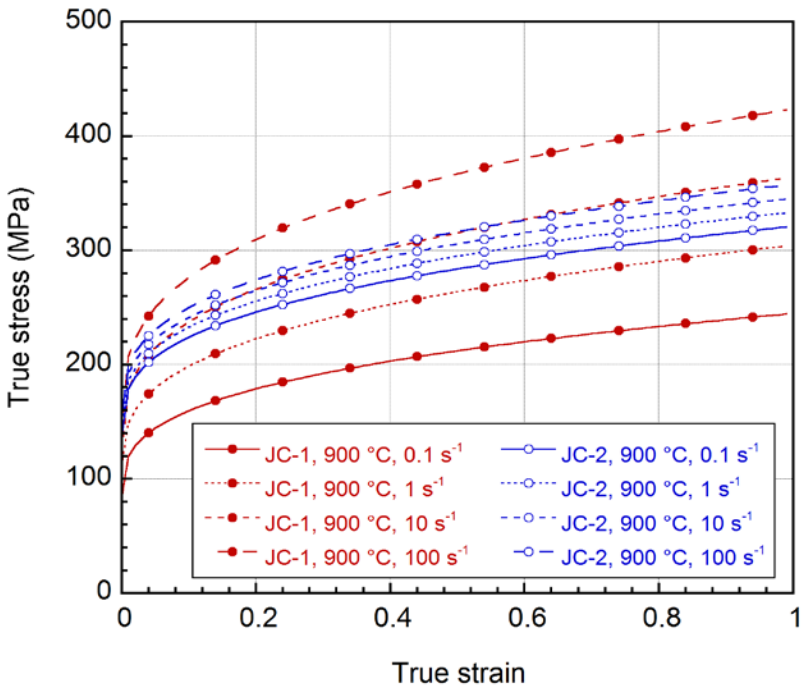

Figure 3.7. The stress-strain curves of JC-1 and JC-2 model at different strain rates at 900 °C.

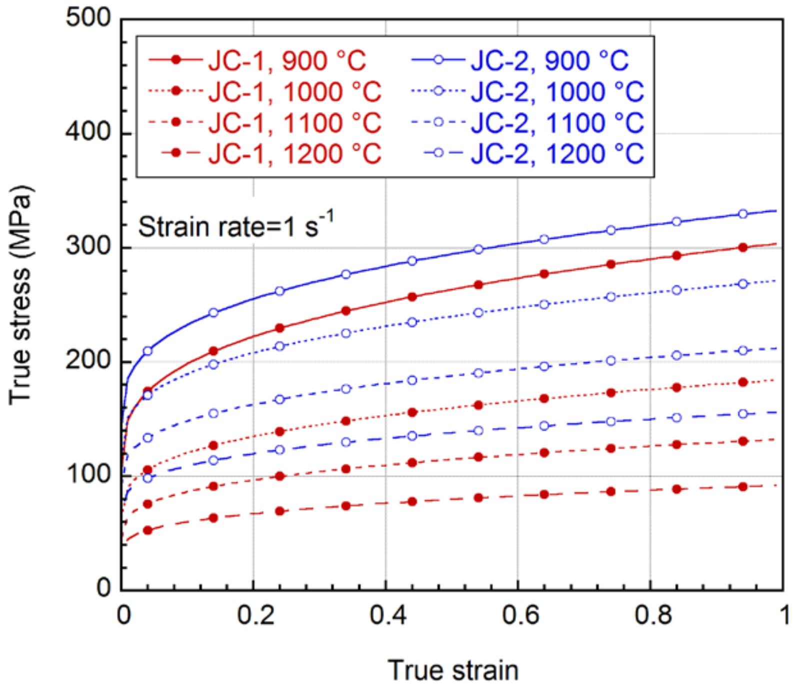

(a)

Figure 3.8. The flow stress-strain curves of JC-1 and JC-2 model at different temperatures at (a) 1 and (b) 10 s^{-1}.

(cont. on next page)

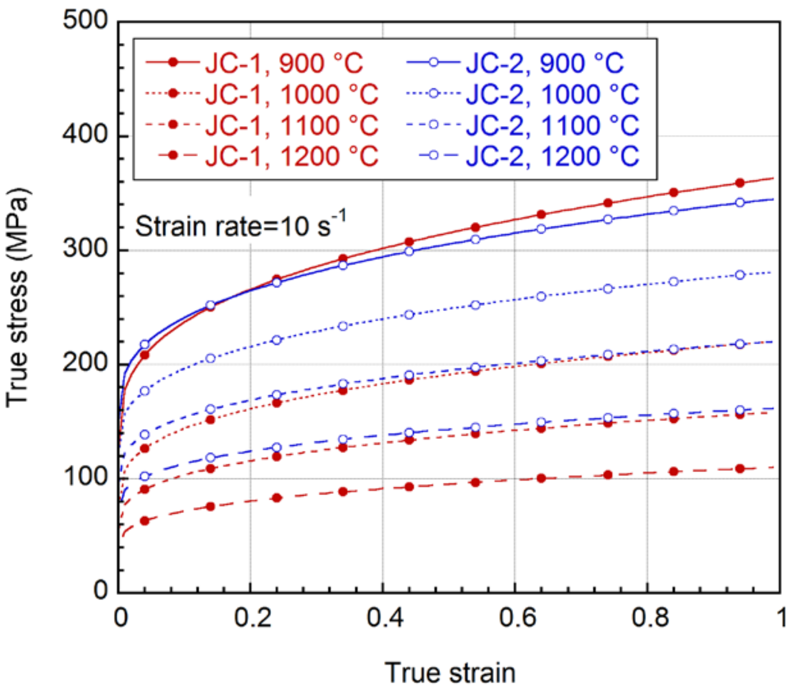

(b)

Figure 3.8. (cont.)

3.1.2. Ti6Al4V

The model and determined JC flow parameters for Ti6Al4V between 25-800 °C are tabulated in Table 3.4 and Table 3.5. This model is referred as to JC-1 in the thesis. The determined JC flow parameters between 800-1100 °C are further tabulated in Table 3.5. This model is referred as to JC-2 in the thesis. Figure 3.9(a) shows the predicted flow stress-strain curves at varying strain rates at 25 °C using JC-1 model and Figure 3.9(b) shows the predicted flow stress-strain curves between 900-1100 °C at a strain rate of 1x10^{-3} s^{-1} using JC-2 model. The damage parameters are tabulated in

Table 3.6. Figure 3.10 shows the model prediction of fracture strain as function stress triaxiality at 25 and 500 °C at 1x10^{-3} s^{-1} and at 25 °C at 1x10^{-1} s^{-1} together with corresponding experimental fracture strain values. As is seen in the same figure, model and experimental fracture strain values are agreed well at increasing temperatures and strain rates.

Table 3.4. Material model parameters of Ti6Al4V.

Parameters	**Ti6Al4V (JC-1)**	**Ti6Al4V (JC-2)**
Density, *kg/m*^{3}	4330	4330
Shear modulus, GPa	44	44
Melting temperature, °C	1663	1663
Reference temperature, °C	25	800
Specific heat, *J/kg*·°C	526.3	526.3
$C_{1,}$ (equation of state)	$42.19x10^9$	$42.19x10^9$

Table 3.5. The JC material model parameters of Ti6Al4V.

Material	**A (MPa)**	**B (MPa)**	**c**	**n**	**m**	**EPSO**
Ti6Al4V (JC-1)	927	1062	0.0167	0.6214	0.753	0.001
Ti6Al4V (JC-2)	30	50	0.0167	0.6214	0.423	0.001

Table 3.6. The JC damage model parameters of Ti6Al4V.

D_1	D_2	D_3	D_4	D_5
0.294	8.63	-8.4	-0.0213	4.22

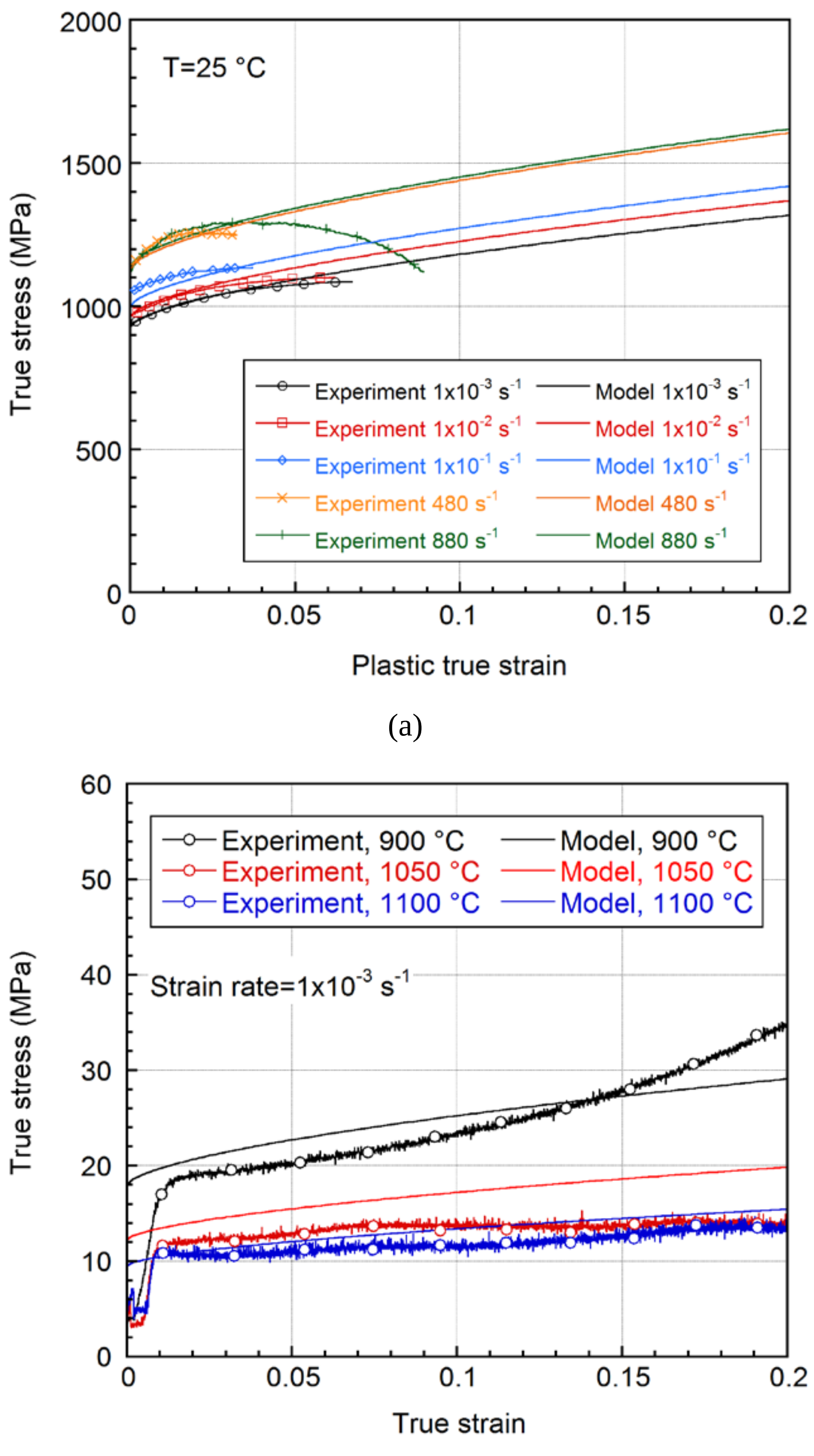

(a)

(b)

Figure 3.9. The predicted flow stress-strain curves (a) at varying strain rates at 25 ^{o}C using JC-1 model and (b) between 900-1100 °C at a strain rate of 1x10^{-3} s^{-1} using JC-2 model.

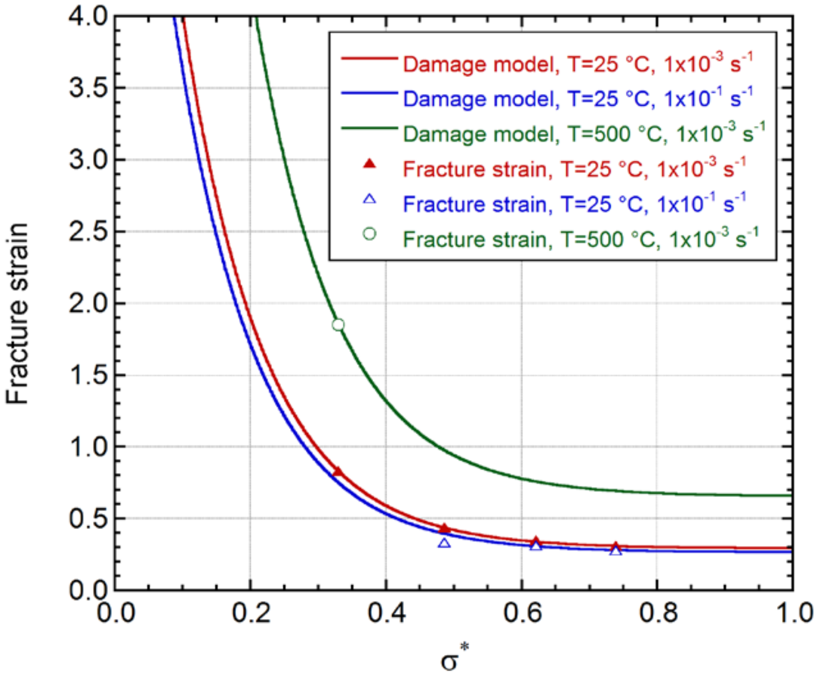

Figure 3.10. The model predicted fracture strain as function of stress triaxiality at 25 and 500 °C at $1x10^{-3}$ s^{-1} and at 25 °C at $1x10^{-1}$ s^{-1} together with the corresponding experimental fracture strain values.

3.2. CWR of AISI 1045 Steel and Ti6Al4V

The CWR experiments for model verifications were performed in a CWR machine at the Physical Technical Institute of NAS Belarus. The machine is shown in Figure 3.11 and a furnace next to the machine is used to heat the work piece at prescribed CWR temperature. The CWR mill parameters are as follows: the maximum lateral power: 10 tons, the maximum speed of the tool: 25 m s^{-1}, the maximum power consumption: 60 kW and the diameter of the workpiece: 6-50 mm and the length of the workpiece: up to 400 mm, the maximum productivity: 600 parts h^{-1}, and the tool life: over 500000 parts. The flat wedge type tool used in the experiments is shown in Figure 3.12. In a typical experiment, the bottom wedge tool was kept stationary and the upper wedge tool moved laterally with a rolling speed of 235.2 mm s^{-1}. The total deformation duration at this speed is about 1.25 s. The tool geometrical parameters were as follows: $\alpha=35^o$, $\beta=2.35^o$, $\delta=1.16$, the stretching zone length=220 mm, the sizing zone length=55 mm and the knifing zone length=19 mm. A small reduction ratio was chosen in the experiments in order not to damage the tooling. The studied AISI 1045 steel and Ti6Al4V alloy workpiece diameter and length are 18 and 60 mm, respectively. Before CWR process, the workpiece was heated using an induction furnace for 5 minutes. The CWR was performed at temperatures between 25 to 750°C. The pictures of the deformed Ti6Al4V workpiece at various temperatures are shown in Figure 3.13.

Figure 3.11. CWR machine used in the experiments.

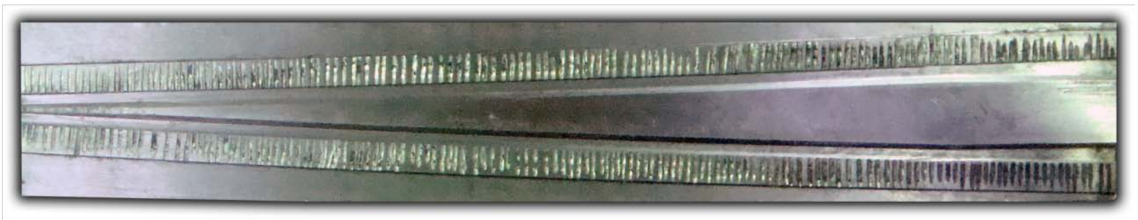

Figure 3.12. The tool (Tool-1) used to verify JC material models of 1045 steel and Ti6Al4V.

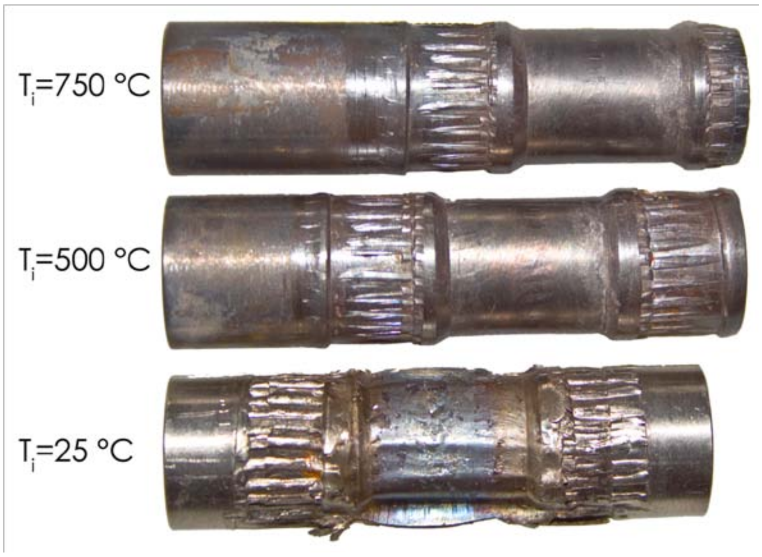

Figure 3.13. The pictures of Ti6Al4V workpiece after CWR process at different initial temperatures (T_i=25, 500 and 750°C).

A flat wedge type CWR machine, which is currently operated at the Physical Technical Institute of NAS Belarus to manufacture 1045 steel rolled parts, is shown in Figure 3.14. The machine consists of three major parts: an induction furnace, mainframe and flat wedge tools. A furnace next to the machine is used to heat the workpiece at a prescribed CWR temperature (Figure 3.14). The hot-rolled 1045 steel workpieces are heated in an induction furnace to the temperature of 1150 °C for 10 minutes and then were transferred to the CWR machine. During the rolling process, the bottom wedge tool is stationary, while the upper tool moves tangential to the workpiece. The AISI 1045 rolled parts are also shown on the inset of Figure 3.14. The bottom flat wedge tool used in the modeling is shown in Figure 3.15, together with the workpiece deformations at various stages of the rolling process and the tool geometrical parameters. The tool geometrical parameters are as follows α=30°, β=5.5°, guiding, stretching and sizing lengths of 37, 412 and 151 mm, respectively, and the workpiece length and diameter are 20 mm and 60 mm, respectively. The workpiece is deformed into a final length of 78 mm (Figure 3.16(a)) and the reduction ratios vary between 1.21 and 1.84 (Figure 3.16(b)). The workpiece deformation is designed to be sequential; the mid section is initially rolled followed by the rolling of the end sections of the workpiece. In the final step, the excess amount of material is removed by the side cutters. The rolled parts are then machined into the final geometrical sizes. In a final step, the surfaces of the parts are induction hardened.

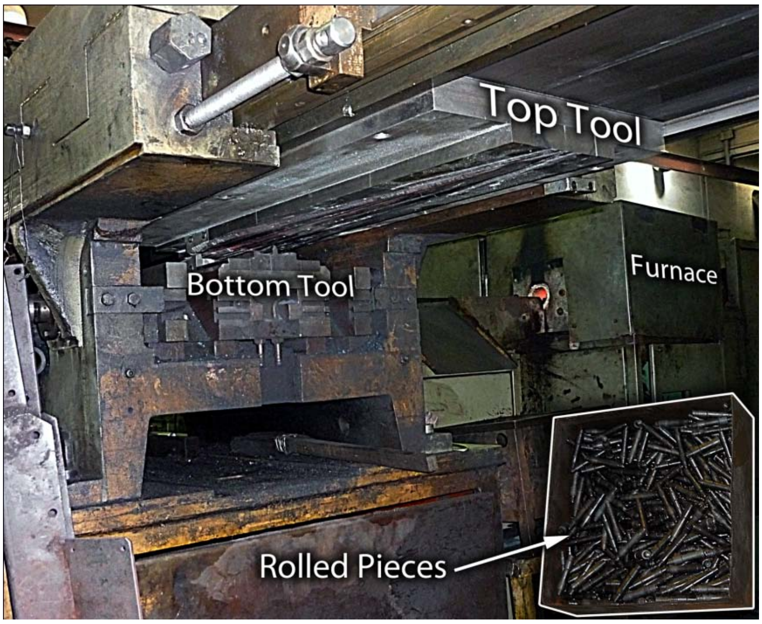

Figure 3.14. The CWR machine at the Physical Technical Institute of NAS (Belarus) and the rolled products.

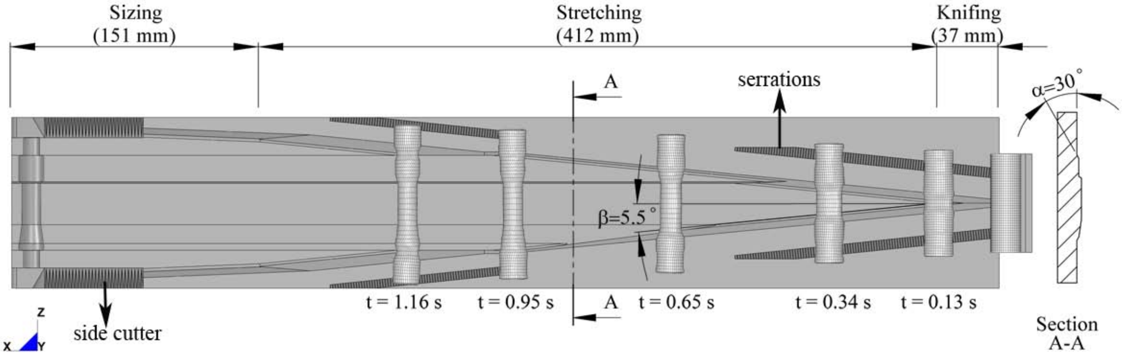

Figure 3.15. The geometrical parameters of the bottom tool and the deformation steps of the workpiece with respect to time.

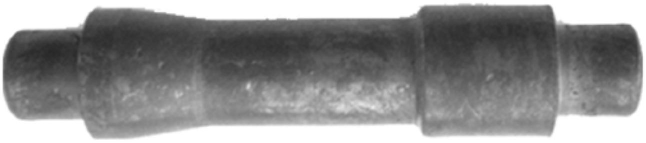

(a)

Figure 3.16. The picture of (a) 1045 steel workpiece before machining and (b) final deformed shape.

(cont. on next page)

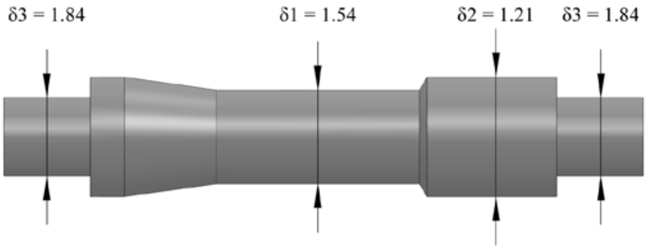

(b)

Figure 3.16. (cont.)

3.3. Force Measurement

A pressure gage connected to hydraulic cylinder was used to measure the tangential pressure on the workpiece. The gage reading was recorded using a camera with 30 fps, and then the pressure was read using a video capture program. The forces were calculated as a function of time from the pressure readings and the hydraulic cylinder diameter. Figure 3.17(a) and (b) show examples of pressure gage readings.

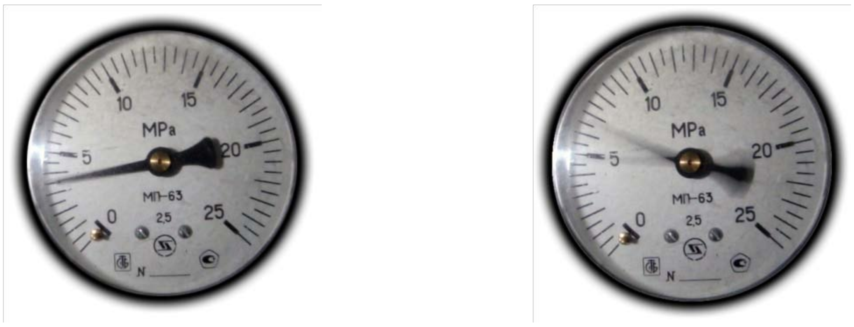

(a) (b)

Figure 3.17. The pictures of pressure gage readings (a) a clear and (b) blur motion shot.

3.4. Microscopic Investigation

The samples following the CWR process were cut into two parts along the long axis using an electro discharge machine. The cross-sections of the samples along the long axis before and after CWR process were then epoxy mounted as seen in Figure 3.18(a) and (b). These samples were sequentially ground using 120, 240, 320, 600, 800, 1200 and 2400 grit SiC papers. The final polishing was performed using SiC solutions down to 1 μm. The polished cross-sections of Ti6Al4V and 1045 steel samples were etched with Kroll's reagent (3 cm^3 of HF and 6 cm^3 of HNO_3 in 100 ml of H_2O) and 2% Nital solution, respectively. Microscopic analyses were performed on vacuum epoxy-mounted samples using an optical microscopy and a Philips XL30-SFEG scanning electron microscope (SEM) with an Energy Dispersive X-ray (EDX) analyzer.

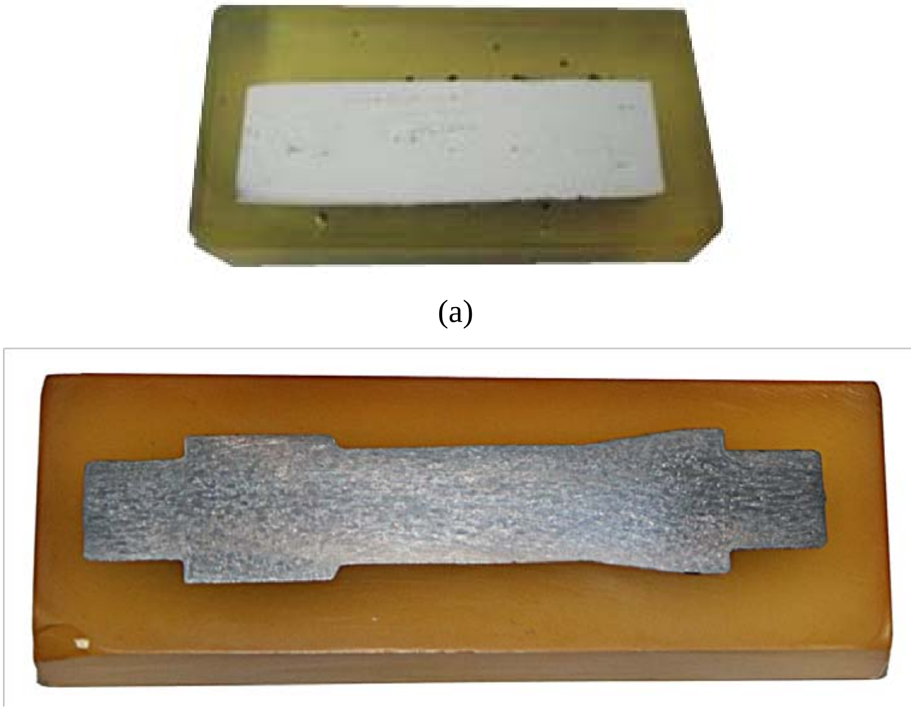

(a)

(b)

Figure 3.18. The mounted Ti6Al4V workpiece cross-section (a) before and (b) after CWR process.

CHAPTER 4

MODELING OF CWR

Three different flat wedge tool designs were modeled in this thesis. The first tool design (Tool-1) also called model testing tool was specially produced for CWR of Ti6Al4V and 1045 steel (Figure 4.1(b)). This tool was modeled for the verification of the JC material model parameters. The obtained numerical model tangential forces were compared with those of experiments performed at different workpiece temperatures. The second tool (Tool-2) was a basic flat wedge type tool geometry, which was used to model the effect of CWR geometrical parameters on the CWR process (Figure 4.2(b)). The last one (Tool-3) had a relatively complex tool design geometry, which is currently used in a real production line by Physical Technical Institute of NAS Belarus (Figure 4.3).In the modeling studies, three main steps were followed. These were (1) geometry modeling, (2) mesh generation, and (3) pre-processing of FEM. These steps are explained in detail in the following sections sequentially.

4.1. Geometry Modeling

First step of modeling is to design CWR parts in 3D environment by the use of a CAD program. These parts are flat wedge tools located tangentially to the workpiece at the top and bottom. In the actual process, serrations (Figure 4.1(b) and Figure 4.3) are present to obstruct the initial misalignment and misshapen of the final products by providing grips on the workpiece. The main purpose of modeling tools as surfaces (as seen in Figure 4.2(b) and Figure 4.3) instead of solid body (Figure 4.1(b)) is to lower the mesh discretization and consequently lower computational time in FEM solving process. The workpiece geometry is a cylindrical and throughout the thesis study, it is modeled as solid body (volume) in all simulations (Figure 4.2(a)). The workpiece dimensions are slightly changes from one to another. The radius of the workpiece is 9 mm for Tool 1 and 3, while it is 12 mm for Tool 2. The length of the workpiece is identical for all tools and it is 60 mm.

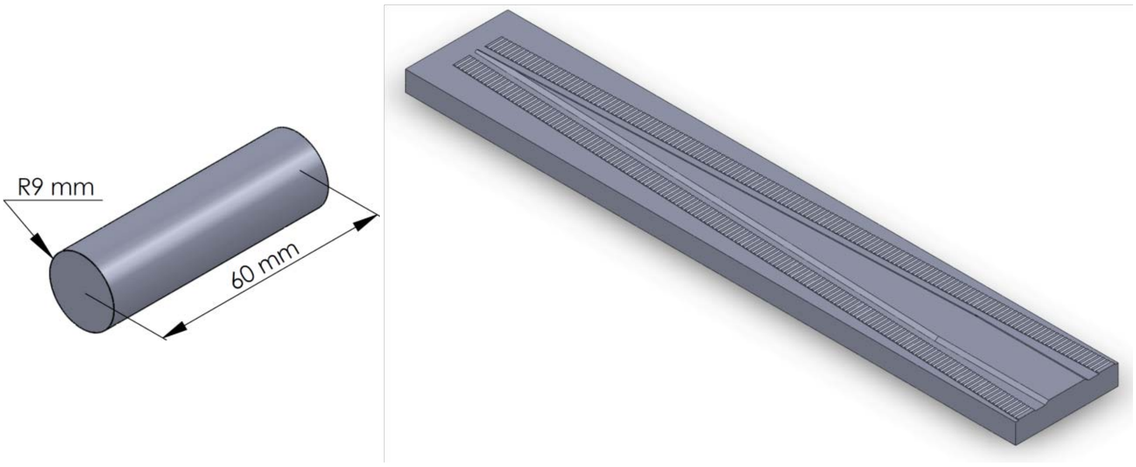

(a) (b)

Figure 4.1. (a) The workpiece and (b) Tool-1 designed for experimental verification of JC materials models of AISI 1045 steel and Ti6Al4V.

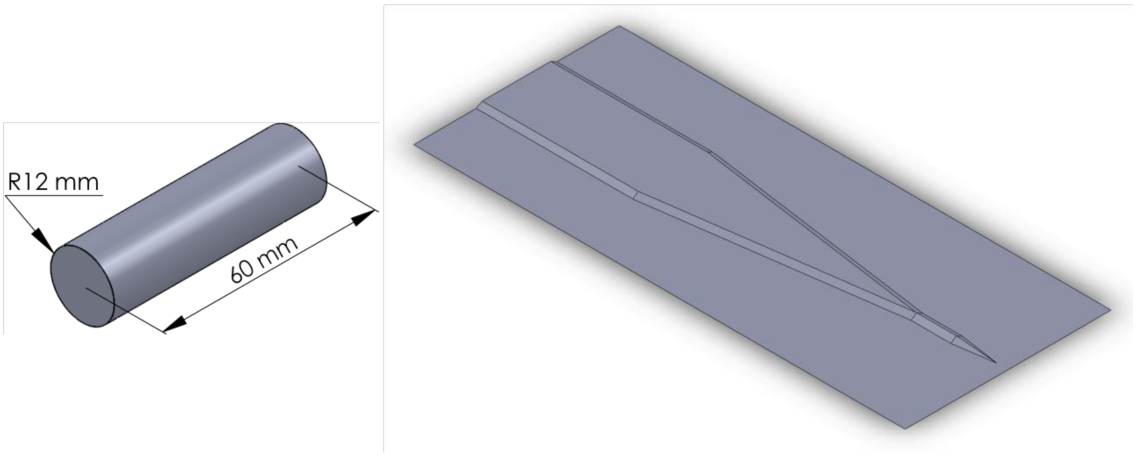

(a) (b)

Figure 4.2. (a) The workpiece and (b) Tool-2: basic flat-wedge type tool geometry used for parametric studies.

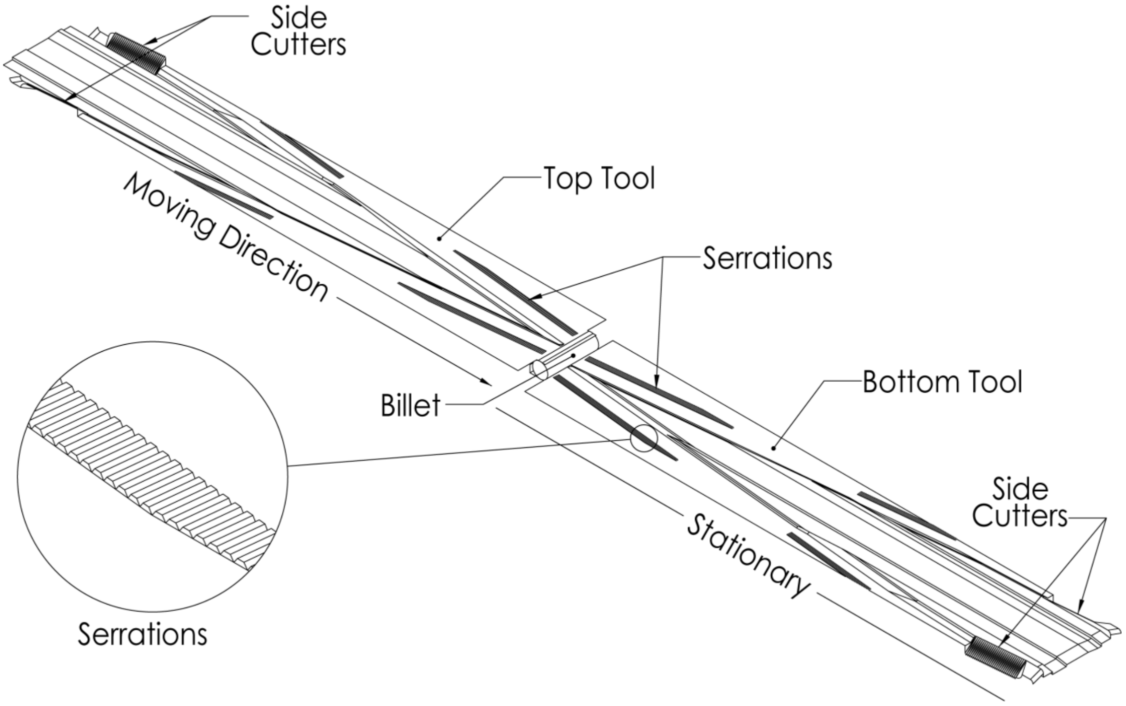

Figure 4.3. Assembly view of the complex tool geometry (Tool-3) used for the tractor shafts manufacturing by the Physical Technical Institute of NAS, Belarus.

The details of the Tool-1 geometry are shown in Figure 4.4. The tool accommodates serrations at both sides of the wedge and the guiding zone is eliminated. The forming angle is 35° and the stretching angle 2.34° and the reduction ratio 1.16. In Figure 4.5 shows the basic tool geometry of Tool-2. The tool has varying geometric parameters: α=7°, 8° and 10°, β=30°, 35° and 40°, and Δ_A=32%, 39% and 45% are used to determine the effect of process parameters. Tool-3 as shown Figure 4.6 is the most complex design. Figure 4.6 shows the ghost views of workpiece deformation steps over the Tool-3.

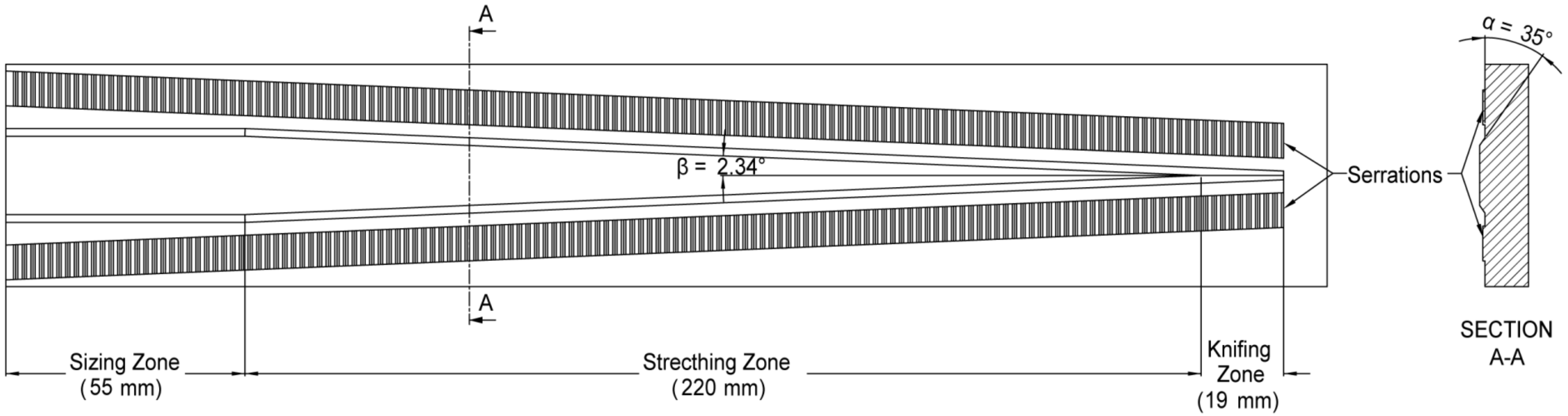

Figure 4.4. Technical drawing of the Tool-1, used for experimental verification.

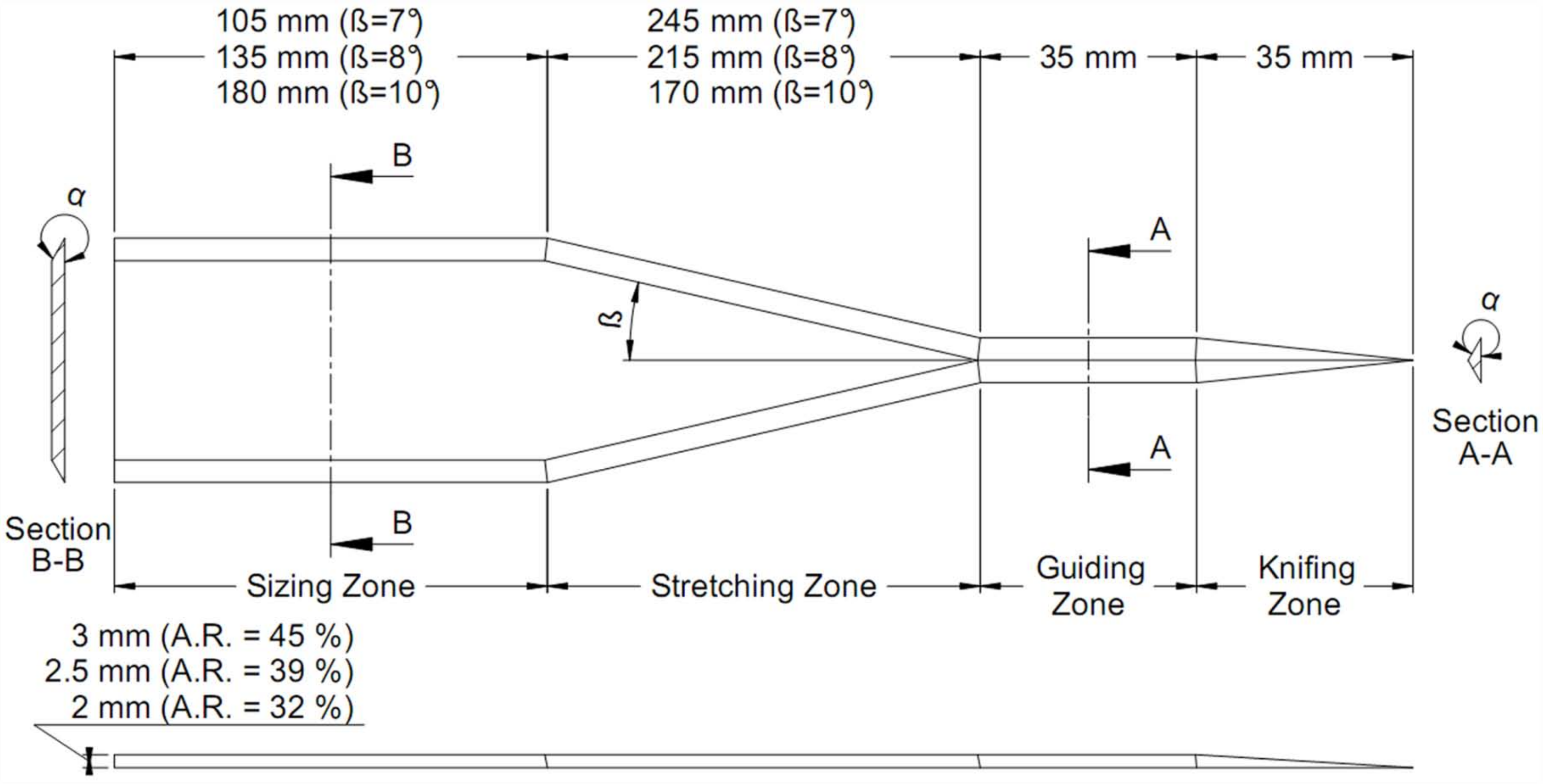

Figure 4.5. Technical drawing of the basic CWR tool.

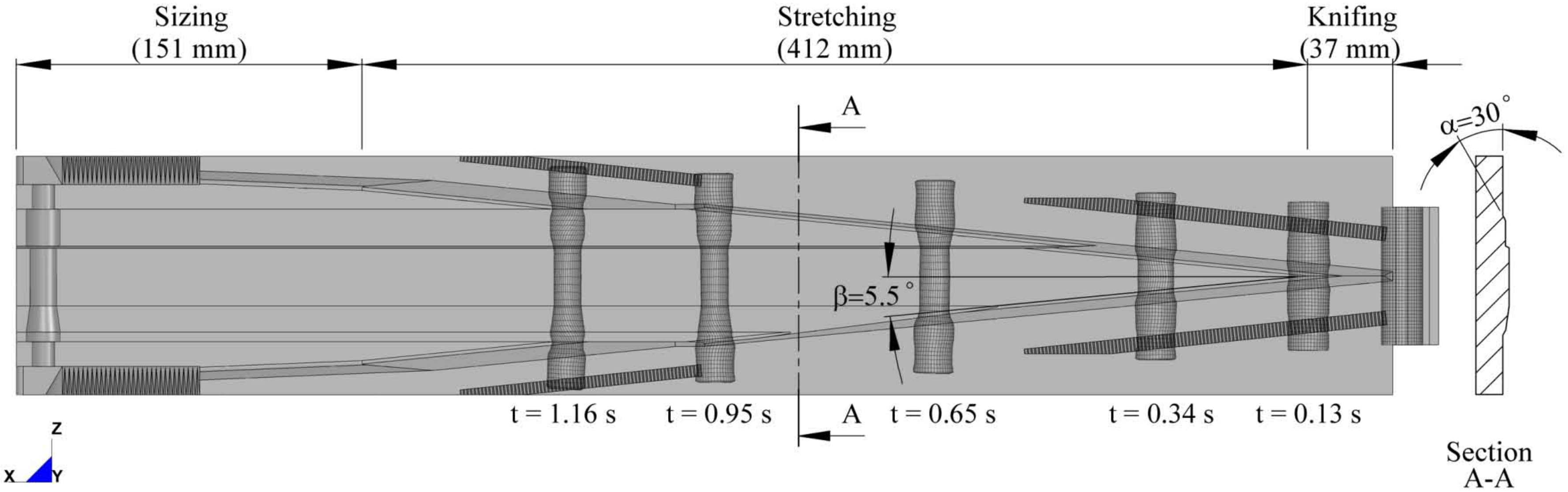

Figure 4.6. Illustration of deformation zones on tool geometry and ghost view of workpiece (workpiece) deformation steps.

4.2. Mesh Generation

The next step after designing the part geometries is to mesh discretization of the continuous surfaces and volumes into a set of shell (2D) and solid (3D) elements. In Figure 4.7, an illustration of assembled parts (Tool-2 and workpiece) after meshing process is represented. The tools were meshed by two different types of shell elements: tria (triangle) and quad (quadrilateral) shell elements. Quad shell elements (4-node) enable mapped discretization of the trouble-free surfaces while tria shell (3-node) elements are more suitable for complex surfaces to be meshed. The workpiece was meshed using hexahedron (8-node) solid elements.

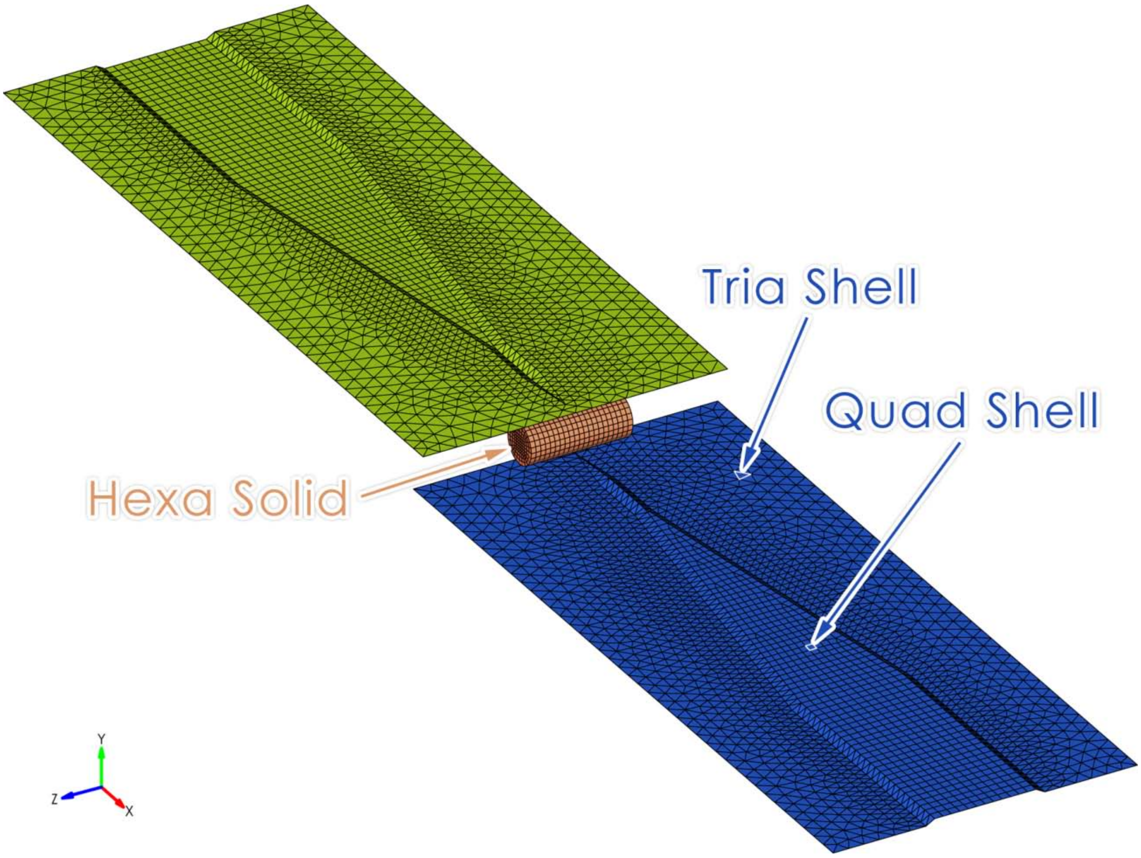

Figure 4.7. Assembly view of meshed model (Tool-2) designed for parametric studies.

The CWR design for experimental verifications was meshed with finer elements around the wedges and serrations in order to increase accuracy of the results (Figure 4.8). The main reason for using finer meshes on the tools was to prevent element penetrations. This was because the contact algorithm requires smaller meshes for rigid bodies (tools). In Figure 4.8, the mixed (tria-quad) type shell elements were used on tools (Tool-1) while the mesh density was changed occasionally. The complex design tools were meshed with fine tria-shell elements without changing the density (Figure 4.9). This cost high computational times, which were compensated by the fact that only two processes were simulated.

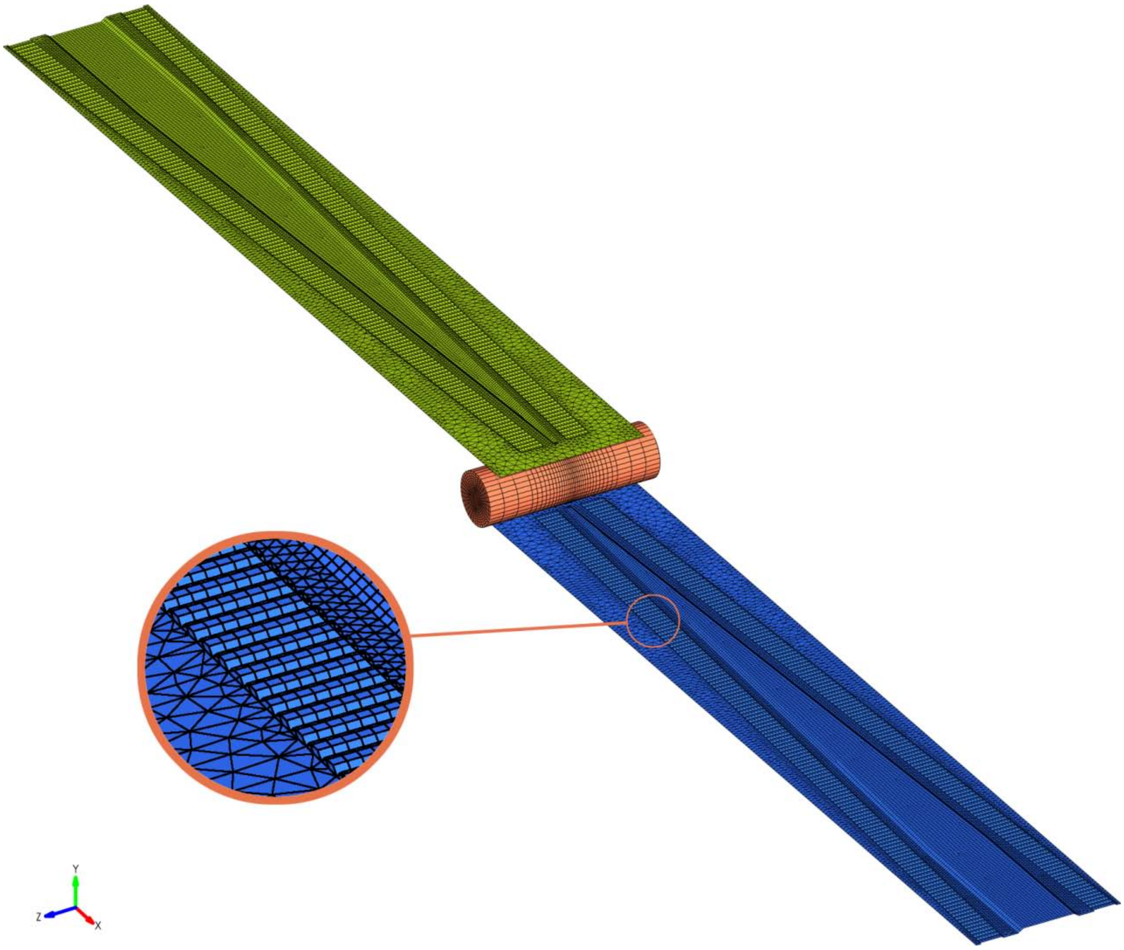

Figure 4.8. Mesh density and element type comparison for experimental CWR design (Tool-1).

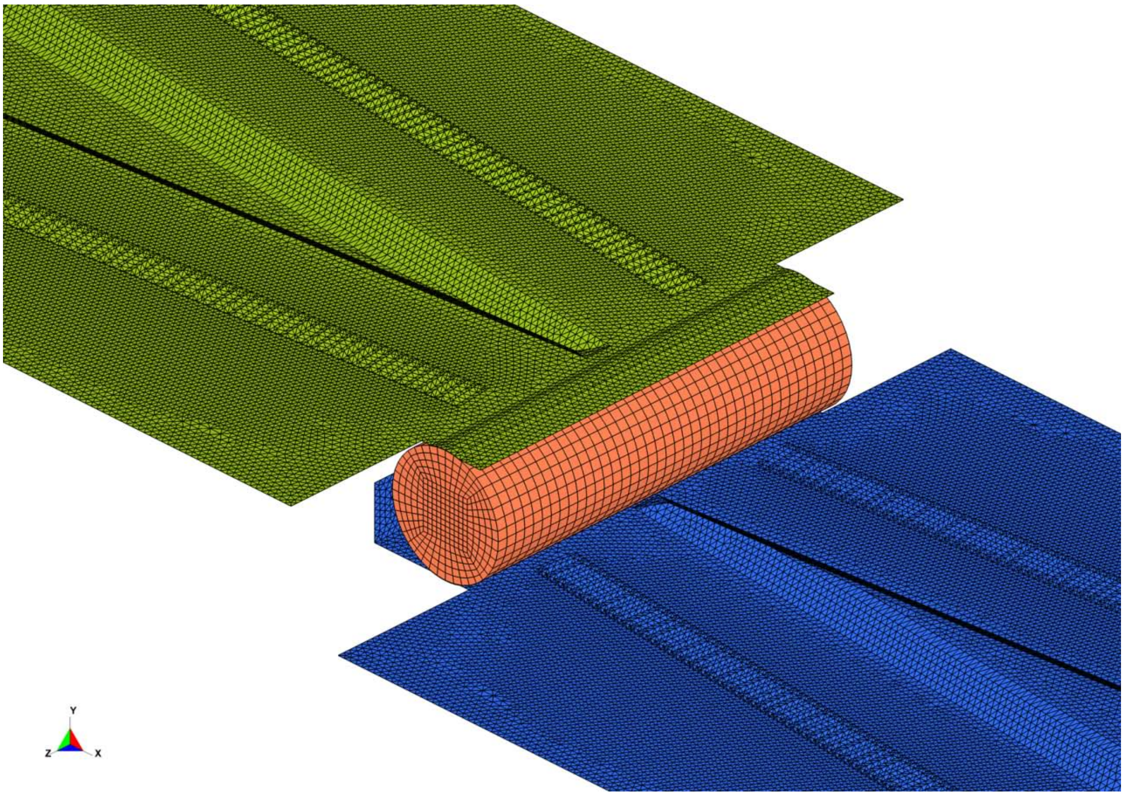

Figure 4.9. The complex CWR design (Tool-3) was meshed with finer elements.

In FEM solving process, about seventy percent of total CPU clock time (cost) was spent for element processing. To lower this cost, meshing was carried out studiously and different workpiece meshes were used for different processes. The middle section of the workpiece was meshed finer as it was the major deformation zone (Figure 4.10). The workpiece was also meshed by bell-curve style biasing along the z-axis to lower total element number. The xy cross section was meshed by butterfly type and the elements around the centroid were smoothed.

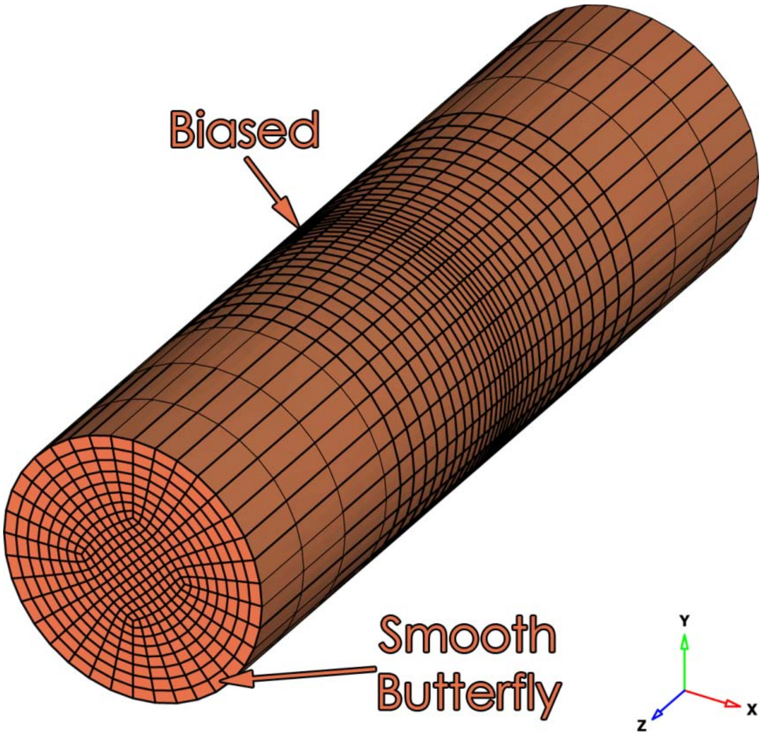

Figure 4.10. The meshed workpiece.

In Figure 4.11, the workpiece with two different mesh densities are shown. For parametric study, fifteen different simulations were performed and the computational time decreased by decreasing the mesh density of workpiece (Figure 4.11(a)). On the other hand, the complex design (Tool-3) was meshed with smaller elements (Figure 4.11(b)) to analyze the results in detail. The element numbers for each tool design are further tabulated in Table 4.1. As is noted in the same table, a higher number of shell elements were used in Tool-3.

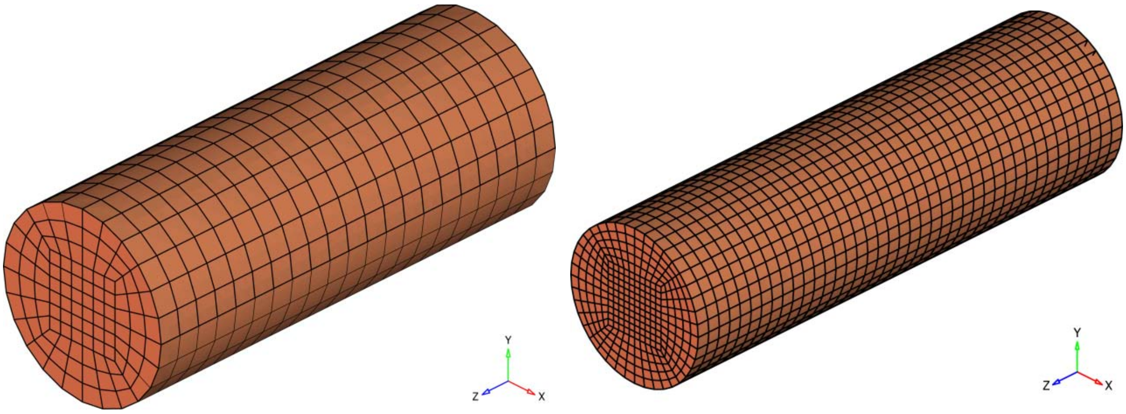

(a) (b)

Figure 4.11. The workpiece meshed with (a) coarse elements for parametric study and (b) fine elements for complex tool design (Tool-3).

Table 4.1. The number of elements for each CWR tool design.

Design	# of elements (shell)	# of elements (solid)
Tool-1	39886	13284
Tool-2	6772-7142	2268
Tool-3	360664	12000

The meshing of notched Ti6Al4V samples was made by pentahedral elements with six nodes (Figure 4.12). The first step for this procedure was to mesh the circle face by triangular elements and then drag those elements to form prism. This procedure enabled the overall mesh to be scaled at lower radius without changing the distribution. The Split Hopkinson Pressure Bar was meshed by the same element types but using relatively coarse mesh compared to the notched samples. The assembly views of meshed notch samples of R=2, 3 and 6 mm in are shown sequentially in Split Hopkinson Pressure Bar in Figure 4.13(a-c), respectively.

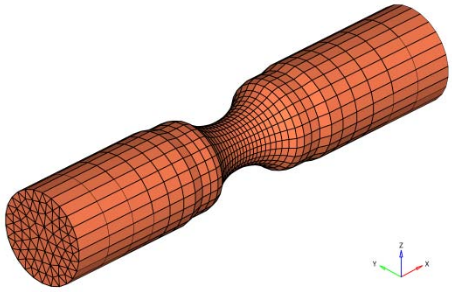

Figure 4.12. Meshed notched sample (R=6 mm) model.

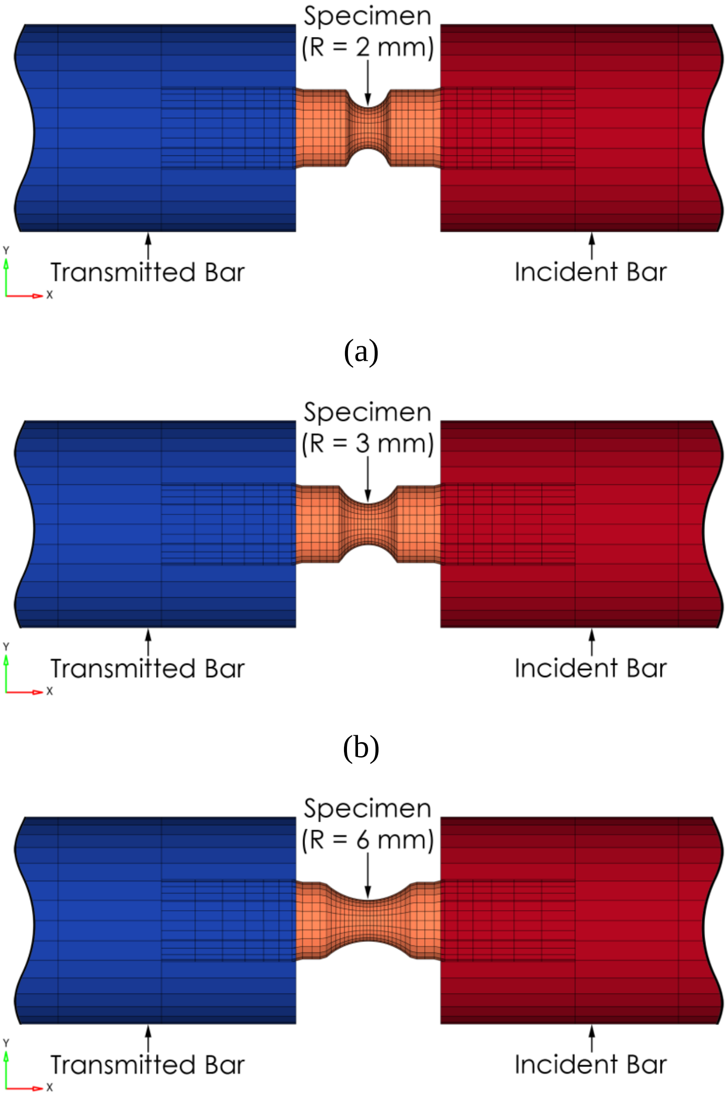

(a)

(b)

(c)

Figure 4.13. The assembly view of the meshed notch samples: (a) R=2 mm, (b) R=3 mm and (c) R=6 mm.

4.3. Pre-processing of FEM model

FEM calculations were implemented using LS-DYNA V971 R4.2.1 (R4.53450) solver. The CWR models were prepared using LS-PrePost software in order to write the input file in a specific format compatible with the solver. The input file was named as keyword file and this file contained all the FEM model information needed by the solver. The output file was generated by the solver and the post-processing was performed by LS-PrePost over again. In the following sections, the pre-processing steps of FEM model are explained.

4.3.1. Material Models

The CWR FEM model consisted of three parts; one of which was workpiece (workpiece) and the other two were the top and bottom tools. The first step was to define material models for these parts. The workpiece was modeled by JC material model and the tools as rigid bodies. In CWR process, the workpiece experiences varying strain rates over a large range and the material softening occurs because of the adiabatic temperature increase due to plastic deformation. In addition, this model remains valid down to lower strain rates and even into the quasi-static regime. In order to model this problem, JC strain and temperature sensitive plasticity model was used. This model is further known as material type 15, which requires an equation-of-state when used with solid elements. The rigid material model was used for CWR tools in order to reduce computational cost. The elements defined as rigid are bypassed from being processed and history variables are not stored in the memory. The inertial properties for tools were calculated the tool geometry and the corresponding density defined for the rigid material (tool). Young's modulus, E, and Poisson's ratio, υ were defined in order to determine sliding interface parameters when the rigid body interacts in a contact definition. In Table 4.2, user input requirements are detailed for each material model used in CWR model.

Table 4.2. Material models and corresponding user defined inputs.

Johnson and Cook	**Rigid**	**Thermal Isotropic**
Mass density	Mass density	Heat capacity
Shear Modulus	Young's Modulus	Thermal conductivity
JC parameters (A, B, c, m, and n)	Poisson's ratio	-
Quasi-static threshold strain rate	-	-
Failure parameters ($D_{1\ldots5}$)	-	-
Melting temperature	-	-
Room temperature	-	-

4.3.1.1. Material Model 15: Johnson and Cook Plasticity Model

The JC flow stress [38] is expressed as

$$\sigma_y = \left(A + B\bar{\varepsilon}^{P^n}\right)\left(1 + c\ln\dot{\varepsilon}^*\right)\left(1 - T^{*^m}\right) \tag{4.1}$$

where *A*, *B*, *c*, *n*, and *m* are the user defined input constants, $\bar{\varepsilon}^P$ is effective plastic strain,

$$\dot{\varepsilon}^* = \frac{\dot{\bar{\varepsilon}}^P}{\dot{\varepsilon}_0} \text{effective plastic strain rate for } \dot{\varepsilon}_0 = 1\ s^{-1} \tag{4.2}$$

$$T^* = \frac{T - T_{ref}}{T_{melt} - T_{ref}} \tag{4.3}$$

The damage parameter (fracture strain) is given by the following equation:

$$\varepsilon^f = \left[D_1 + D_2 \exp D_3\sigma^*\right]\left[1 + D_4 \ln\dot{\varepsilon}^*\right]\left[1 + D_5 T^*\right] \tag{4.4}$$

where, D_i $i=1,\ldots,5$ are input constants and σ^* is the ratio of pressure divided by effective stress:

$$\sigma^* = \frac{P}{\sigma_{eff}} \tag{4.5}$$

The fracture occurs when the damage parameter

$$D = \sum \frac{\Delta \bar{\varepsilon}^P}{\varepsilon^f} \tag{4.6}$$

reaches the value 1.

4.3.1.2. Equation of State: Linear Polynomial

The linear polynomial equation of state in the internal energy per initial volume (E) is given by the following equation:

$$p = C_0 + C_1\mu + C_2\mu^2 + C_3\mu^3 + \left(C_4 + C_5\mu + C_6\mu^2\right)E \tag{4.7}$$

where, p is pressure and C_i, $i=0,\ldots,6$ are user defined constants, and

$$\mu = \frac{1}{V} - 1. \tag{4.8}$$

here, V is the relative volume.

4.3.2. Element Section

In CWR model keyword (input file), the element formulations, integration rules and shell thickness properties were defined by the “section” interface. The element formulation used for solid elements (CWR workpiece) was “constant stress solid element” with single point integration. The single point integration was selected as the workpiece undergoes large deformations during CWR. For fully integrated solid formulation, the elements with poor aspect ratios experience the shear locking that leads to an excessively stiff response. Another disadvantage of fully integrated elements is locking up in the constant volume bending modes when the Poisson’s ratio is close to 0.5. “Belytschko-Tsay” element formulation with one integration point was used for shell elements. It is a computationally more efficient alternative to “Hughes-Liu” shell element. For example, a Hughes-Liu shell element with five integration points requires five times more mathematical operations than a Belytschko-Tsay shell element. The Belytschko-Tsay shell element is a combination of co-rotational and velocity-strain formulation. In brief, the mathematical simplifications of these two kinematical assumptions make this formulation more efficient. For this reason, Belytschko-Tsay element formulation was selected for the explicit calculations in the thesis. A uniform thickness of 1 mm was defined for shell elements (CWR tools).

4.3.3. Hourglass

The main disadvantage of one-point integration elements is the zero energy modes, also known as hourglass modes. The elements with zero energy modes deform without any load. This problem was controlled by adding small artificial elastic stiffness to the elements. In one-point integration elements, the hourglass work is neglected in the energy equations, leading to a small energy loss. In the thesis, the hourglass energy was monitored for each simulation. The hourglass coefficient was 0.05 and the hourglass control type of “Flanagan-Belytschko stiffness form with exact volume integration for solid elements” was used in CWR models.

4.3.4. Time Step Control

Explicit (central difference) method was used for modeling the CWR process. During the solutions, a new time step size (Δt) was calculated as well as with the stresses and forces by looping over all the elements [38].

$$\Delta t^{n+1} = a \cdot \min\left\{\Delta t_1, \Delta t_2, \Delta t_3, ..., \Delta t_N\right\} \tag{4.9}$$

where *a* is scale factor and *N* is total number of elements. The critical time step size, Δt_{cr}, for solid elements was calculated from

$$\Delta t_{cr} = \frac{l}{Q + \sqrt{Q^2 + c^2}} \tag{4.10}$$

where, *l* is characteristic length, *c* is velocity of sound in material, and *Q* is a function of the bulk viscosity coefficients C_0 and C_1:

$$Q = \begin{cases} C_1 c + C_0 l \left|\dot{\varepsilon}_{kk}\right| & \text{for } \dot{\varepsilon}_{kk} < 0 \\ 0 & \text{for } \dot{\varepsilon}_{kk} \geq 0 \end{cases} \tag{4.11}$$

The calculated time step size was multiplied by a scaling factor of 0.9 in order to ensure the stability.

$$\Delta t = 0.9 \cdot \Delta t_{cr} \tag{4.12}$$

The time-step size parameters for different element types are listed in Table 4.3. Here, *E* is young's modulus, ρ is the specific mass density and υ is the Poisson's ratio.

Table 4.3. The time-step size parameters used in calculations.

Element type	**Characteristic length (*l*)**	**Velocity of sound in material (*c*)**
Solid	$l = \frac{\text{the element volume}}{\text{the area of the largest side}}$	$c = \sqrt{\frac{E(1-\upsilon)}{\rho(1+\upsilon)(1-2\upsilon)}}$
Shell	Smallest element length	$c = \sqrt{\frac{E(1-\upsilon)}{\rho(1-\upsilon^2)}}$

The mass scaling was performed by changing the mass density of the elements. In time-step control card, a negative value of “dt2msf” option was specified in order to change only those elements, whose critical time-step size was smaller than the specified one. This procedure enabled the computational cost to be lowered while providing the stability of the integrations. The mass added to the system was checked carefully so that the system was kept in realistic physical conditions.

4.3.5. Boundary Conditions

The thermo-mechanical analysis was solved by coupling of implicit (for thermal) and explicit (for mechanical) methods. The tool motions and the thermal conditions were modeled by the boundary card. The thermal properties were defined using “thermal-isotropic” material model. A set of workpiece (outer surface) segment was defined by the set card and the thermal convection was applied to this set by the boundary card. The initial temperatures were applied to set of nodes previously defined by the set card. In order to solve thermo-mechanical coupled analysis, “diagonal scaled conjugate gradient iterative” type of thermal (implicit) solver card was initiated.

The tool motions were modeled by the boundary prescribed motion card in LS-PrePost. In this card, the motion was applied to the tools as displacement, which was defined by a curve as function of time. Only the tangential displacement was applied to the top of Tool-1 and Tool-3 design. Both top and bottom tools were moved towards each other (in x-axis) by the same displacement in order to ensure the symmetry in Tool-2 design. Since this design was used in the parametric study, the serrations and the indent were excluded. In the actual process, the serrations and the indent apply a temporary compression to the workpiece just at the beginning of the process. The schematic of actual CWR process is shown in Figure 4.14. The workpiece is inserted to the bottom tool by the help of an indent, which functions to ensure that each workpiece is stayed stationary at the identical position with the previous one. The effect of serrations and the indent was adapted in the model by compressive tool displacement (in y-axis) applied to both top and bottom tools. Each tool was moved 0.5 mm towards to workpiece until the process time reached 0.1 second; afterwards, both tools stayed stationary until the end of the process.

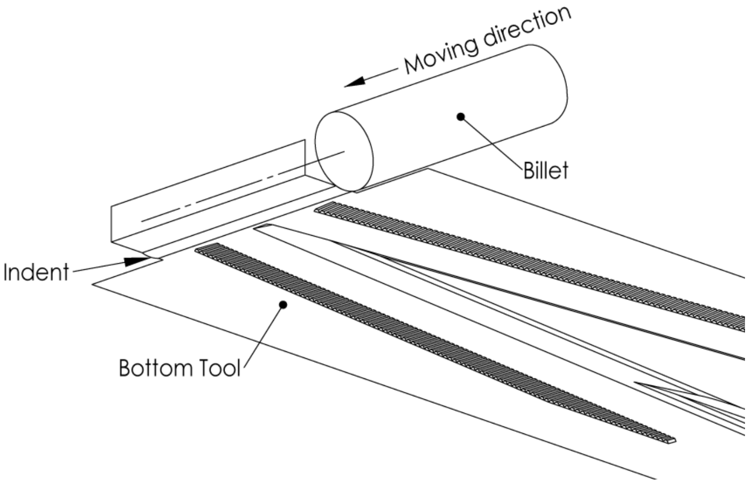

Figure 4.14. The schematic of the actual CWR process and workpiece installation using an indent on the bottom tool (Tool-3).

4.3.6. Contact

Two identical "surface to surface" contact algorithms were used to define the interactions between the workpiece (deformable, slave) and the tools (rigid, master). The contact algorithm was based on the sliding interfaces with penalty method. In this method, each deformable (slave) nodes are checked for penetrations through the contact (master) surface. An interface force is applied only in the case of penetration. The magnitude of this force is calculated by the amount of penetration. A simple formulation for this force is as follows:

$$F_{contact} = k \cdot n \tag{4.13}$$

where, k is the contact stiffness factor and n is the depth of penetration. The contact stiffness (k) is calculated for the shell elements as:

$$k = \frac{sf \cdot K \cdot A}{\max(shell\ diagonal)} \tag{4.14}$$

and for the solid elements as:

$$k = \frac{sf \cdot K \cdot A^2}{V} \tag{4.15}$$

Where, *sf* is a scale factor for the interface stiffness, *K* is the bulk modulus, *A* is the face area and *V* is the volume. In the thesis, the scale factor was taken 0.1. In simulations, the contact stiffness was calculated for both master and slave nodes, and the minimum value was used. The disadvantage of this method is that the explicit time integration may become unstable, if the high frequency vibrations are activated at higher stiffness values.

In the model, the friction coefficients were defined by the Coulomb formulation [39], which depended on the relative velocity (V_{rel}) of the surfaces in contact as,

$$\mu_c = FD + \left(FS - FD\right)e^{-DC\left|V_{rel}\right|} \tag{4.16}$$

where, *FD* is dynamic coefficient of friction, *FS* is static coefficient of friction, and *DC* is exponential decay coefficient.

4.4. Model Capabilities

The CWR process was modeled as coupled thermal (implicit) and mechanical (explicit) FEM using the LSDNYA commercial software. The thermal and the mechanical solvers were implemented simultaneously so that the mechanical work was converted into heat through plastic deformation.

4.5. Mass Scaling

Mass scaling was applied in few analyses to lower the computational time by increasing the time step size (Δt) of small elements. In mass scaling applied analyses, a nonphysical mass was added to the small elements to increase the density to increases the calculated critical time step size. Figure 4.15 shows the tool forces of the mass scaling applied and excluded simulations for comparison. The main differences between the simulations with and without mass scaling is the lack of the detailed force variations in the simulations without mass scaling, while both method give the similar magnitudes of the forces. Figure 4.16 shows the variations of the internal and kinetic energy as function of time. As seen in this figure, the kinetic energy is explicitly lower than the internal energy, which means that the mass scaling is reasonable for this simulation.

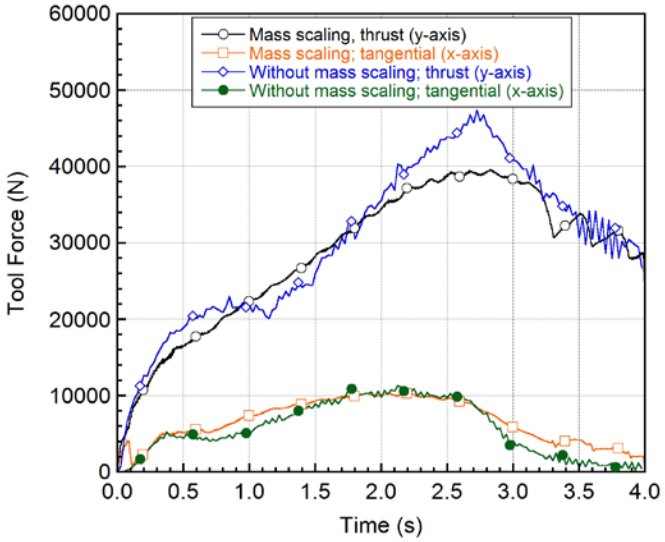

Figure 4.15. The effect of mass scaling on the tool forces in CWR: α=30° and β=8°.

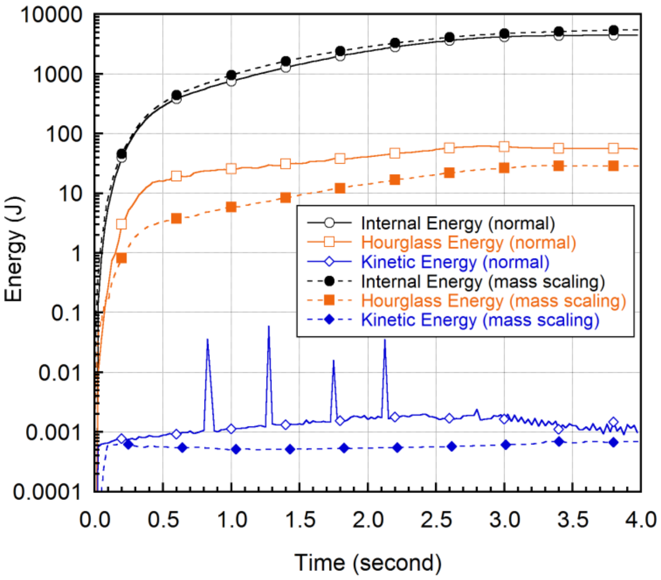

Figure 4.16. The energy comparison of normal analysis and mass scaling in CWR: α=30° and β=8°.

CHAPTER 5

RESULTS AND DISCUSSION

5.1. Model Verification

Numerical model and experimental incident and reflected stresses of the SHPB testing of 2 mm notch size sample at a striker velocity of 15.3 m s^{-1} are shown in Figure 5.1. In the numerical model, the incident and transmitted waves were measured 1.2 m away from the specimen-bar interface, the same as with the experiments. The experimental stresses in the same figure were shifted in the time scale with respect to numerical stresses for comparison. It should be noted that, the tested sample fractured at the point of the maximum transmitted wave. The fracture initiation was noted as a sudden rise in the transmitted wave during the initial rise (Figure 5.1). The experimental and numerical stress values shown in Figure 5.2 are very similar to each other in shape and magnitude. Similar trends were also found in SHPB testing and in the modeling 3 and 6 mm notch size samples. Figure 5.2 shows the experimental and numerical force-displacement curves of the notched samples tested in SHPB. As the notch size increases, the corresponding fracture or maximum force decreases (Figure 5.2). The model and experimental force-displacement curves also showed very good correlations, except that the experimental force values showed sharp reductions in the force values at the onset of and following the fracture.

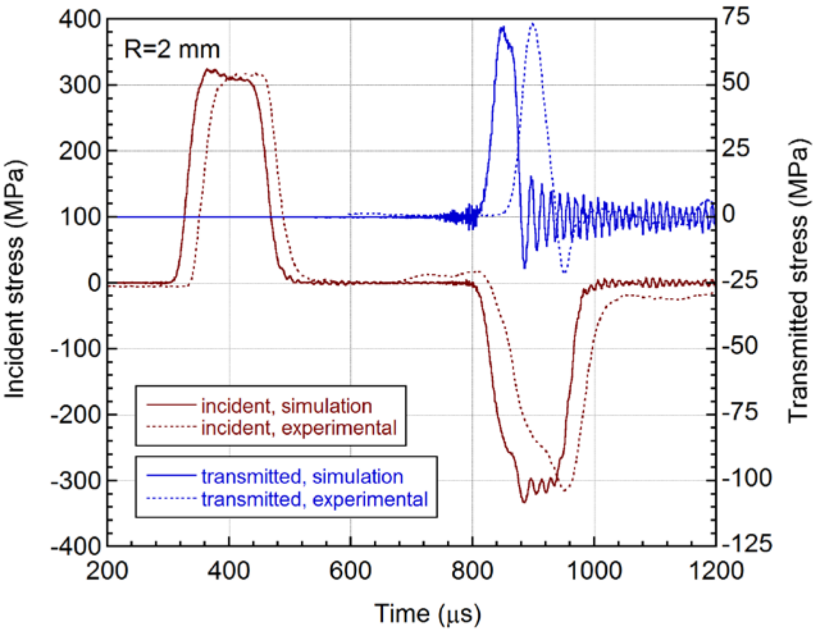

Figure 5.1. Numerical and experimental SHPB incident and transmitted stresses of R=2 mm sample tested at 15.3 m s^{-1} striker velocity (experimental stresses were shifted in time scale).

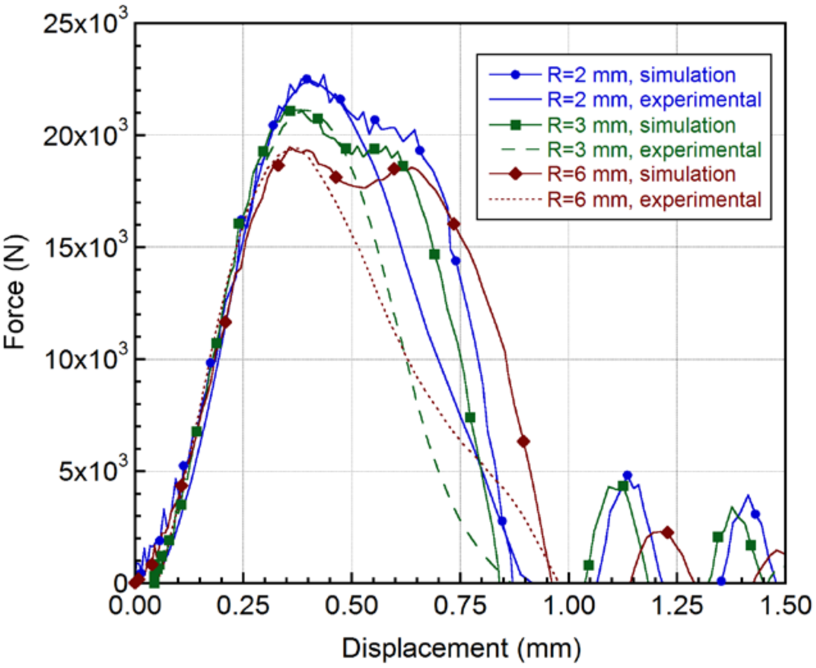

Figure 5.2. Numerical and experimental force-displacement curves of notched samples tested in SHPB at a striker velocity of 15.3 m s^{-1}.

Figure 5.3 shows the experimental force-displacement curves of 3 and 6 mm notch size and unnotched (diameter 4 mm) samples at dynamic and static strain rates. In the same figure, the corresponding static force-displacement curves of 3 and 6 mm notch size and unnotched samples are also shown. For 3 mm and 6 mm notch size static test samples, the displacement was directly read from the test machine displacement, while static unnotched sample displacement was determined using a video extensometer. The effect of strain rate on the fracture force of unnotched sample is clearly seen (Figure 5.3). As the strain rate increases, force increases and the fracture displacement decreases. The increase in the fracture forces of 3 and 6 mm size notch samples in dynamic tests are also seen in the same figure.

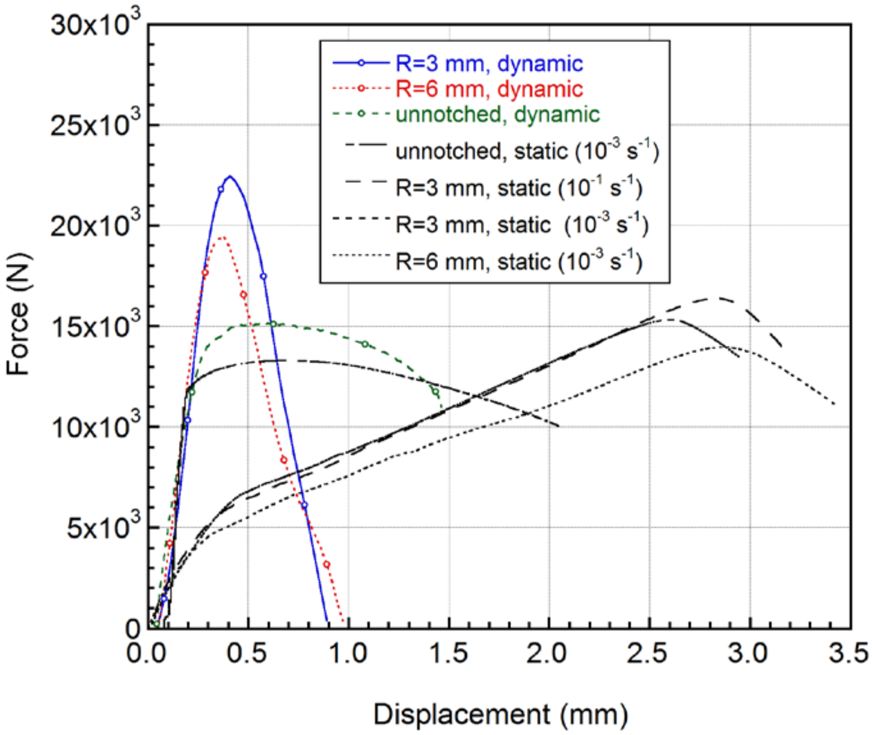

Figure 5.3. Experimental load displacement curves of notched and unnotched (diameter 4 mm) samples at dynamic static strain rates (note that static R=3 and 6 mm sample displacements were sample plus machine displacement).

In Figure 5.4, the effective strain distribution in the samples just before the fracture and at the fracture in the SHPB test simulations are shown. As it is expected, the highest effective strain is detected in 6 mm notch size sample. As the notch size decreases, the effective fracture strain decreases near the fracture site, which in agreement with the variation of the fracture strain with stress triaxiality. Figure 5.5 shows the effective strain rate distribution of the notched samples at t=586 μs in SHPB test simulation. At a constant time, the highest strain rate is seen in R=2 mm sample. Figure 5.6(a-c) further show the simulation and experimental fracture pictures of 2, 3 and 6 mm notch size sample tested in SHPB, respectively. The differences between model and experimental deformed shapes of the tested samples near the fracture side simply arise from the fact that the elements in the numerical model are deleted at the onset of fracture. This naturally results in a shorter final length of the model specimen than the real specimen does. Except near the fracture site, the deformed shape of the simulations and experiments are almost the same, showing the validity of the material flow stress and fracture strain model used.

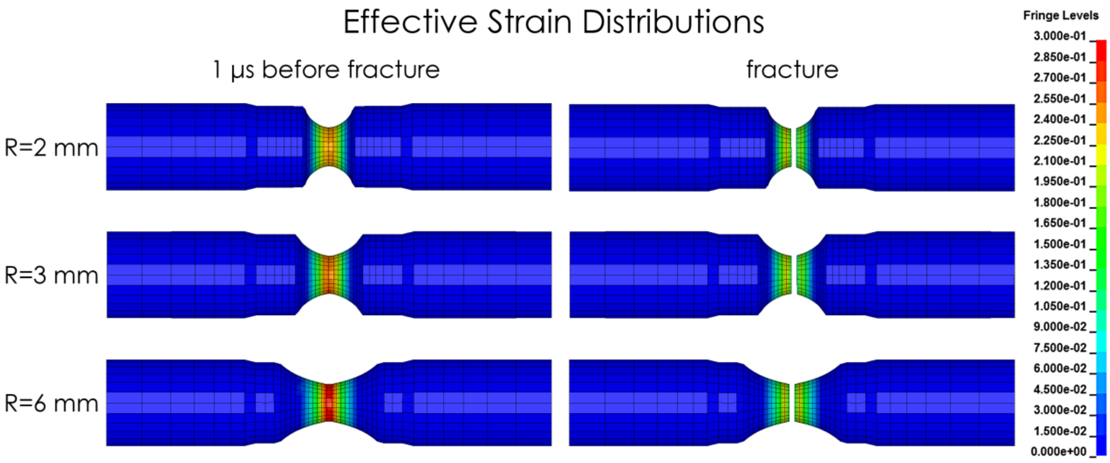

Figure 5.4. Effective strain distribution before and at the onset of the fracture in the SHPB notched sample test simulations.

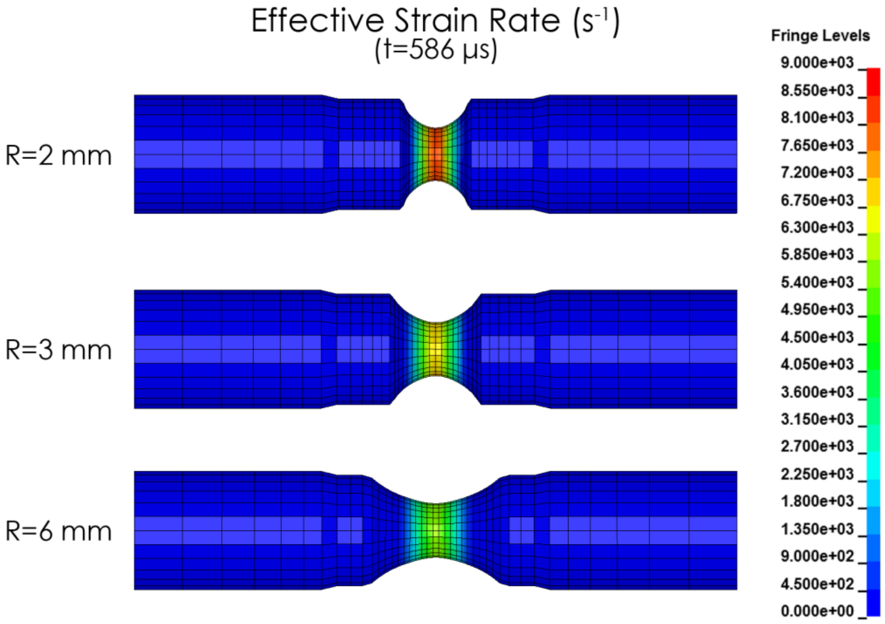

Figure 5.5. Effective strain rate distribution of the notched samples at t=586 μs in SHPB test simulations.

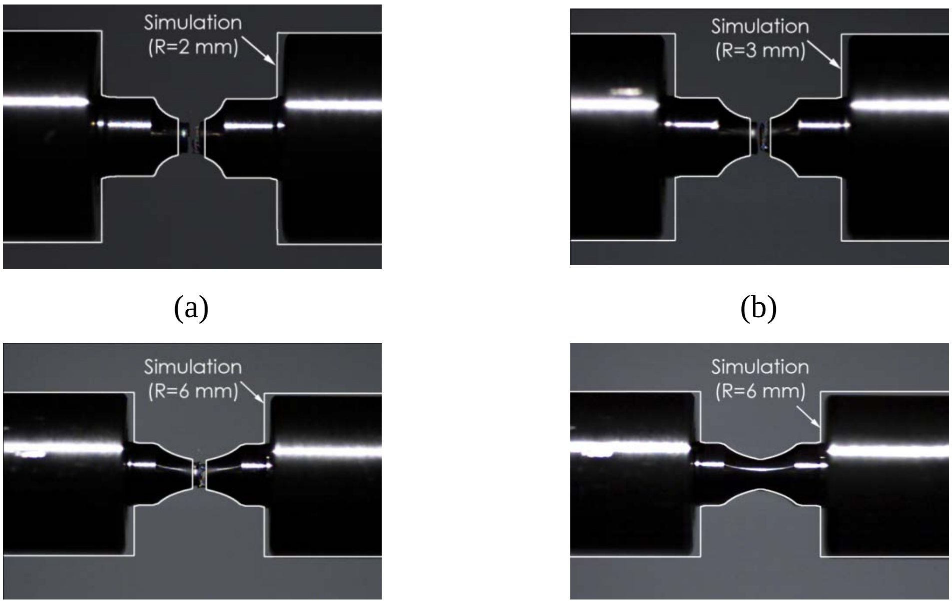

(a) (b)

(c) (d)

Figure 5.6. The pictures of the simulation and experimental fracture of the notched samples: (a) R=2 mm, (b) R=3 mm, (c) R=6 mm and (d) R=6 mm (before fracture) tested in SHPB.

5.1.1. Material Model

Figure 5.7(a) shows the variation of experimental and simulation tangential force of Ti6Al4V workpiece cross wedge rolled using Tool-1, at 25 °C initial workpiece and tool temperature. The models were implemented for JC-1 Ti6Al4V material model using static friction coefficient of 0.1 (dynamic friction coefficient 0.1) and 0.3 (dynamic friction coefficient 0.3), respectively. As is seen in Figure 5.7, the simulation and experimental tangential forces show well agreements at beginning and in the stretching zone, except near the end of the stretching zone. The simulation force values near the end of the stretching zone are however smaller than those of experimental force values. It is also noted that as the static friction coefficient decreases from 0.3 to 0.1 the difference between them increases. This shows that the friction coefficient between tool and workpiece varies with the time. The increase of the friction coefficient with deformation is attributed to the heating of the surface of the workpiece. The effect of increasing dynamic and static friction coefficients to 0.5 as shown in Figure 5.7(b) increases the force values near the end of the stretching zone, without significantly affecting the force values in the knifing and at the beginning of the stretching zone. This also proves that the friction coefficient increases during the CWR process. Figure 5.8 shows the variation of experimental and simulation tangential force of Ti6Al4V workpiece cross wedge rolled using Tool-1 at 500 and 750 °C initial workpiece temperature and 25 °C tool temperature. The models were implemented using JC-1 material model and static and dynamic friction coefficients of 0.5 and 0.5, respectively. The model and experimental tangential force values at increasing workpiece temperatures also show well agreements in the large extents of the stretching zone as shown in Figure 5.8. The difference between simulation and experimental force values is about 10% on the average, simulation forces being higher than experimental forces. It is also noted that both experimentally and numerically that although tangential force increases with increasing deformation duration when the workpiece initial temperature at 25 °C, it almost becomes constant when the workpiece initial temperature increases to 500 and 750 °C, except initial region.

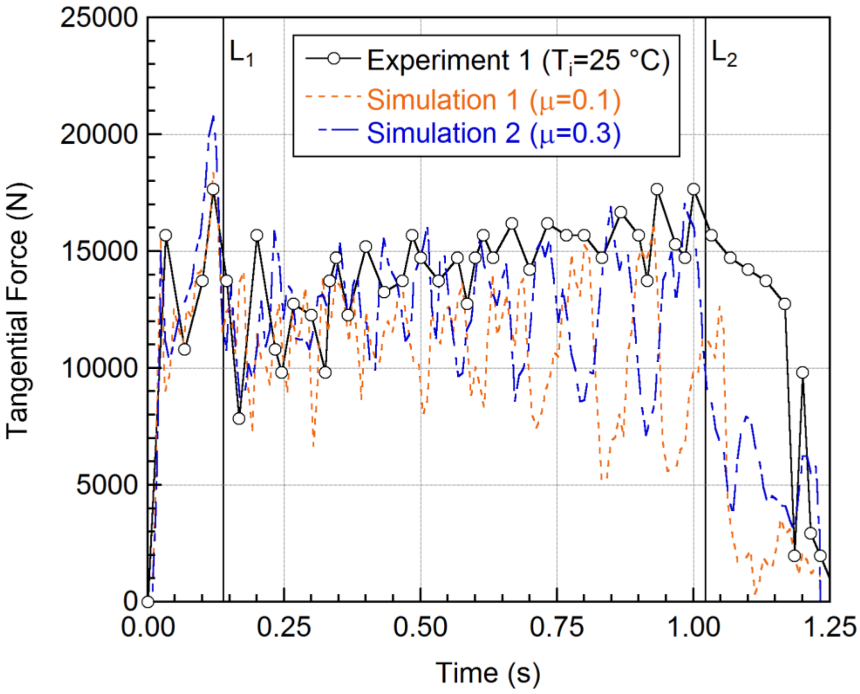

(a)

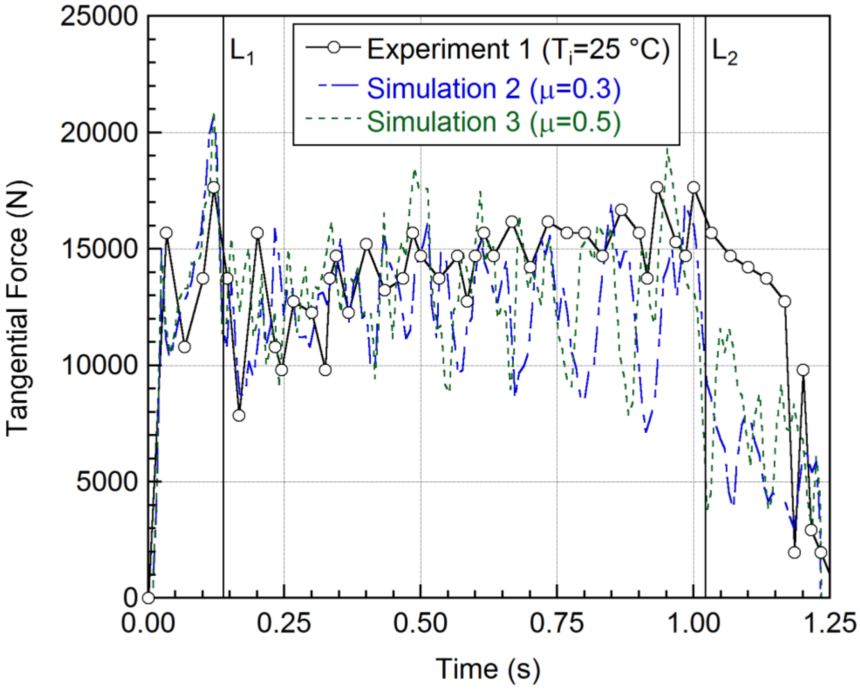

(b)

Figure 5.7. The variation of experimental and simulation tangential forces of Ti6Al4V workpiece, using Tool-1 at 25 °C workpiece temperature, static friction coefficients of (a) 0.1 and 0.3 and (b) 0.3 and 0.5.

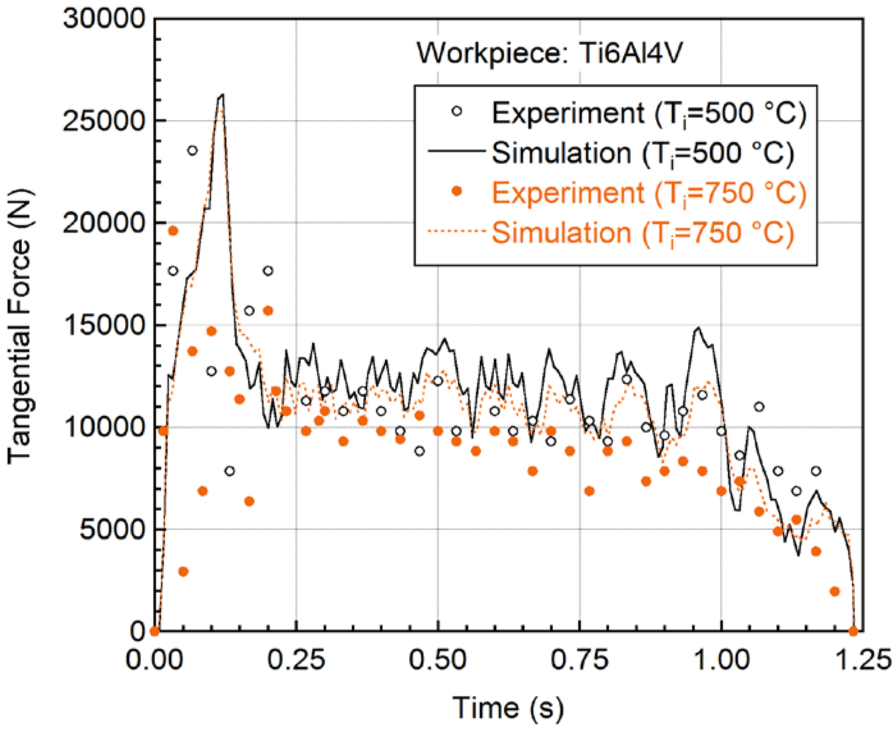

Figure 5.8. The variation of experimental and simulation tangential forces of Ti6Al4V workpiece cross wedge rolled using Tool-1 at initial workpiece temperature of 500 and 750 °C and the tool temperature of 25 °C.

The final pictures of the samples rolled at initial temperatures of 500 and 750 °C are shown in Figure 5.9(a) and (b), respectively. In the same figure, the deformed shapes of simulations are also shown for comparison (red lines). The simulation and experimental deformed shapes match well with each other. The variation of the workpiece properties with the CWR time is investigated for the center (element A), middle (element B) and surface (element C) as depicted in Figure 5.10.

The final temperature distribution of Ti6Al4V workpiece at the middle center (xy cross-section) and along the z-axis (yz cross-section), and the temperature of element A, B and C as function of rolling time at different friction coefficients for 25 °C initial workpiece temperature are shown in Figure 5.11(a) and (b), respectively. At the end of the CWR, the highest temperature is found in the stretching zone of the workpiece, in the shoulder area. The temperature at the center of the workpiece and in the shoulder is as high as 550 °C. It is also noted in Figure 5.11(b) that initially the temperature of the workpiece surface is higher than that of middle and center point. The friction is noted to produce an initial uneven temperature distribution throughout the workpiece, which gradually evens out afterwards as the deformation proceeds. As the friction coefficient increases, the workpiece surface temperature increases while the middle and center point temperatures decrease. The fluctuations in the surface temperature profile results from the fact that the workpiece contact and loss of contact with the tools. The surface temperature of the workpiece, depending on the friction coefficient varies between 400-550 °C.

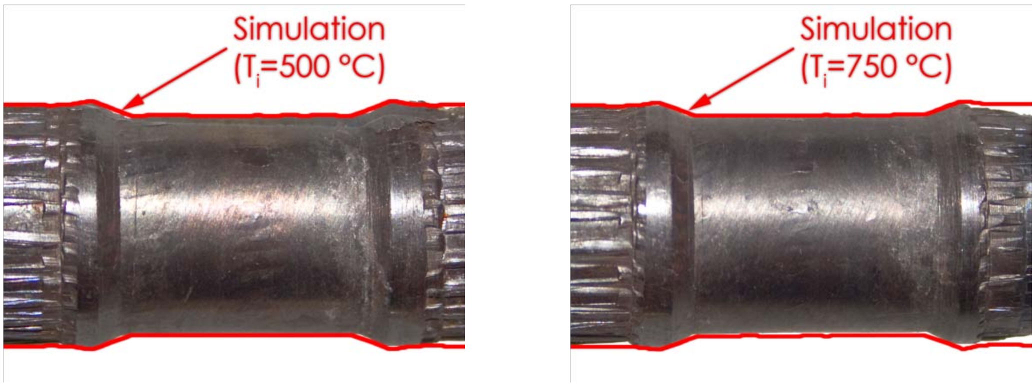

(a) (b)

Figure 5.9. The picture of cross-wedge rolled Ti6Al4V workpiece and the simulation deformed shaped of the same workpiece (red line shows simulation), workpiece initial temperatures (a) 500 °C and (b) 750 °C.

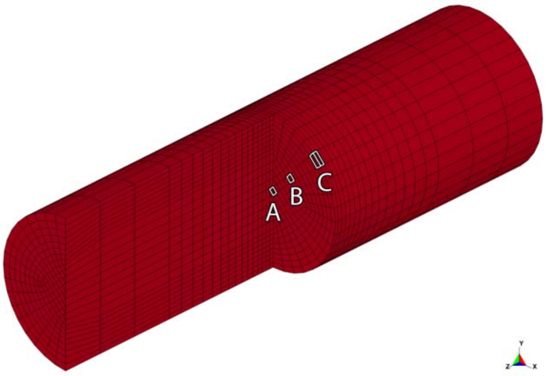

Figure 5.10. The selected elements at the center, middle and surface (A, B and C) of the workpiece.

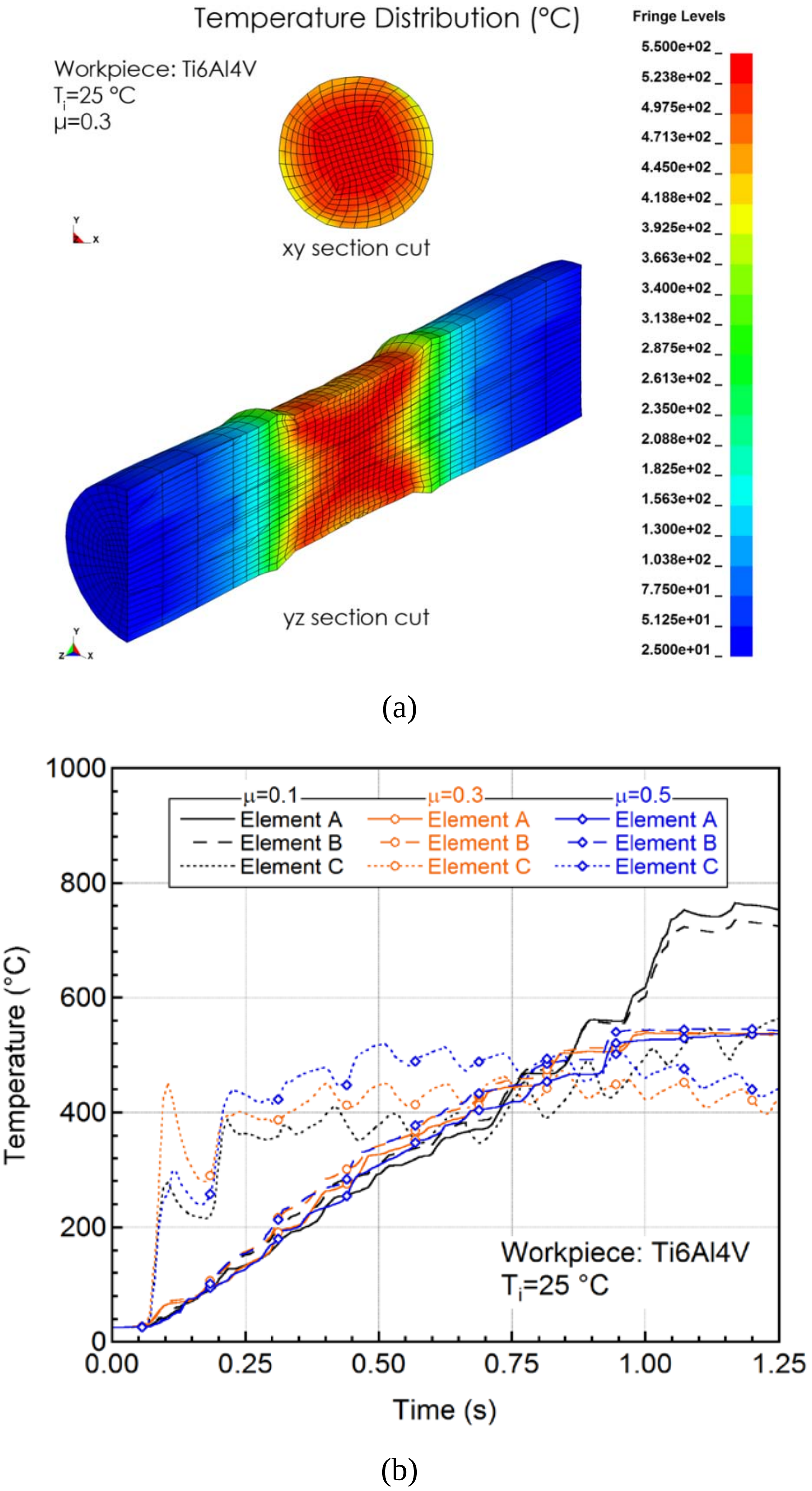

Figure 5.11. (a) The final temperature distribution of Ti6Al4V workpiece (the initial temperature of 25 °C) at the middle xy cross-section and along the yz cross-section, and (b) the temperature variations of element A, B and C with rolling time for different friction coefficients at the initial workpiece temperature of 25 °C.

The final temperature distribution of Ti6Al4V workpiece at the middle center (xy cross-section) and along the z-axis (yz cross-section), and the temperature of element A, B and C as function of rolling time at workpiece initial temperatures of 500 and 750 °C are shown in Figure 5.12(a) and (b), respectively. The static and dynamic friction coefficients were 0.5 in the simulations. The highest final temperature is seen in the stretching zone at the center of the workpiece. The workpiece final temperature at the center increases to roughly 900 and 1050 °C for the workpiece having initial temperatures of 500 and 750 °C. It is again found that although the surface temperature of the workpiece is higher at the initial region of the deformation, it quickly cools as the deformation progresses and becomes smaller than that of middle and centre point. The workpiece surface is cooled by thermal contact conductance when it is in contact with the tools (at constant temperature of 25 °C) and when the surface losses the contact to the tools, it is reheated by the conduction by the heat generated from the plastic deformation. The temperature profile of Ti6Al4V workpiece (T_i=500 °C) at different rolling times is shown in Figure 5.13. The temperature increase is high at the surface initially. In the later steps of the process, it is shifted to the workpiece center. The temperature of point A at 0.6 s is lower than at 0.68 s because the workpiece is in contact with the tools at 0.6 s. In Figure 5.14, the pictures of the deformed surfaces of Ti6Al4V workpiece cross wedge rolled at 25 and 500 °C initial temperatures are shown together with the tensile test specimens tested at 500 and 900 °C. The surface color of the sample cross wedge rolled at 25 °C is near blue, as with that of the sample tensile tested at 500 °C. Similarly the surface color of the sample cross wedge rolled at 500 °C is very much similar that of the tensile tested sample at 900 °C, light brown.

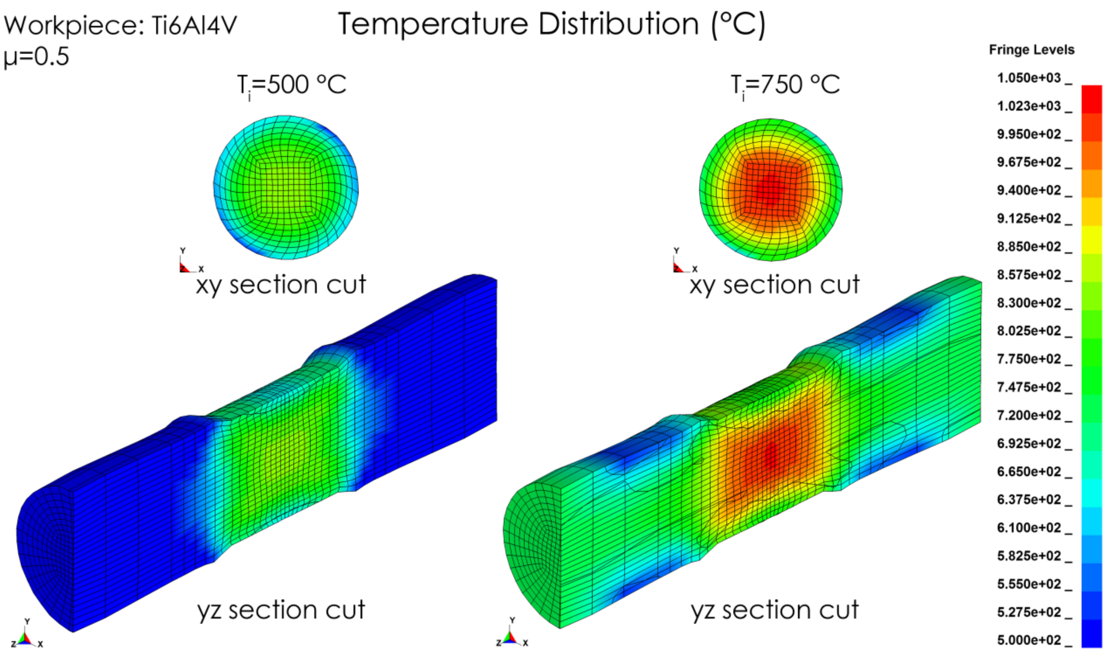

(a)

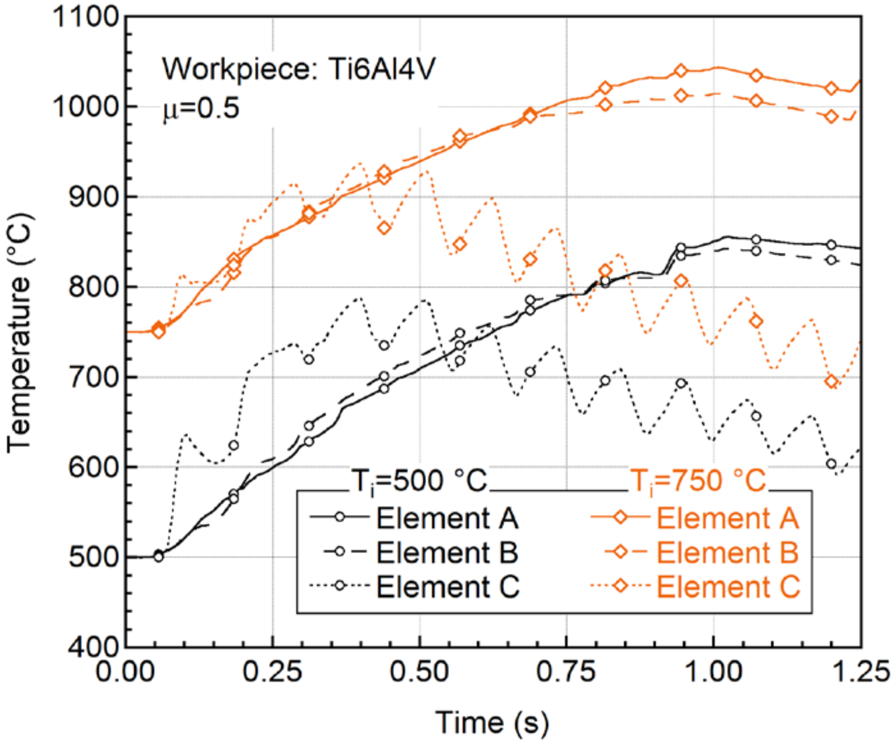

(b)

Figure 5.12. (a) The final temperature distribution of Ti6Al4V workpiece (the initial temperature of 500 and 750 °C) at the middle xy and yz cross-sections, and (b) the temperature variations of element A, B and C with rolling time at the initial workpiece temperature of 500 and 750 °C (the friction coefficients are 0.5).

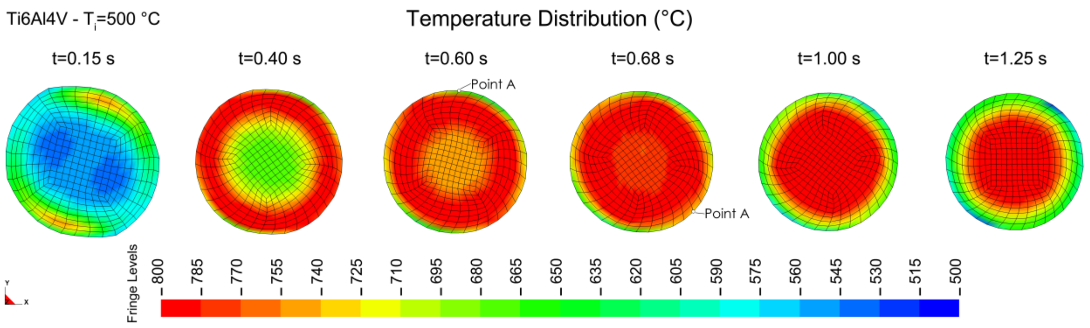

Figure 5.13. The temperature distribution of Ti6Al4V workpiece xy cross-sections at different rolling times.

Figure 5.14. The final temperature comparison of Ti6Al4V samples by surface color.

Figure 5.15 shows the variation of experimental and simulation tangential forces of 1045 steel workpiece initial temperatures of 750 and 1050 °C, rolled by Tool-1 at tool temperature of 25 °C. The static and dynamic friction coefficients were 0.5 for both simulations. The material models AISI 1045 JC-2 and JC-1 were used in the simulations of workpiece at initial temperatures of 750 and 1050 °C, respectively. As is seen in Figure 5.15, the simulation and experimental tangential forces show well agreements for 750 °C, while simulation tangential forces are slightly higher than those of experiments for 1050 °C are.

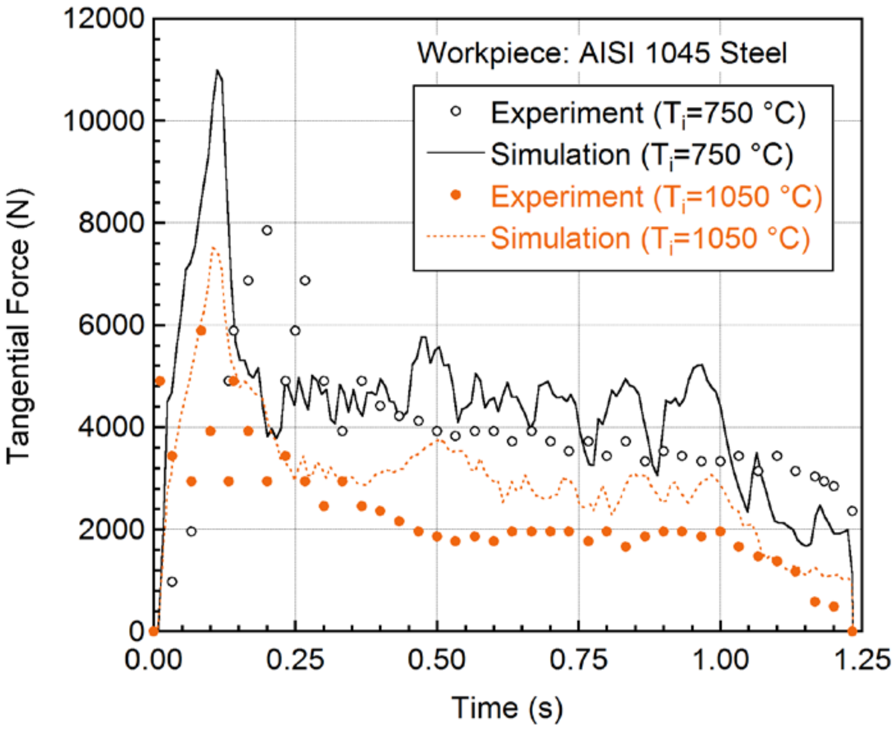

Figure 5.15. The variation of experimental and simulation tangential forces of 1045 steel workpiece initial temperatures of 750 (JC-2 material model) and 1050 °C (JC-1 material model) rolled by tool-1 at tool temperature of 25 °C (μ=0.5).

5.2. Parametric Study

The parameters investigated in the parametric study of CWR of 1045 steel are listed in Table 5.1. The forming angle varies between 30 and 40°, while stretching angle between 7 and 10°. The area reduction varies between 31.75 and 51.60%, and the friction coefficient (static and dynamic) between 0.3 and 0.8. The number of elements used in the modeling of the tools in the parametric study is further tabulated in Table 5.2. The effect of parameters on the deformation behavior of the workpiece are determined at mid cross-section, for the central, middle and surface nodes, represented as A, B and C in Figure 5.16. The parametric study was performed at 1000 °C using JC-2 model for 1045 steel.

Table 5.1. The parameters investigated in the parametric study of 1045 steel.

Parameters	**Values**
Forming angle, α (°)	30-35-40
Stretching angle, β (°)	7-8-10
Area reduction, Δ_A (%)	31.75-38.75-45.36-51.60
Friction coefficient, μ	0.3-0.5-0.8

Table 5.2. The number of shell elements used in the tool design (Tool-2) for Δ_A=45%.

Parameter:	β	7°			8°			10°		
	α	30°	35°	40°	30°	35°	40°	30°	35°	40°
Number of elements		7048	7208	7208	7142	6936	6940	6772	6802	7178

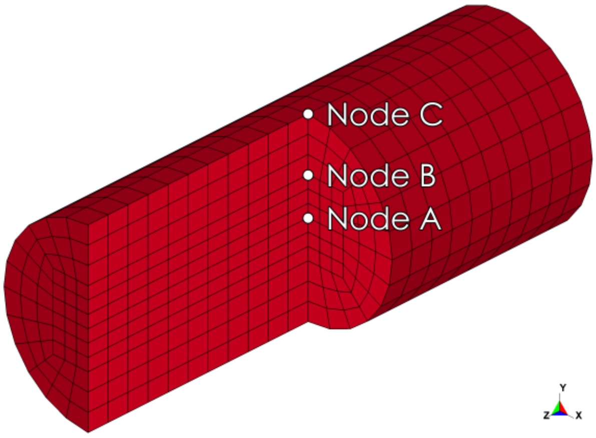

Figure 5.16. The locations of investigated nodes at mid cross-section of the workpiece: A-center, B-middle and C-surface nodes.

5.2.1. Effect of Reduction Ratio

Figure 5.17 shows the numerically deformed final shape of 1045 workpiece. The initial diameter of the workpiece is 24 mm. In the model, both top and bottom tools move to each other with a velocity of 0.86 m s^{-1}, corresponding a relative velocity of 1.72 m s^{-1}. The tool velocity selected is comparable with the tool velocities used in conventional CWR practice, which range between 1-2 m s^{-1}. The tools compress the workpiece at the top and bottom with at distance of 0.5 mm, corresponding to a total vertical workpiece displacement of 1 mm. Therefore, the initial diameter of the workpiece is reduced to 23 mm by the pressure applied by the tools. As stated earlier, the compression of the workpiece in the model functions as indents and also as serrations. Figure 5.18 shows the final geometries of the workpiece as function of the area reductions. As noted in this figure, as the area reduction increases, the final length of the workpiece increases. The final length of the workpiece is therefore dictated by the applied are reduction.

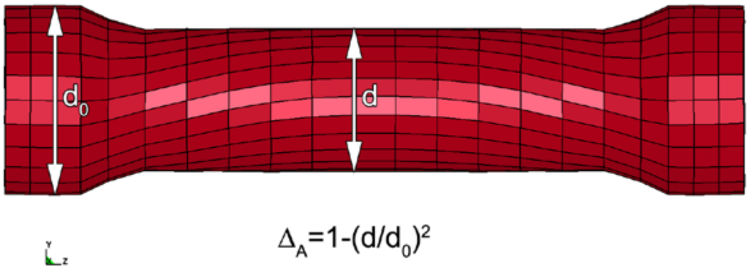

Figure 5.17. The final deformed shape and dimensions of the workpiece.

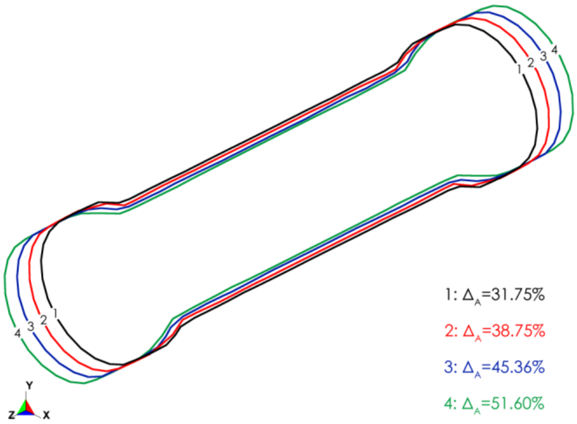

Figure 5.18. The workpiece final geometry at varying area reductions.

The effect of area reduction at constant forming and stretching angle on the tangential and vertical forces during CWR is shown in Figure 5.19. Both forces increase in the knifing zone as the tool start to deform the workpiece initially. After forming a notch on the workpiece in the knifing zone, both forces decrease gradually in the guiding zone, as seen in Figure 5.19. The forces increase in the stretching zone until about sizing zone. Thereafter, the forces decrease gradually. The effect of increasing area reduction is to increase the tangential force and to decrease the thrust force. It is further noted that the effect of area reduction on the forces is more pronounced in the stretching zone.

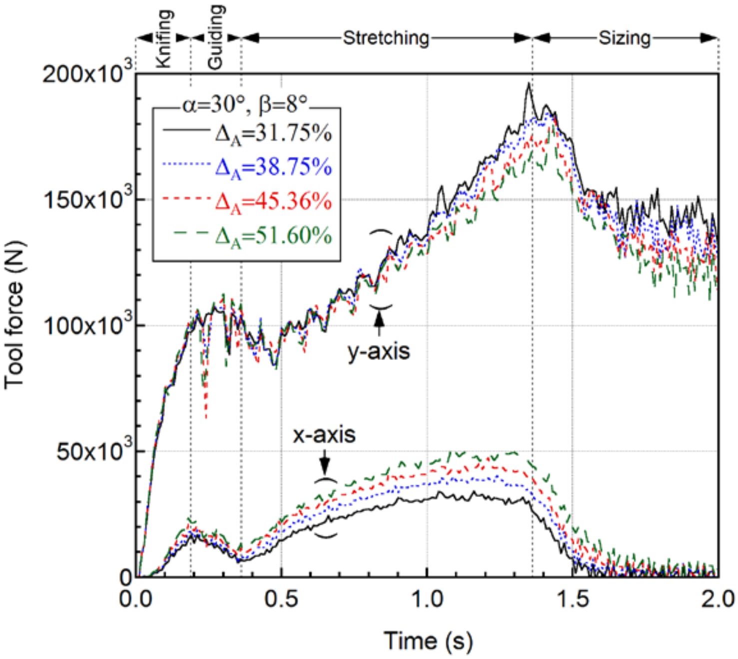

Figure 5.19. The tool forces vs. time at different area reductions.

The effect of reduction area on the final temperature distribution of the workpiece (α=30° and β=8°) is shown for two different cross-sections of the workpiece, yz and xy, in Figure 5.20. Increasing area reduction increases the temperature at the mid sections of the workpiece. The highest temperature increase is at center of the workpiece and the lowest at the surface of the workpiece, through the ends of the workpiece. The variation of the workpiece temperature at the center, middle and surface nodes with CWR time is shown in Figure 5.21. Depending on the value of the area reduction, the surface point temperature decreases gradually with time from the initial workpiece temperature, 1000 °C, to 800-900 °C at the end of the CWR. The oscillations seen in the surface temperature distributions are resulted from the workpiece surface contact and noncontact with the tools. The temperature at the center and middle node/point increases with increasing deformation time in the stretching zone, reaching maxima, and gradually decreases in the sizing zone. The increase in the workpiece temperature at the center and middle point is due to the conversion of the work into heat (adiabatic heating) and the subsequent cooling due to the heat losses through conduction and convection.

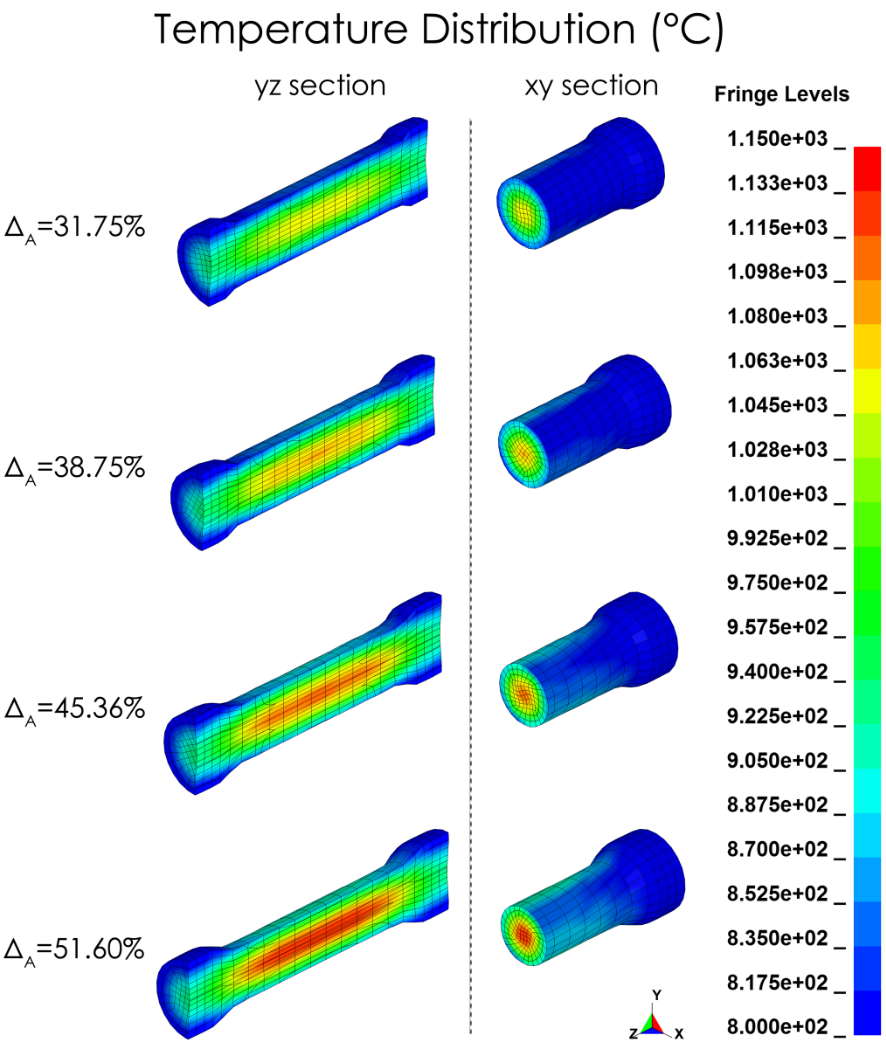

Figure 5.20. The final temperature distribution of the workpiece in the cross sections of xy and yz for different area reductions (α=30° and β=8°).

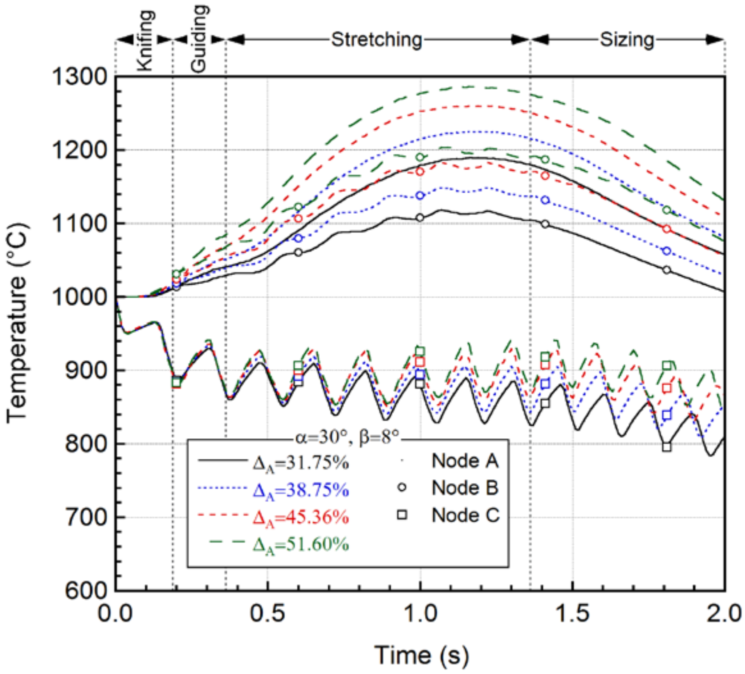

Figure 5.21. The temperature variations of node A, B and C for different area reductions (α=30° and β=8°).

The effective strain distribution of the workpiece is shown for two different area reductions, 31.75% and 51.60%, and for xy and yz cross-section of the workpiece in Figure 5.22(a) and (b), respectively. The highest effective strain values are found in the stretched region of workpiece as shown these figures. The variation of the effective strain at the center, middle and surface node with CWR time is further shown in Figure 5.23. As seen the graphs in Figure 5.23, the effective strain increases sharply in the knifing zone, increases gradually in the guiding zone and stretching zone and almost remains constant in the sizing zone. Despite the variations in the effective strains between the center, middle and surface points, the differences level out at the later stages of the deformation at the end of the stretching zone.

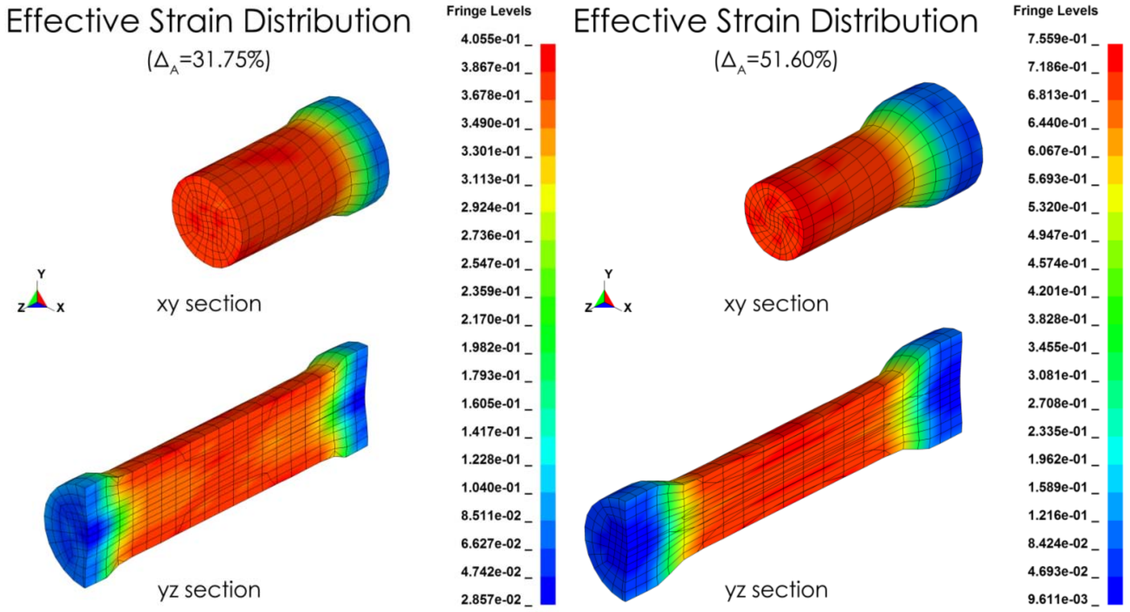

(a) (b)

Figure 5.22. The effective strain distribution of the workpiece cross sections of xy and yz for (a) Δ_A=31.75% and (b) Δ_A=51.60% (α=30° and β=8°).

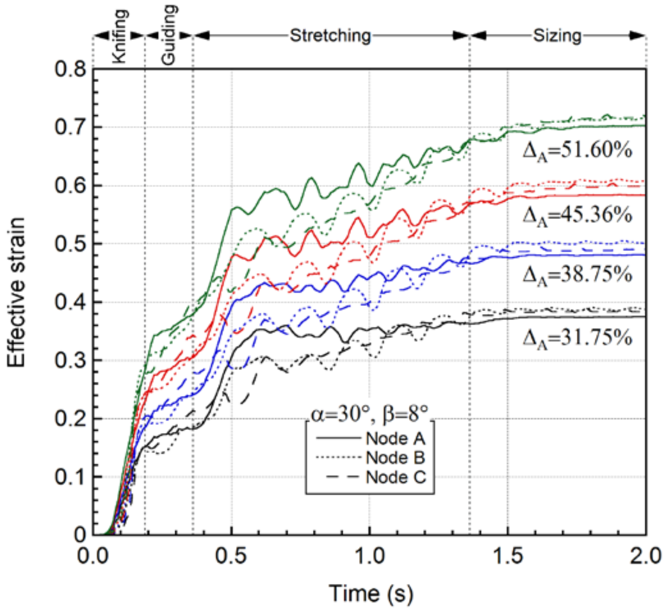

Figure 5.23. The effective strain distribution of A, B and C node for different area reductions (α=30° and β=8°).

The effective stress distribution of the workpiece for yz cross-section at various CWR times corresponding to knifing; guiding, stretching and sizing zone for Δ_A=31.75% is shown in Figure 5.24. The highest effective stress is seen at the surface of the workpiece, in the shoulder region. Figure 5.25(a) and (b) show the effective stress variations of A, B and C node with the CWR time for the area reduction of 31.75% and

51.60%, respectively. The effective stress increases almost linearly with deformation time in the knifing zone and remains almost constant throughout the stretching zone for lower area reduction and slightly reduced in the stretching zone for higher area reduction, except for the surface node, C. At the surface, because of contact and non-contact of the tolls with the workpiece, the effective stress shows oscillations for both are reductions as shown in Figure 5.25(a) and (b). In addition, it also noted that the highest effective stresses are found on the surface and the lowest in the center point. Figure 5.26(a), (b) and (c) show sequentially, the variation of the effective stress for the center, middle and surface point with the area reduction. Increasing area reduction reduces the center, middle and surface point effective stress in the stretching zone as seen in Figure 5.26(a), (b) and (c). In the sizing zone, the effective stresses for 3 points level out, reaching to the same level. The effect of increasing area reduction is to increase the effective stress in the knifing and guiding zone, and to reduce the range of stress oscillations on the surface.

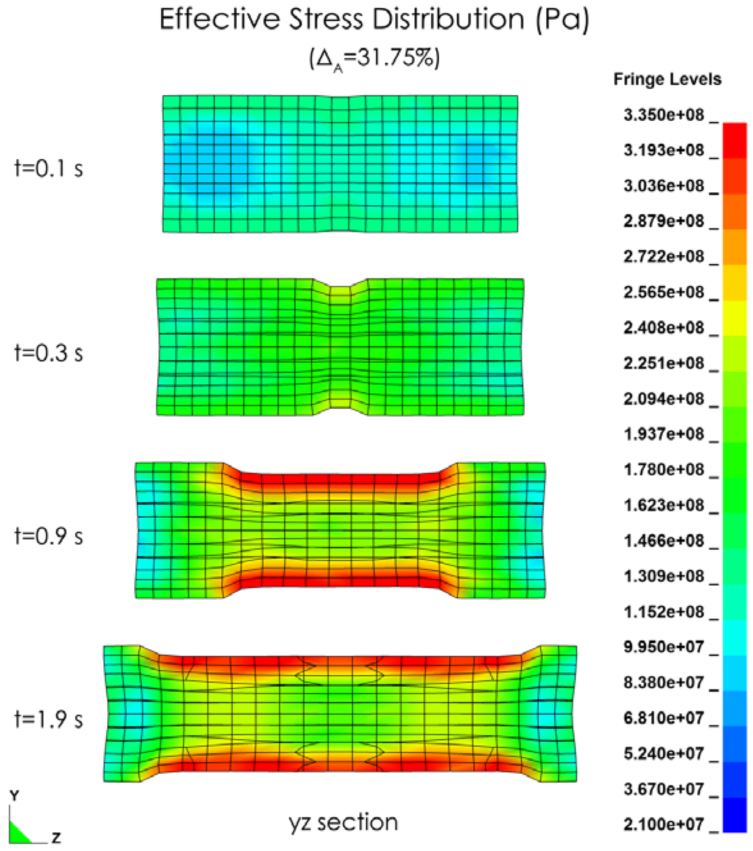

Figure 5.24. The effective stress distribution of the workpiece yz cross section at different rolling times (t=0.1, 0.3, 0.9, 1.9 s) for Δ_A=31.75% (α=30° and β=8°).

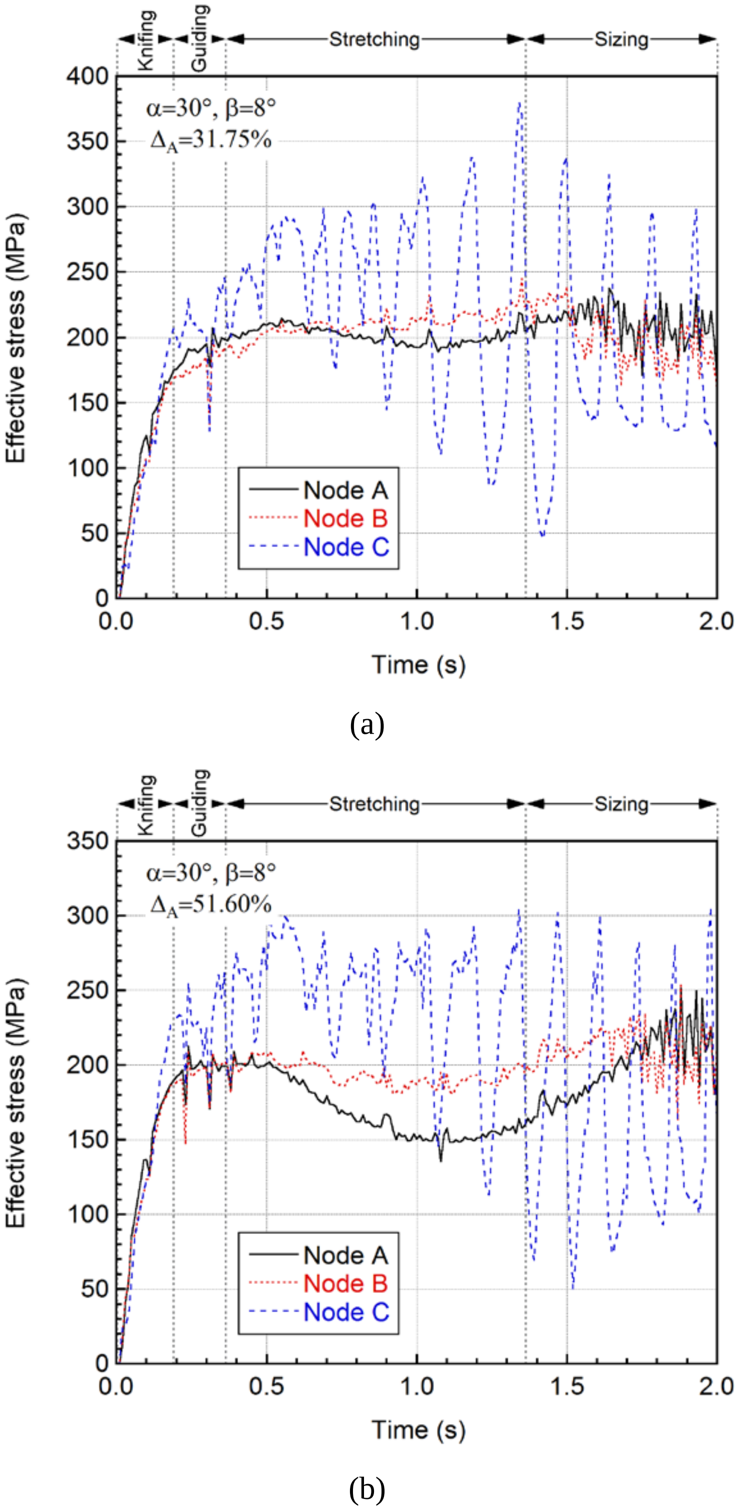

Figure 5.25. The effective stress variation of A, B and C node with time for (a) Δ_A=31.75% and (b) Δ_A=51.60% (α=30° and β=8°).

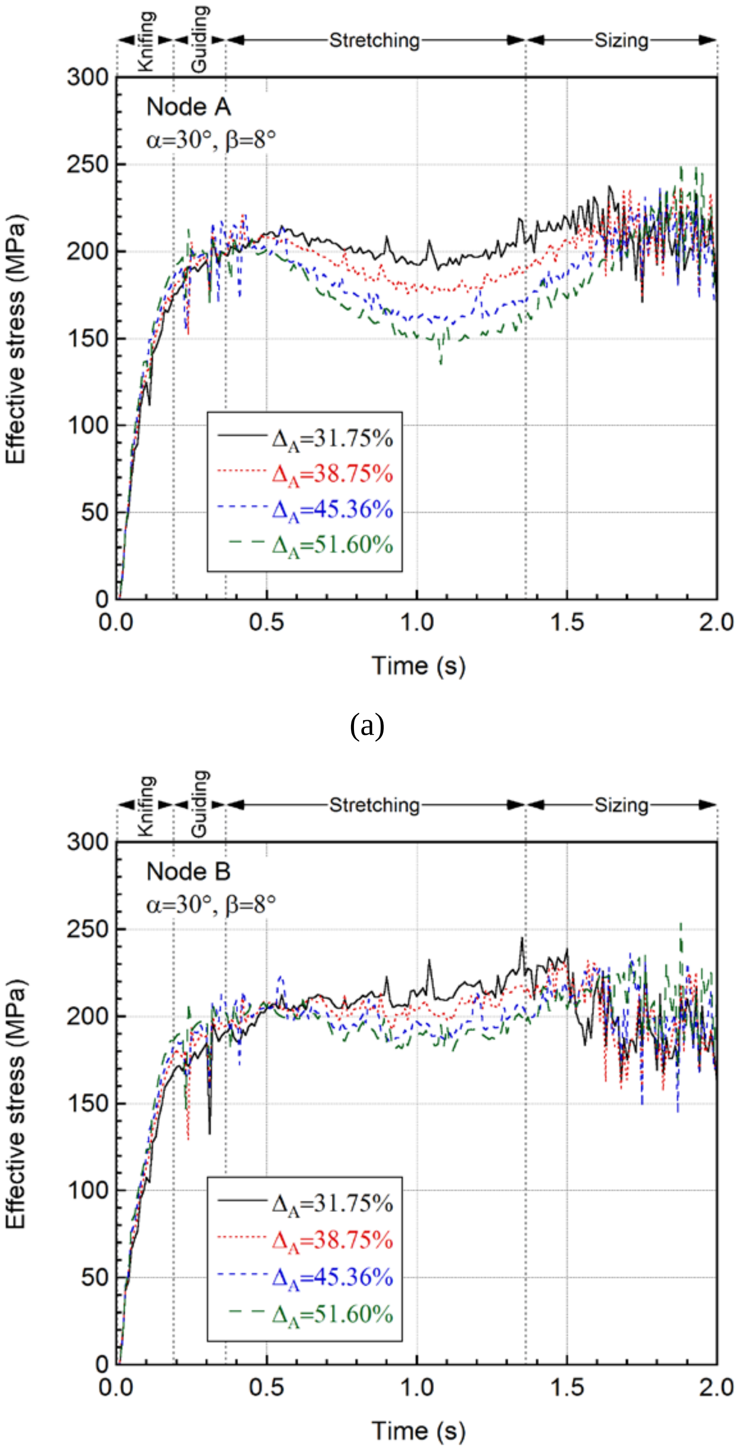

(a)

(b)

Figure 5.26. The effective stress variations with time: (a) node A, (b) node B and (c) node C (=30° and β=8°).

(cont. on next page)

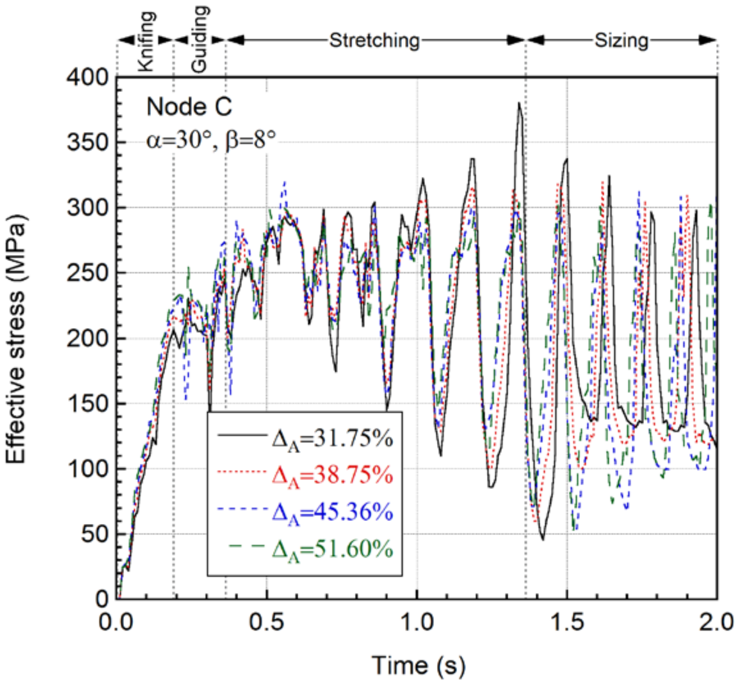

(c)

Figure 5.26. (cont.)

The maximum principal stress distribution of the workpiece cross sections of yz at different rolling times (t=0.1, 0.3, 0.9, 1.9 s) corresponding to knifing; guiding, stretching and sizing zone is shown in Figure 5.27 for an area reduction of 31.75% (tool parameters: α=30° and β=8°). The highest maximum principal stresses are seen in Figure 5.27 to occur in the mid sections of the workpiece, while the lowest at the surface near the shoulder. Figure 5.28(a) and (b) show the principal stress variations with time at A, B and C node for the area reduction of 31.75% and 51.60%, respectively. For both area reductions, the highest maximum principal stress occurs at the center of the workpiece in knifing zone and sizing zone. Again, the maximum principal stress at the surface shows oscillations resulting from tool contact and noncontact. Increasing area reduction reduces the center and middle point maximum principal stress in knifing, guiding and stretching zone as shown in Figure 5.29(a) and (b), while increases the maximum principal stress at the surface (Figure 5.29(c)).

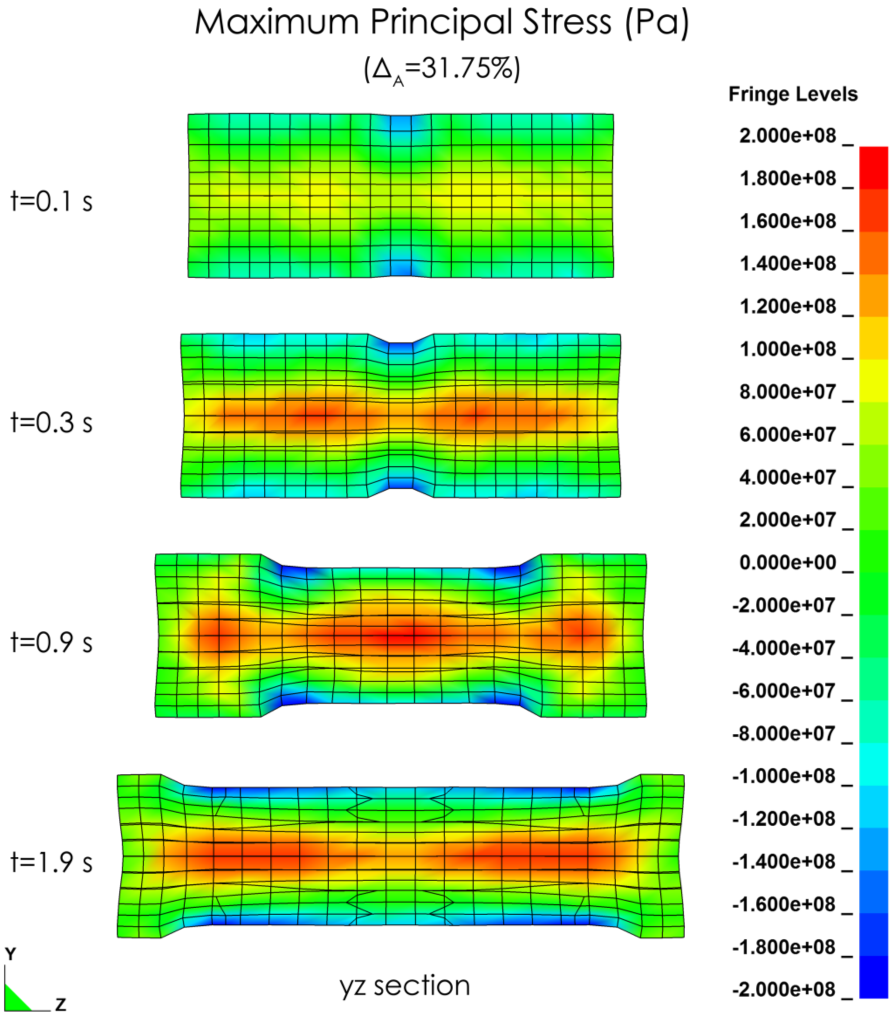

Figure 5.27. The maximum principal stress distribution of the workpiece cross section yz at different rolling times (t=0.1, 0.3, 0.9, 1.9 s) for Δ_A=31.75% (α=30° and β=8°).

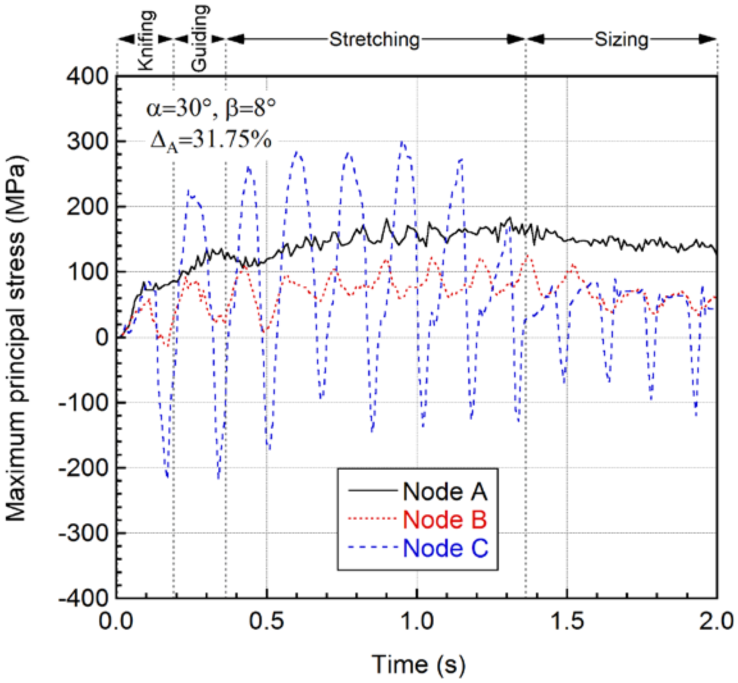

(a)

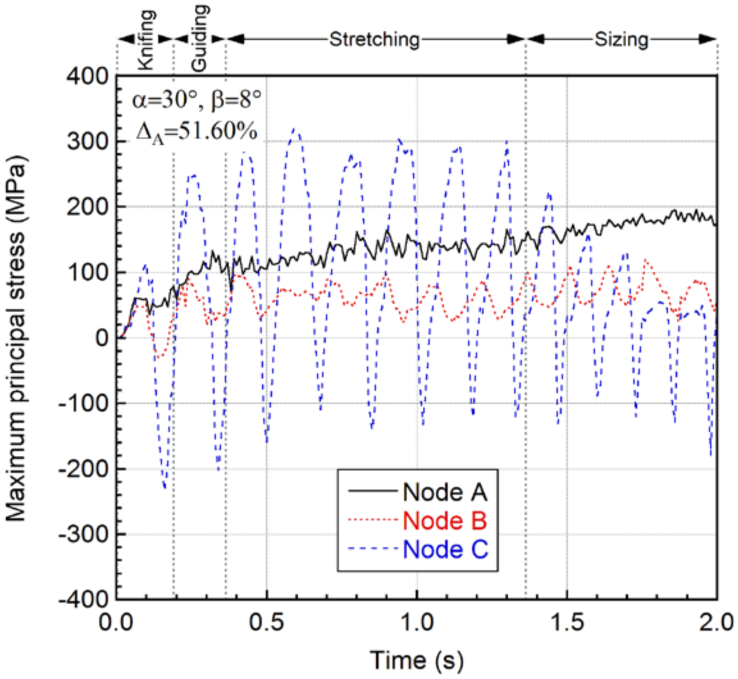

(b)

Figure 5.28. The maximum principal stress variation of A, B and C node with time for (a) Δ_A=31.75% and (b) Δ_A=51.60% (α=30° and β=8°).

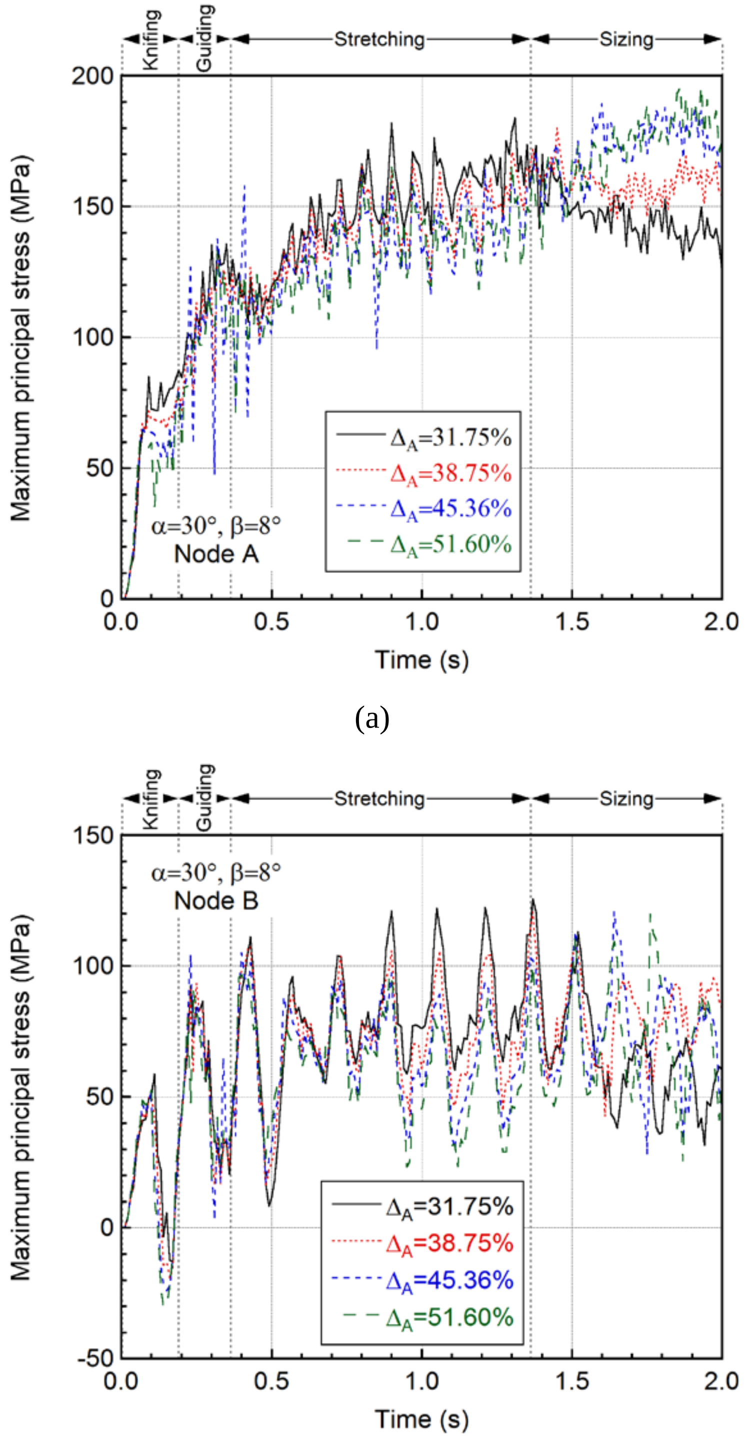

(a)

(b)

Figure 5.29. The maximum principal stress variation with time: (a) node A, (b) node B and (c) node C (=30° and β=8°).

(cont. on next page)

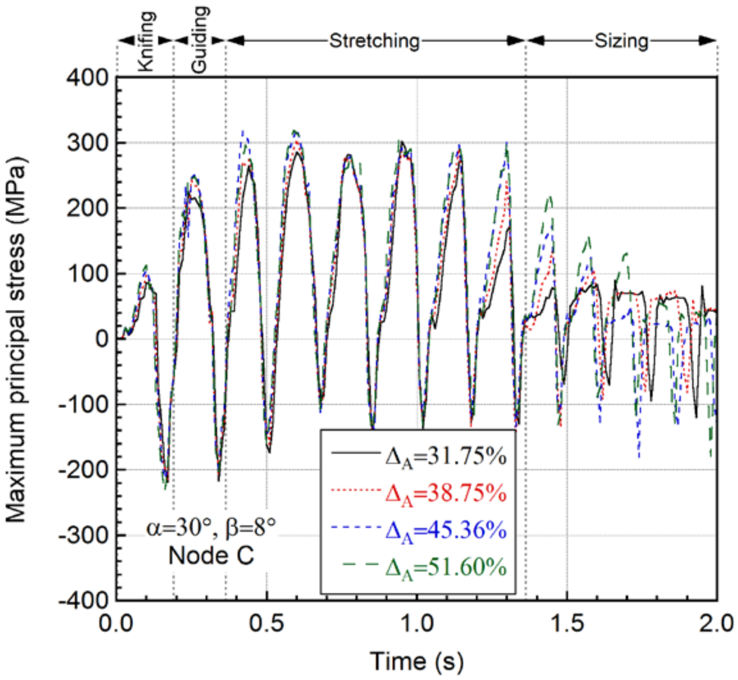

(c)

Figure 5.29. (cont.)

The stress triaxiality distribution of the workpiece cross sections of yz at different rolling times (t=0.1, 0.3, 0.9 and 1.9 s) corresponding to knifing; guiding, stretching and sizing zone is shown in Figure 5.30. The stress triaxiality is the highest on the both sides of the shoulder of the workpiece in knifing and guiding zone, while the stress triaxiality becomes the highest at the mid sections in the stretching zone. Figure 5.31(a) and (b) show the stress triaxiality variation of node A, B and C with time for the area reduction of 31.75% and 51.60%, respectively. The stress triaxiality at node B is only positive in the knifing zone; thereafter, becomes negative in the subsequent zones for both area reductions. The stress triaxiality at the surface shows oscillations between negative and positive value, which is again resulting from tool contact and noncontact. At the center point, positive stress triaxiality is found throughout the deformation starting from the stretching zone. In the knifing and guiding zone, the highest positive stress triaxiality is found at the surface of the workpiece, and in the stretching zone the stress triaxiality of the center point increases to the level of the surface positive stress triaxiality. Increasing area reduction from 37.5 to 51.60% decreases the stress triaxiality at the center point in knifing and guiding zone, while it increases stress triaxiality stretching and sizing zone (Figure 5.32(a)). Increasing area reduction also increases the stress triaxiality in the negative direction in the middle point

(Figure 5.32(b)) and in the positive and negative direction at the surface (Figure 5.32(c)).

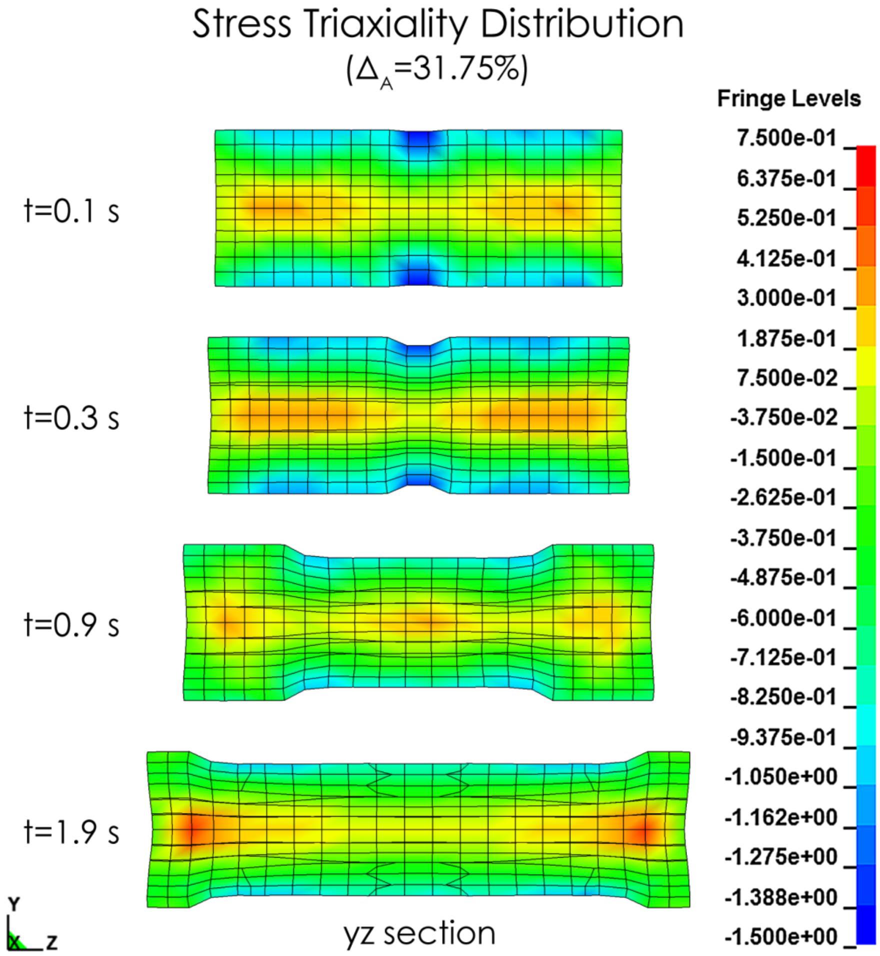

Figure 5.30. The stress triaxiality distribution of the workpiece cross section yz at different rolling times (t=0.1, 0.3, 0.9, 1.9 s) for Δ_A=31.75% (α=30° and β=8°).

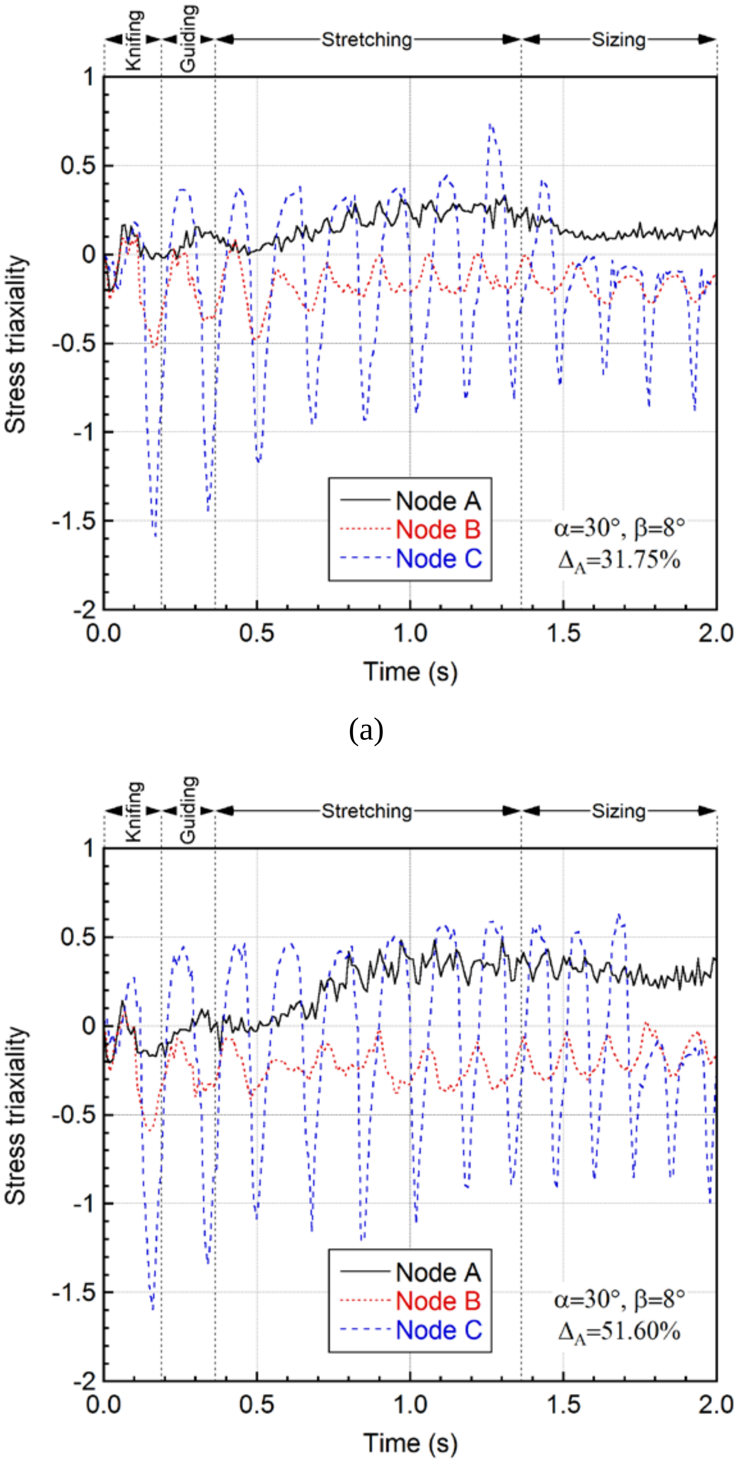

(a)

(b)

Figure 5.31. The stress triaxiality variation of A, B and C node with time for (a) Δ_A=31.75% and (b) Δ_A=51.60% (α=30° and β=8°).

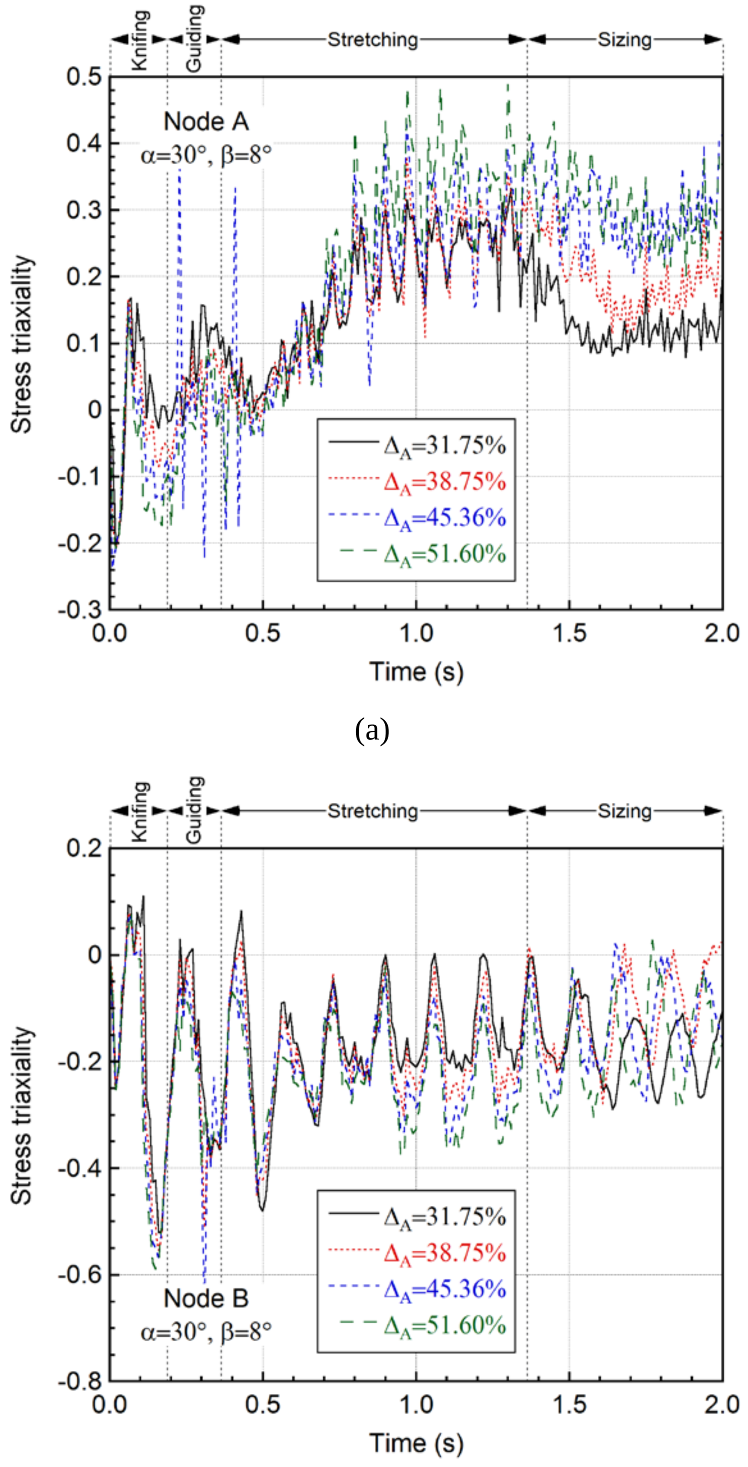

(a)

(b)

Figure 5.32. The stress triaxiality variation by time: (a) node A, (b) node B and (c) node C (=30° and β=8°).

(cont. on next page)

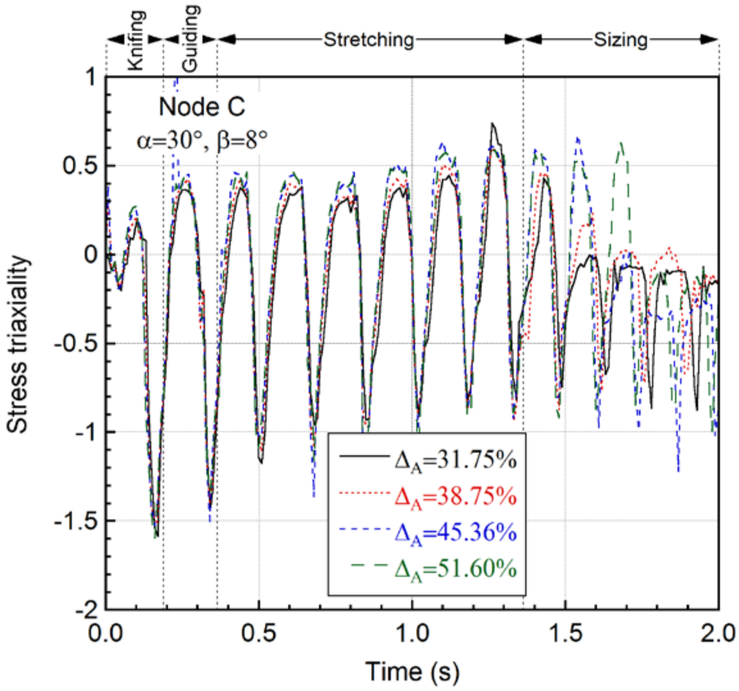

(c)

Figure 5.32. (cont.)

Figure 5.33(a) and (b) show the effective strain rate variation of node A, B and C node with time for the area reduction of 31.75% and 51.60%, respectively. As is seen in these figures, the strain rate sharply increases in the knifing zone and shows oscillations throughout the deformation time for the selected three nodes. It is also note that increasing are reduction increases strain rate in the knifing zone and increases the oscillations.

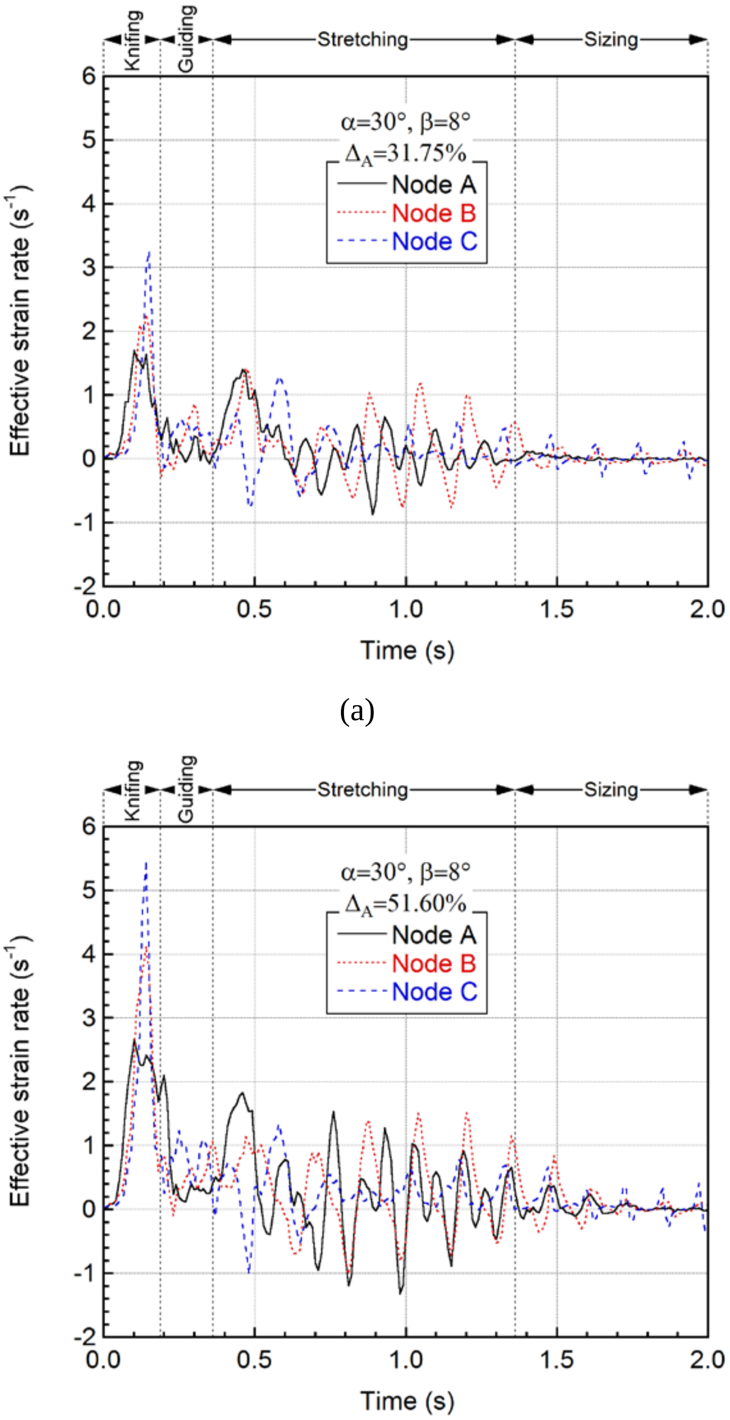

(a)

(b)

Figure 5.33. The effective strain rate variation of A, B and C node with time for (a) Δ_A=31.75% and (b) Δ_A=51.60% (α=30° and β=8°).

5.2.2. Effect of α and β

The effect of α on tool forces is shown in Figure 5.34(a) for β=8° and Δ_A=45.36%. As seen in this figure, the thrust force (y-axis) does not change significantly for different α values. The tangential forces (x-axis) increase at the end of the stretching zone when the α decreases from 40° to 30°. The maximum tangential force occurs for α=30°. In Figure 5.34(b), the effect of β on tool forces is shown for α=30° and Δ_A=45.36%. The stretching angle is seen to affect the thrust and tangential forces. At the beginning of stretching zone, the thrust force decreases with decreasing β. In later stages of the process, the thrust force value of lower β surpasses the one of higher β. This is because the force profile is growing linearly and the stretching zone for lower β values is much longer than the one of higher β values. As the stretching zone length increases, the thrust force increases. The maximum thrust force values are seen at the end of stretching zone for each simulation modeled for the parametric study. A similar effect of β on tangential force is found on the thrust force, except the tangential force values decreases with decreasing β values throughout the stretching zone. The maximum tangential force values are seen for higher β values as the force profiles exponentially decrease and the length of stretching zone is shorter at higher β values. In sizing zone, both forces are found to be same and constant for all designs. This behavior is expected and it shows that the workpiece actually takes its final shape, which is identical for all designs having the same area reductions.

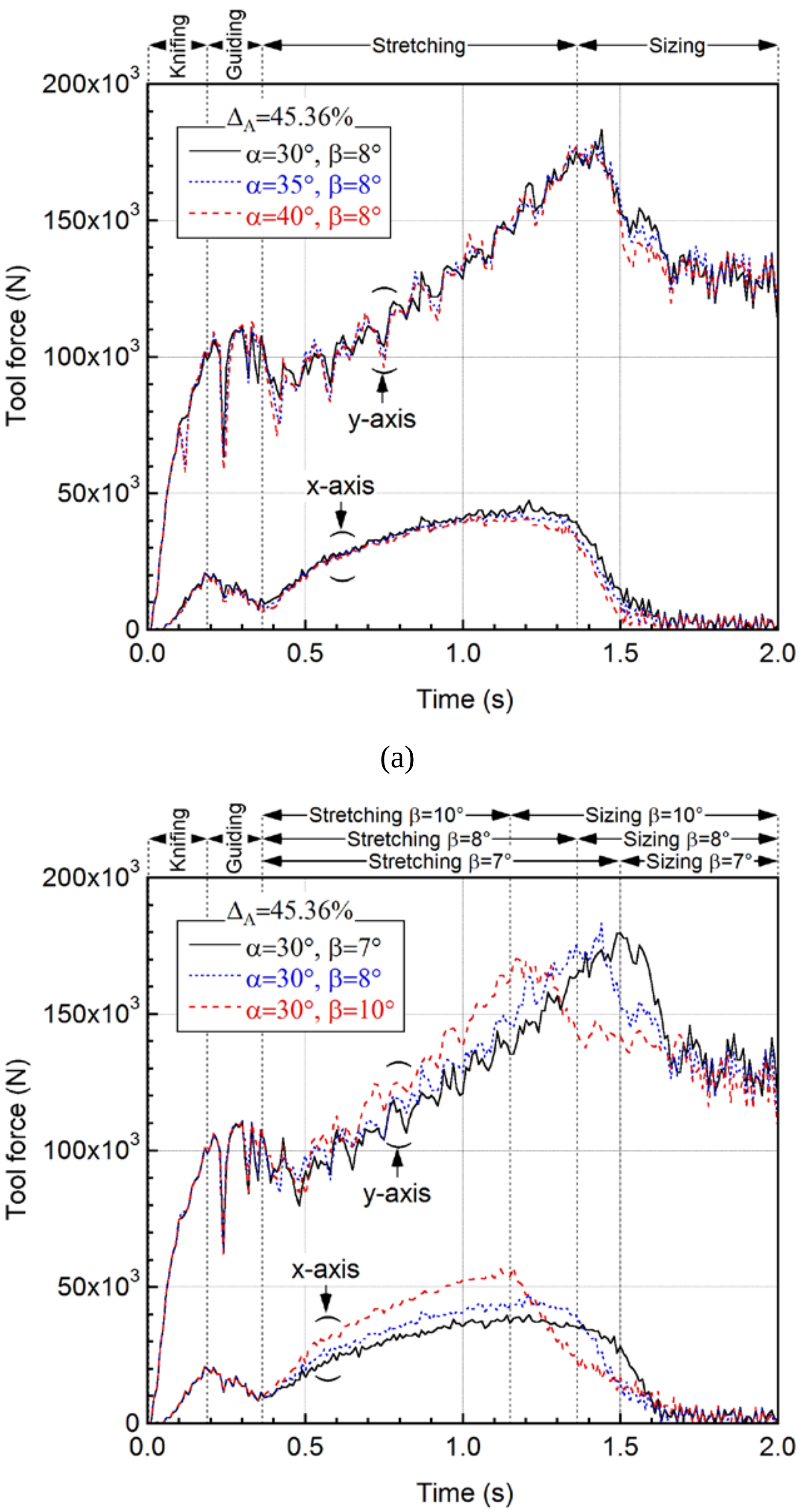

(a)

(b)

Figure 5.34. The variation of tool forces with CWR time for different (a) α and (b) β values.

Figure 5.35 shows the final temperature distribution of yz and xy cross-sections at increasing α values for Δ_A=45.36% and β=8°. The highest temperature is attained in the workpiece mid section, at the center of the workpiece in each design. The forming angle is found to slightly affect the final temperature distribution of the workpiece: increasing the α values result in lower temperature attainment in the workpiece. Figure 5.36 shows the final temperature distribution of yz and xy cross-sections at increasing β values for Δ_A=45.36% and α=30°. The highest temperature is attained again in the mid section, at the center of the workpiece. Increasing β values, in contrast to α, results in higher temperature attainment in the workpiece. The final temperature at the center of the workpiece reaches 1200 °C.

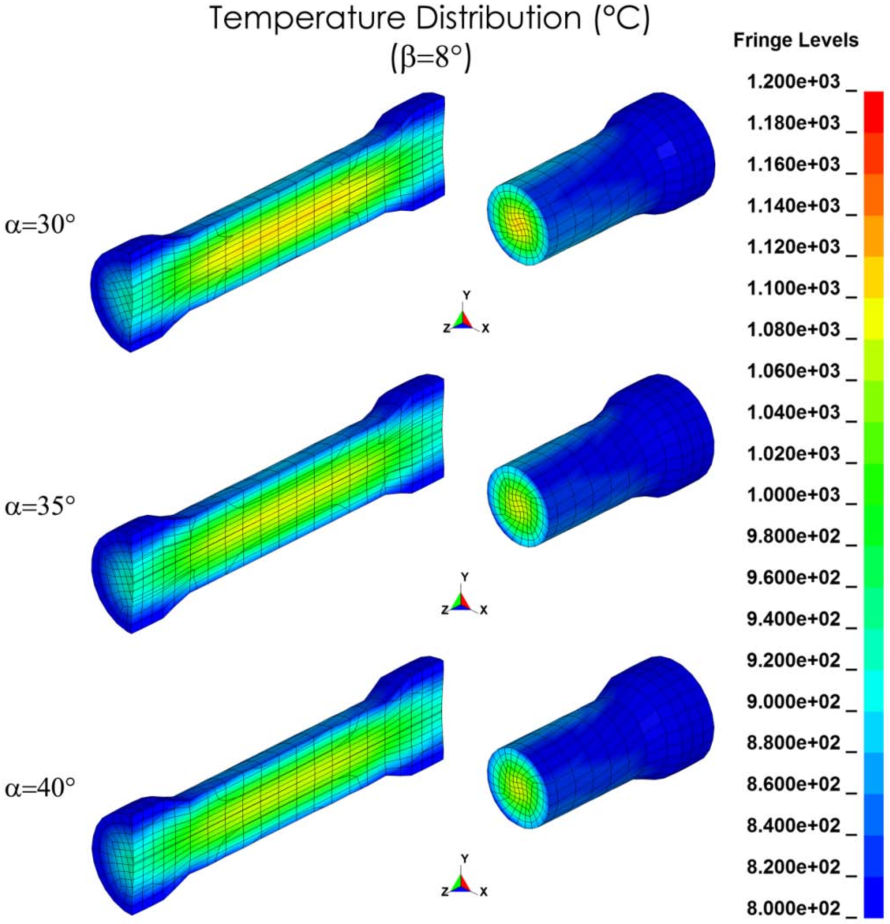

Figure 5.35. The final temperature distribution of the workpiece in the cross sections of xy and yz for different α values (Δ_A=45.36% and β=8°).

Figure 5.36 shows the final temperature distribution of yz and xy cross-sections for Δ_A=45.36% and α=30° at different β values. The highest temperature is attained at the mid section as is expected. The temperature distribution at different β values is almost the same except that the magnitudes of temperature are different. Increasing β results in higher temperatures without changing the temperature distribution profile.

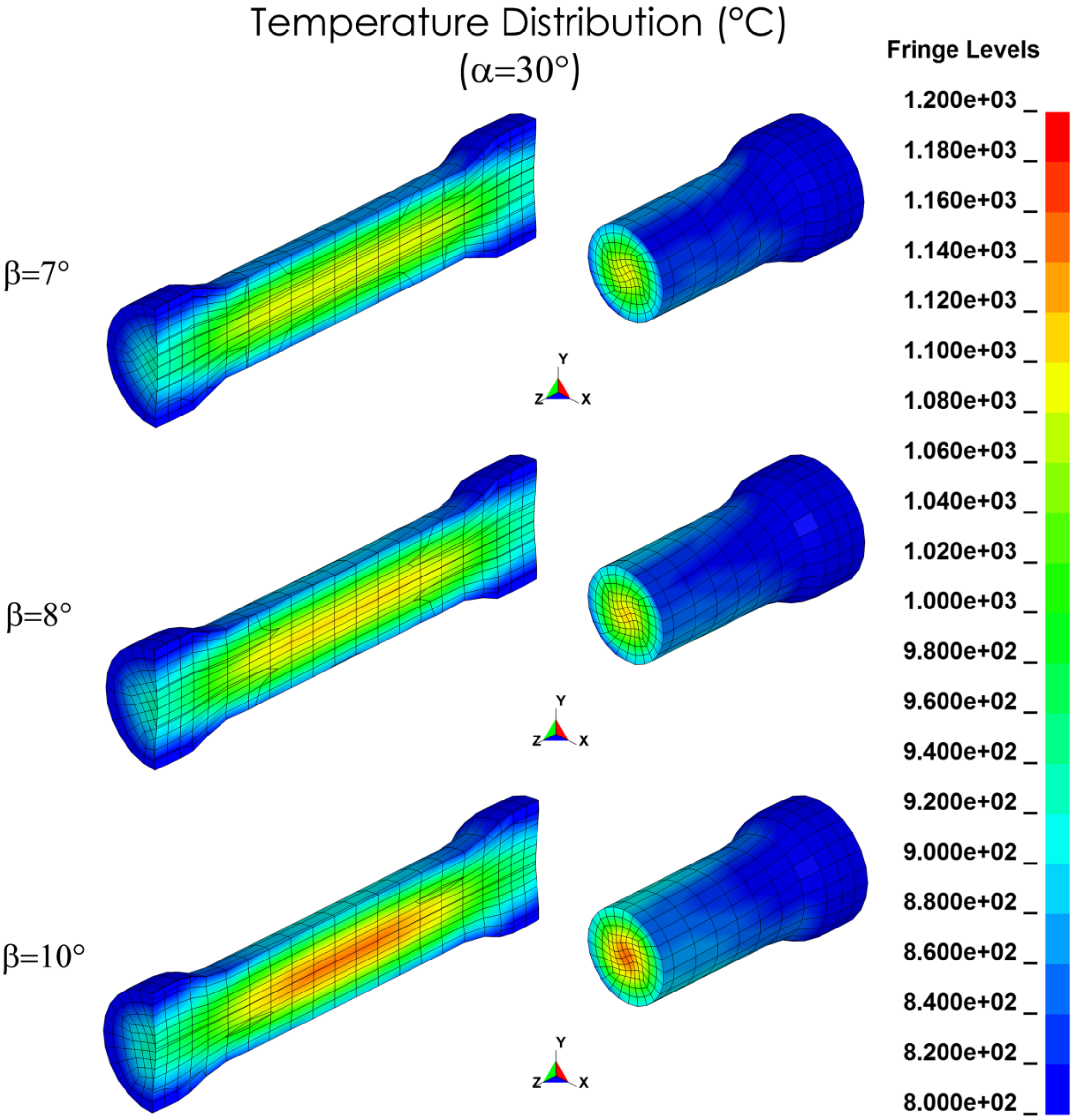

Figure 5.36. The final temperature distribution of the workpiece in the cross sections of xy and yz for different β values (Δ_A=45.36% and α=30°).

The temperature variations of the center, middle and surface point with deformation time for different α and β values are sequentially shown in Figure 5.37. The temperature of the selected locations decreases, starting from the end of the knifing zone through the end of the sizing zone, as the α increases because of reduction in the contact area with increasing α values (Figure 5.37(a)). For nodes A and B, this variation is found to initiate in the guiding zone and continues until the end of the process. The temperature change on the surface (node C) starts in the middle of the stretching zone and continuous until the end of process. The temperature difference between two analyses; α= 30° and 40° is 36.3, 30 and 55.7 °C for node A, B and C, respectively. This shows that the α is more effective on the surface temperature than in the middle and center temperature. The second most affected point is the center of the workpiece. In Figure 5.37(b), it is noted that β has great influence on the temperature. The temperature increases with increasing β. The variation of temperature starts at the beginning of stretching zone and continues until the end of process. The temperature difference between the two analyses: β=7° and 10° is 59, 50 and 33.7 °C for node A, B and C, respectively. This proves that β is more effective in increasing temperature of the workpiece at the center (node A).

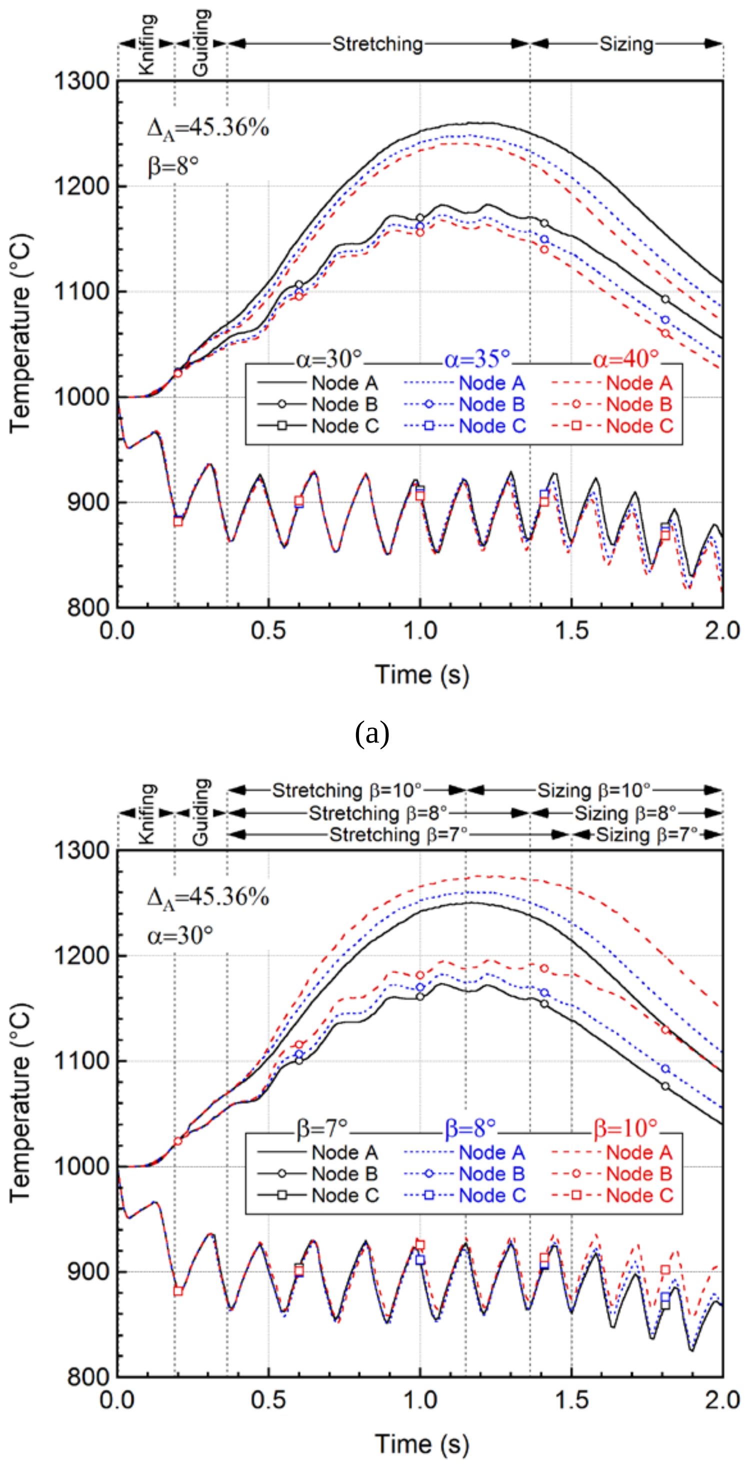

(a)

(b)

Figure 5.37. The temperature variation of center, middle and surface node with deformation time for different (a) α and (b) β values (Δ_A=45.36%).

The effective strain distribution on the yz cross-section of the workpiece as a function of time (t=0.1, 0.3, 0.9 and 1.9 s) corresponding to knifing, guiding, stretching and sizing zone is shown in Figure 5.38 for α=30°, β=8°, and Δ_A=45.36%. As is seen in Figure 5.38, the strain is localized in the middle of workpiece along the z-axis and the highest effective strain attained is nearly 0.6 at the end of CWR process. The variations of the effective strain of the center, middle and surface point at different α values (β=8°, and Δ_A=45.36%) and β values (α=30° and Δ_A=45.36%) are shown sequentially in Figure 5.39(a-c) and Figure 5.40(a-c). The forming angle and stretching angle within the studied ranges of the parameters slightly affect the effective strain variations at the center, middle and surface points. Increasing the stretching angle results in a decrease of the effective strain because the length of stretching zone is shorter for higher β values.

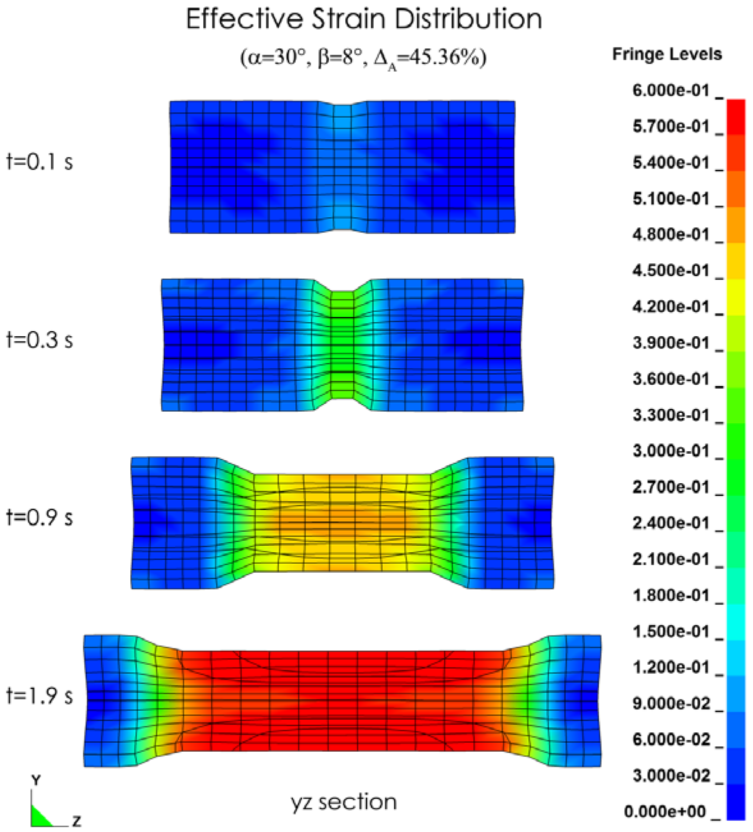

Figure 5.38. The effective strain distribution of the workpiece cross section yz at different rolling times (t=0.1, 0.3, 0.9, 1.9 s) for Δ_A=45.36%, α=30° and β=8°.

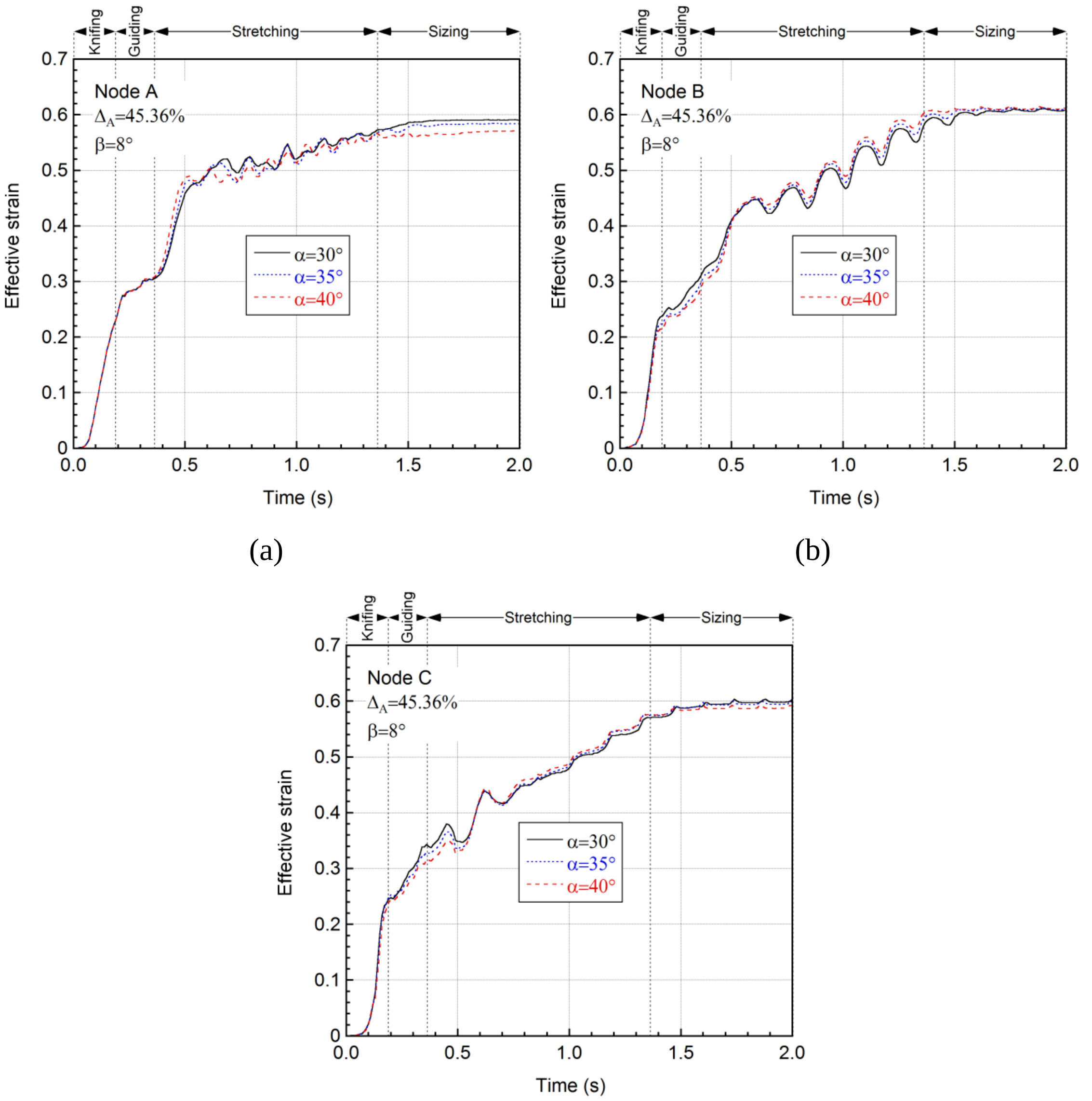

(a)

(b)

(c)

Figure 5.39. The effective strain variations of (a) node A, (b) node B and (c) node C with time at different α values (for Δ_A=45.36% and β=8°).

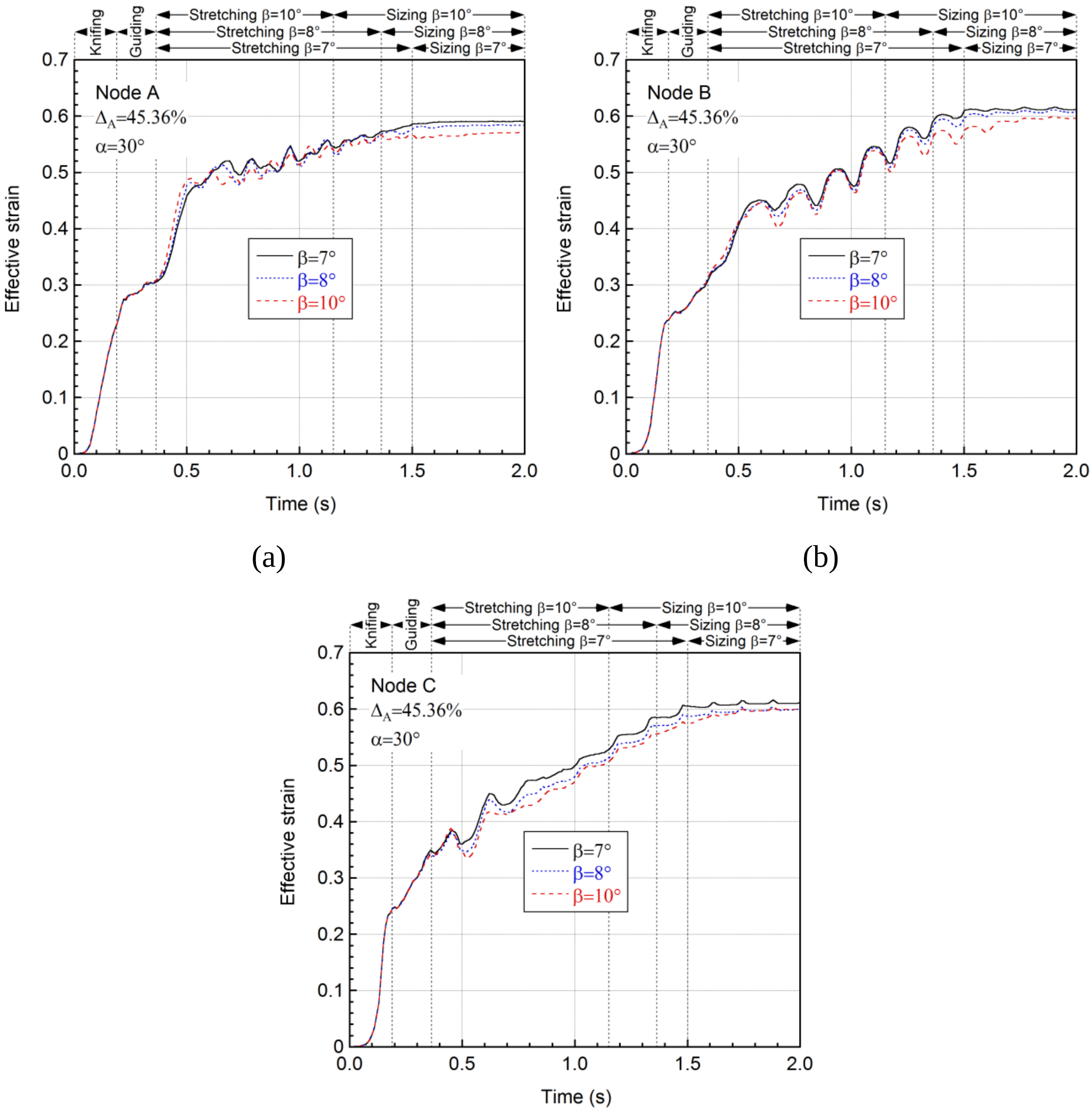

(a)

(b)

(c)

Figure 5.40. The effective strain variations of (a) node A, (b) node B and (c) node C with time at different β values (for Δ_A=45.36% and β=8°).

The effective stress distribution on the yz cross-section of the workpiece as a function of time (t=0.1, 0.3, 0.9 and 1.9 s) corresponding to knifing, guiding, stretching and sizing zone is shown in Figure 5.41 for α=30°, β=8°, and Δ_A=45.36%. It is found that the effective stress distribution is localized on the workpiece surface starting from stretching zone. The effective stress variations with α are shown in Figure 5.42(a-c) for A, B and C point, respectively. The forming angle is found to have minor effect on the workpiece center effective stress starting from stretching zone (Figure 5.42(a)) and increasing the α results in higher stress values. The forming angle is also found to be ineffective in increasing stresses of the workpiece surface and middle points (node B and C) as shown in Figure 5.42(b-c). In Figure 5.43, the effect of β on the effective stress is shown for α=30°, β=8°, and Δ_A=45.36%. The effective stress values decrease in the workpiece center (node A) by increasing β (Figure 5.43(a)). The workpiece surface (node B) and middle (node C) points are not affected significantly by varying β (Figure 5.43(b-c)).

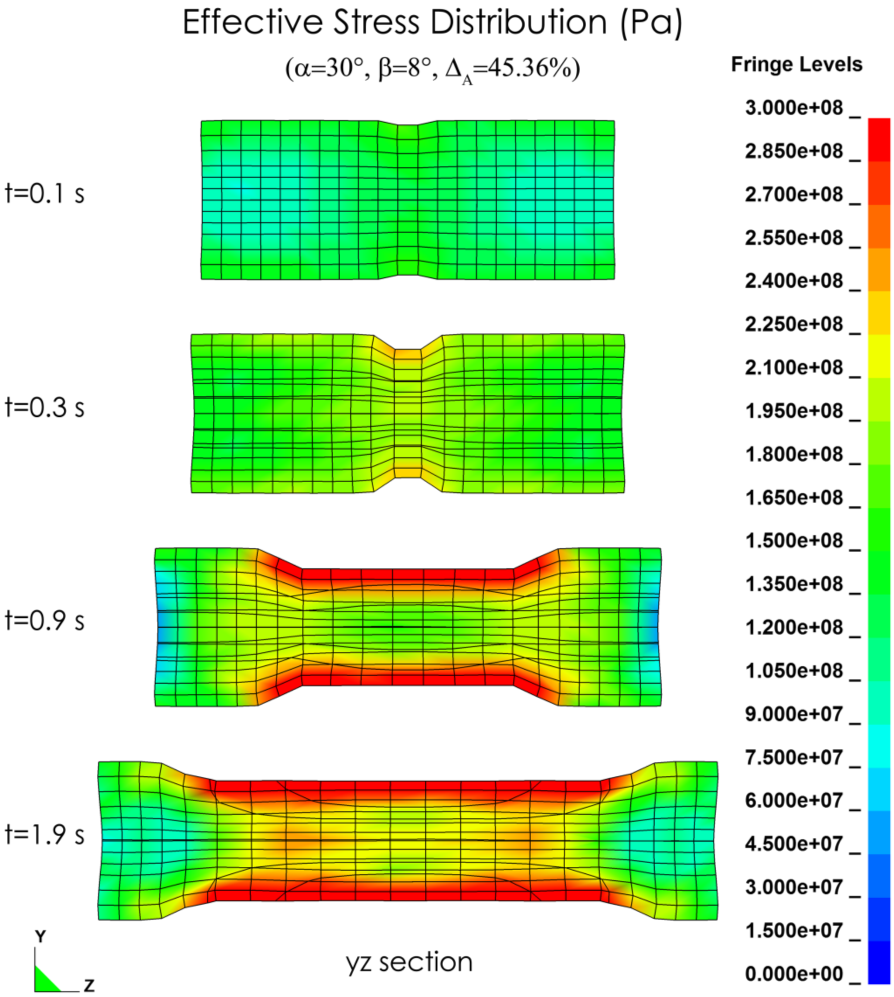

Figure 5.41. The effective stress distribution of the workpiece cross section yz at different rolling times (t=0.1, 0.3, 0.9, 1.9 s) for Δ_A=45.36%, α=30° and β=8°.

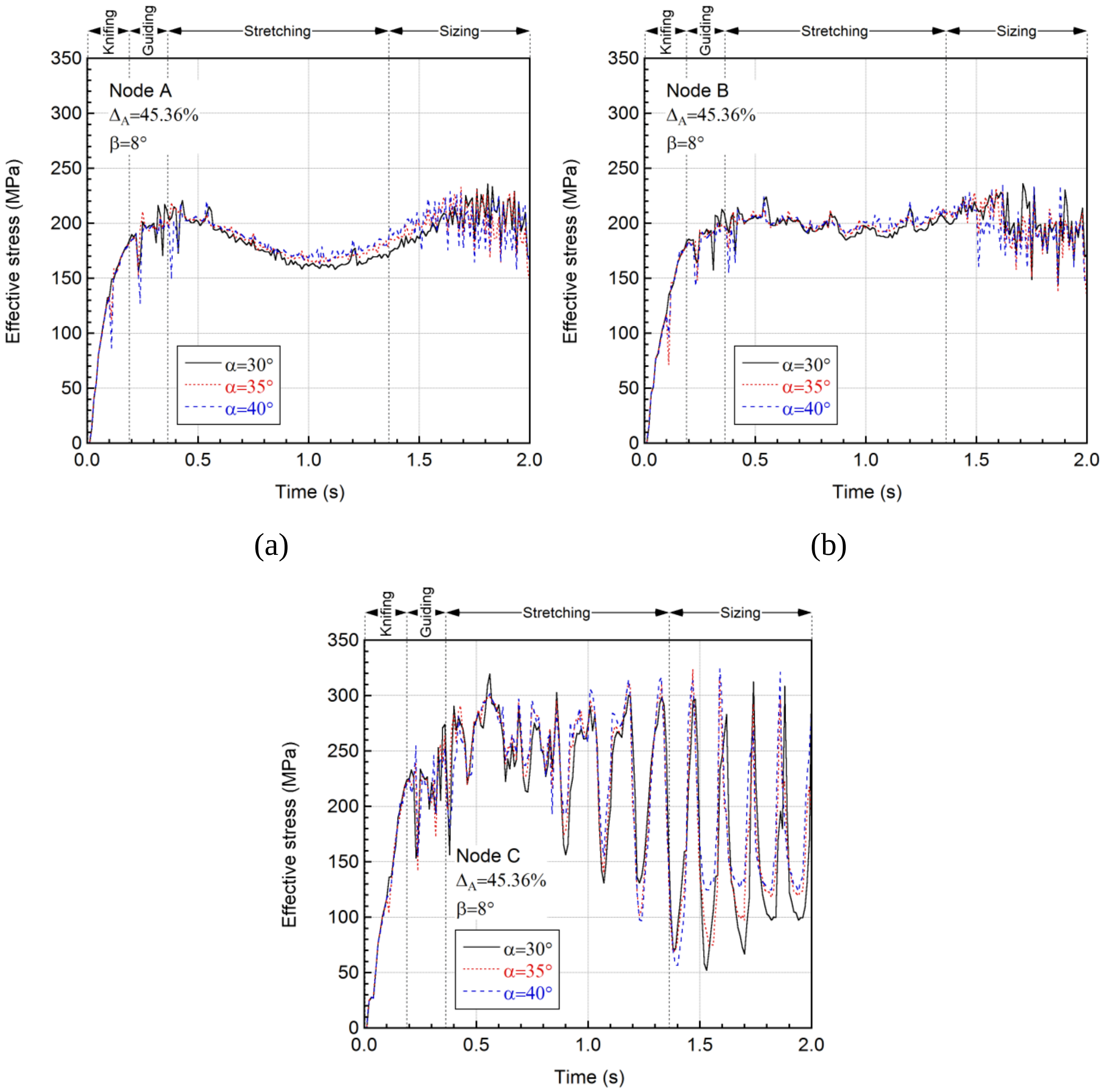

(a)

(b)

(c)

Figure 5.42. The effective stress variations of (a) node A, (b) node B and (c) node C with time at different α values (for Δ_A=45.36% and β=8°).

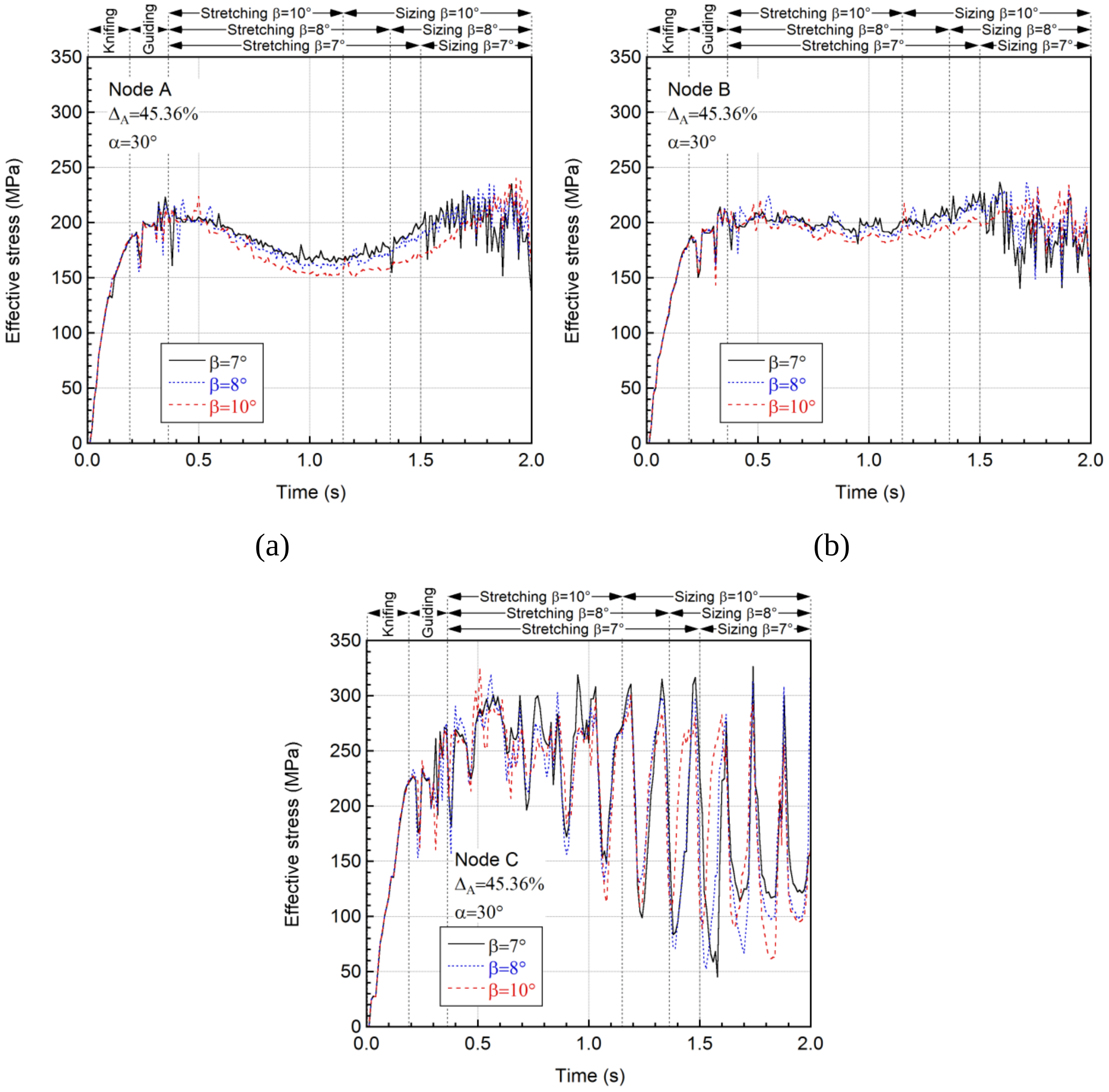

(a) (b)

(c)

Figure 5.43. The effective stress variations of (a) node A, (b) node B and (c) node C with time at different β values (for Δ_A=45.36% and β=8°).

The maximum principal stress distribution on the yz cross-section of the workpiece as a function of time (t=0.1, 0.3, 0.9 and 1.9 s) corresponding to knifing, guiding, stretching and sizing zone is shown in Figure 5.44 for α=30°, β=8°, and Δ_A=45.36%. In this figure, it is seen that the compressive and tensile stress are present on the surface while the workpiece interior only experiences tensile stress. The forming angle and β have almost no effect on the maximum principal stress values, within the studied range of parameters, for all nodes (A, B and C) as seen in Figure 5.45 and Figure 5.46.

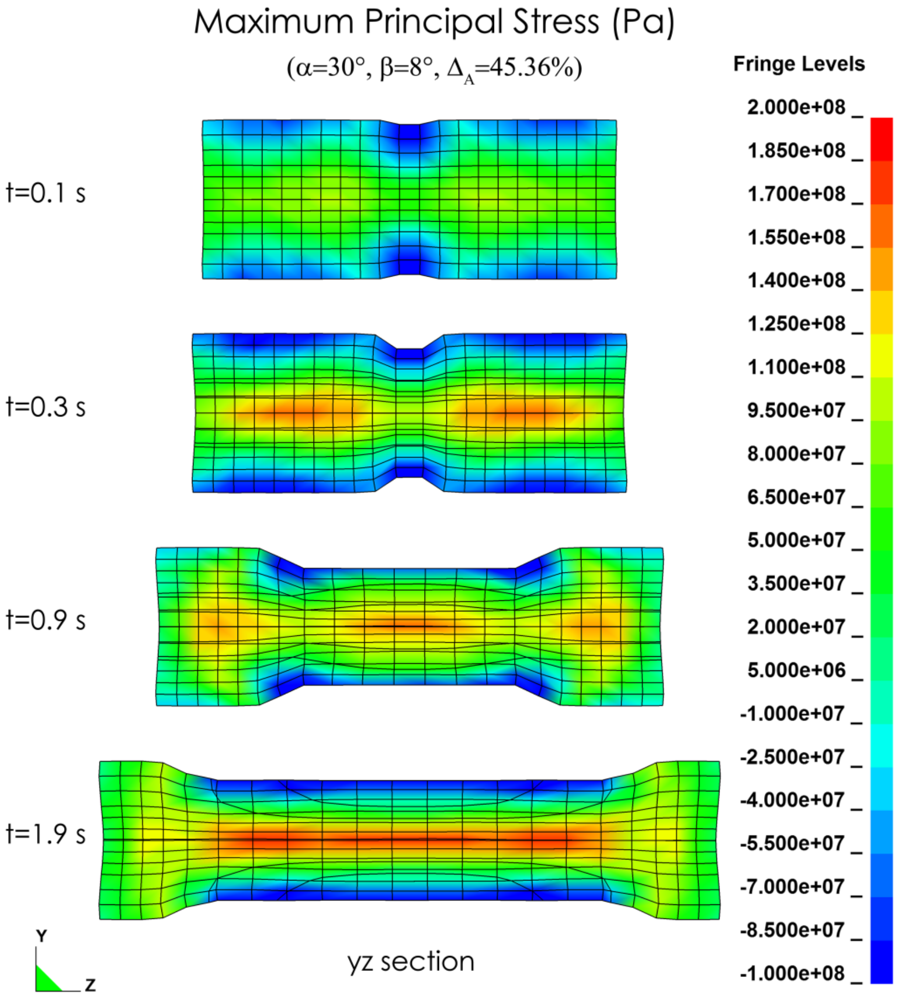

Figure 5.44. The maximum principal stress distribution of the workpiece cross section yz at different rolling times (t=0.1, 0.3, 0.9, 1.9 s) for Δ_A=45.36%, α=30° and β=8°.

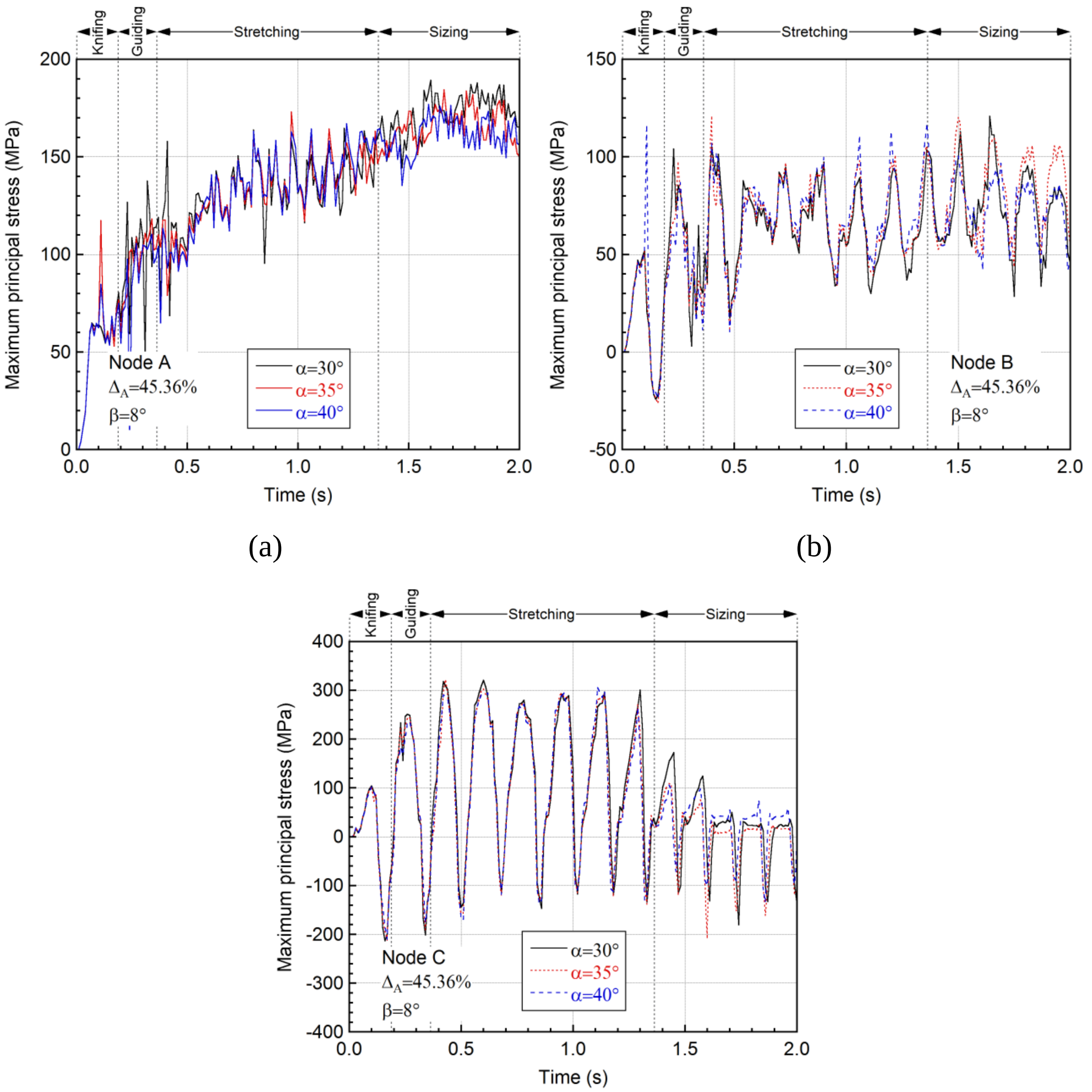

(a)

(b)

(c)

Figure 5.45. The maximum principal stress variations of (a) node A, (b) node B and (c) node C with time at different α values (for Δ_A=45.36%and β=8°).

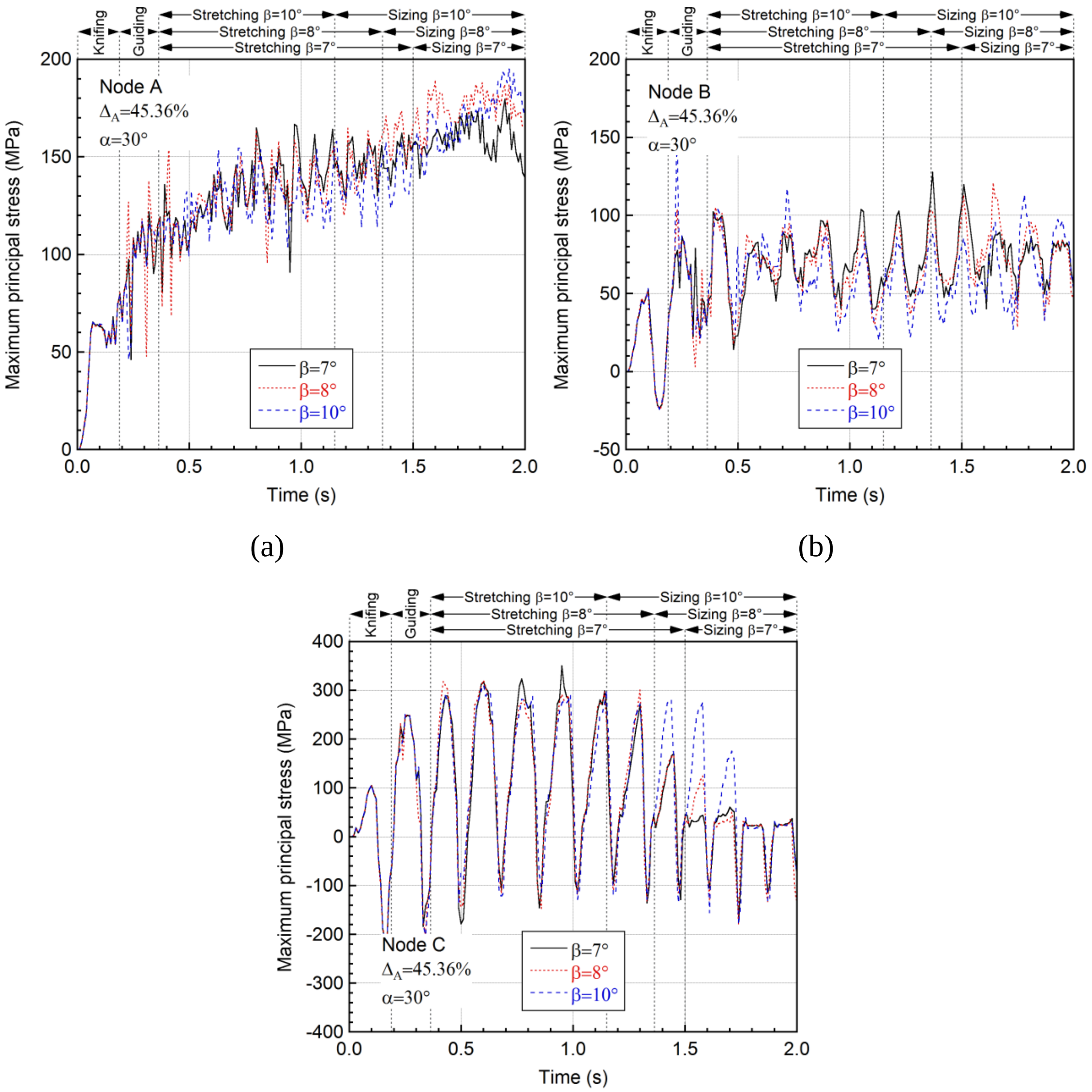

(a) (b)

(c)

Figure 5.46. The maximum principal stress variations of (a) node A, (b) node B and (c) node C with time at different β values (for Δ_A=45.36% and β=8°).

The stress triaxiality distribution on the yz cross-section of the workpiece as a function of time (t=0.1, 0.3, 0.9 and 1.9 s) corresponding to knifing, guiding, stretching and sizing zone is shown in Figure 5.47 for α=30°, β=8°, and Δ_A=45.36%. At t=0.1 and 0.3 s, the stress triaxiality is positive on the workpiece center along the z-axis while it is negative on the workpiece contact surface. Initially, there are two regions where the stress triaxiality is positive and these positive regions are noted to be inspected for failure. After guiding zone (t=0.9 s), the stress triaxiality is the highest at the center. In Figure 5.48(a-c), the stress triaxiality variation with time for node A, B and C is shown for different α values (Δ_A=45.36% and β=8°), respectively. The reduction in the α decreases the stress triaxiality of the workpiece middle point (node B) (Figure 5.48(b)).

The stress triaxiality of workpiece center and surface are noted to be not significantly affected by α. The effect of β on the triaxiality factor for node A, B and C is shown in Figure 5.49(a-c). The stretching angle has insignificant effect on the stress triaxiality of the workpiece center. On the other hand, increasing the β decreases the stress triaxiality at the middle (Figure 5.49(b)). In contrast, the triaxiality of the surface increases with decreasing β (Figure 5.49(c)).

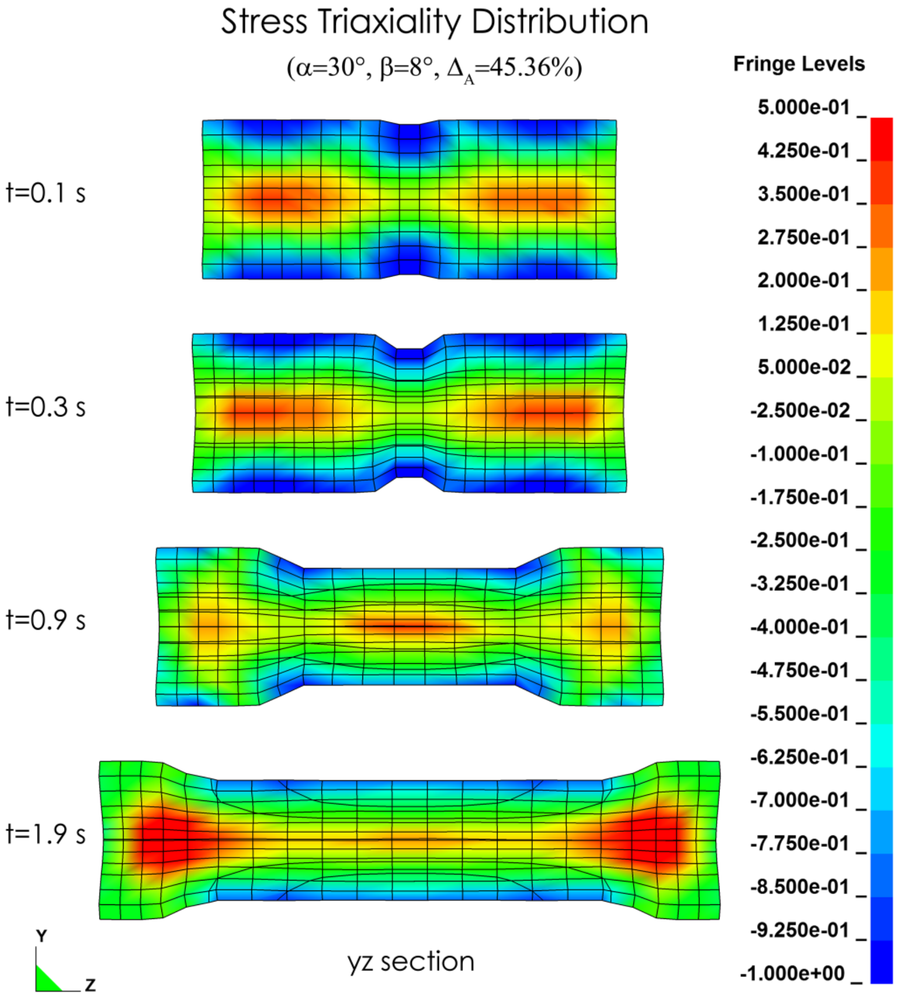

Figure 5.47. The stress triaxiality distribution of the workpiece cross section yz at different rolling times (t=0.1, 0.3, 0.9, 1.9 s) for Δ_A=45.36%, α=30° and β=8°.

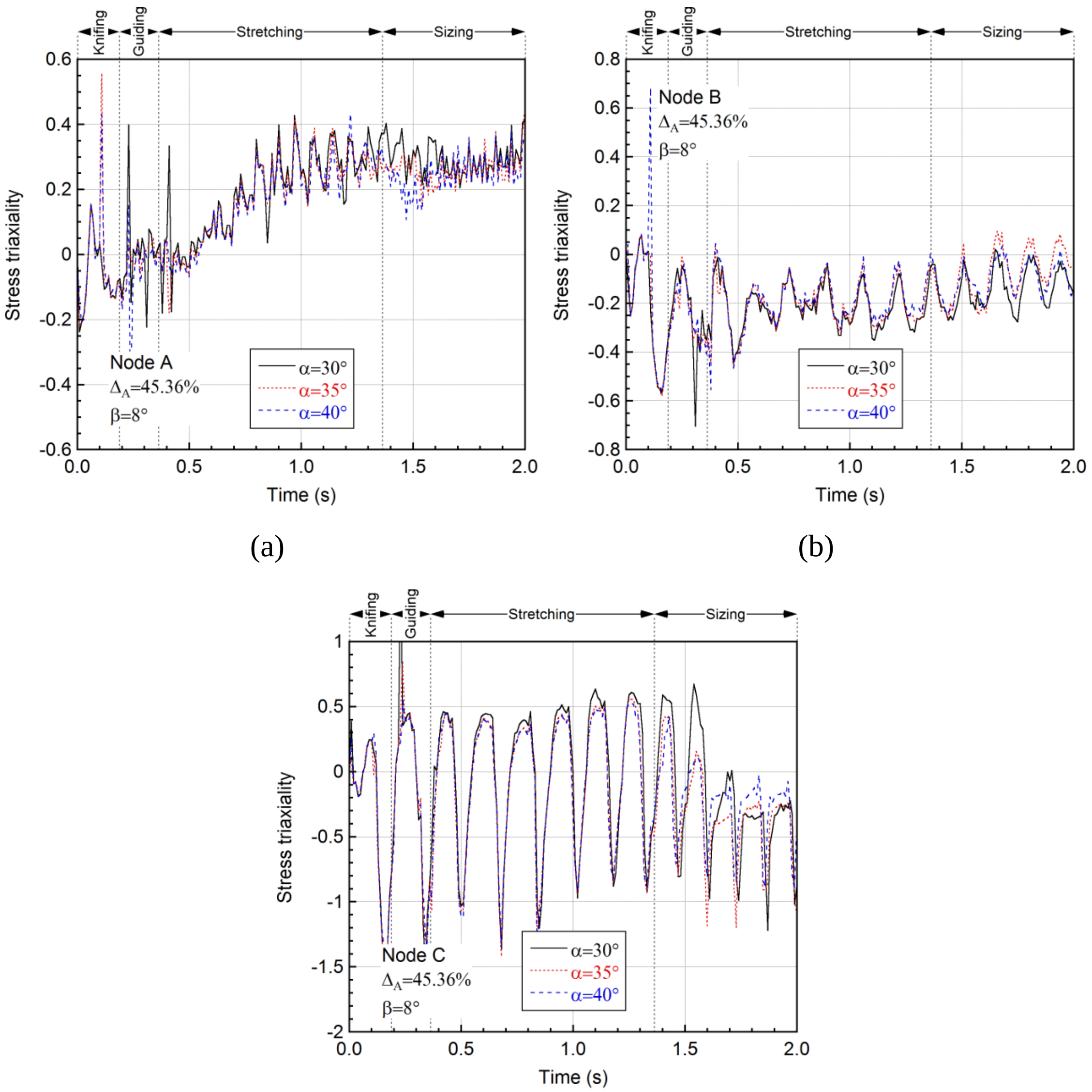

(a)

(b)

(c)

Figure 5.48. The stress triaxiality variations of (a) node A, (b) node B and (c) node C with time at different α values (for Δ_A=45.36% and β=8°).

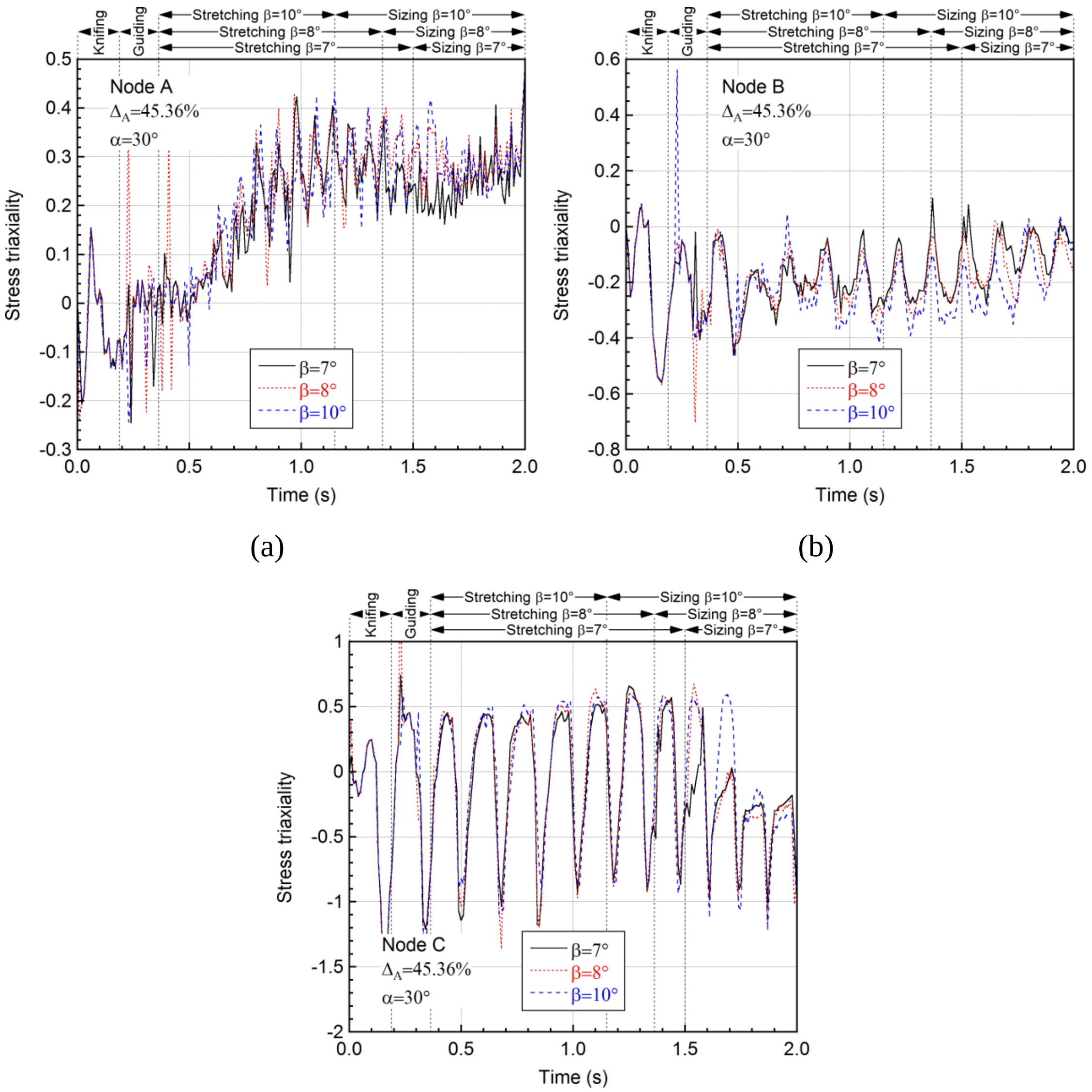

(a) (b)

(c)

Figure 5.49. The stress triaxiality variations of (a) node A, (b) node B and (c) node C with time at different β values (for Δ_A=45.36% and β=8°).

The variations of the effective strain rate at the workpiece center for different α, and β values are shown in Figure 5.50(a-b). The forming angle is seen to have an insignificant effect on the effective strain rate (Figure 5.50(a)), while increasing the β slightly increases the effective strain rate. The effective strain rate variation of the center, middle and surface are shown in Figure 5.50(c). The highest effective strain rate occurs at the workpiece center, while the lowest at surface.

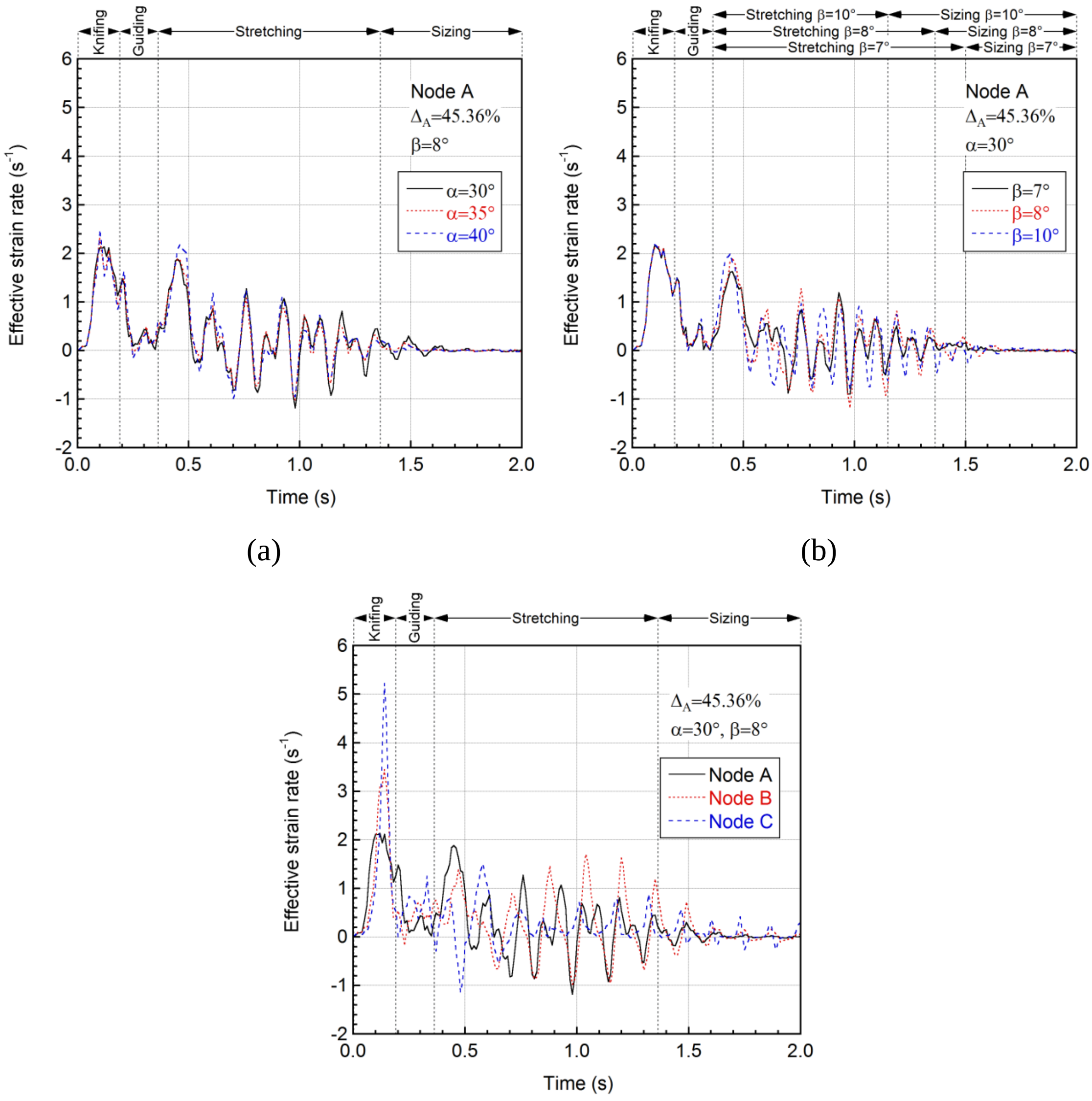

(a) (b)

(c)

Figure 5.50. The variations of the effective strain rate at center (node A) with (a) α and (b) β and (c) the variations of the effective strain rate at center, middle and surface.

5.2.3. Effect of Friction

Figure 5.51 shows the workpiece temperature variations with time for the friction coefficient of 0.3, 0.5 and 0.8 for α=30°, β=8° and Δ_A=31.75%. It is seen that the friction coefficient does not affect the workpiece temperature until the beginning of the stretching zone. The surface temperature of the workpiece increases as the friction coefficient increases. Increasing the friction coefficient to 0.8 does not affect the temperature values of workpiece center and middle point. It is also noted that the temperature oscillations of workpiece surface shifts at varying friction coefficients. This shift results from the workpiece slipping, altering with the values of the friction coefficient. The effective strain of the center, middle and surface point also increases with increasing the friction coefficient as shown in Figure 5.52(a-c), respectively. This behavior is attributed to increase slipping at lower friction coefficients. It is also found that the friction has no influence on the effective stress values of the investigated nodes (Figure 5.53(a-c)). The maximum principal stress values of the workpiece surface are not affected by the friction coefficient (Figure 5.54(c)). As the friction coefficient increases, the maximum principal stress at the workpiece center and middle (node A and B) increases in stretching zone and decreases in the sizing zone (Figure 5.54(a-b)). The stress triaxiality variations of the workpiece center, middle and surface are shown in Figure 5.55(a-c), respectively. At the workpiece center and the middle, the triaxiality factor increases in guiding and stretching zones with decreasing the friction coefficient. In contrast with nodes A and B, the stress triaxiality on the workpiece surface decreases with decreasing the friction coefficient in both stretching and sizing zone. The strain rate decreases at the workpiece center in the stretching zone (Figure 5.56(a)), while increases in the middle and on the surface in stretching zone (Figure 5.56(b-c)) with increasing the friction coefficient.

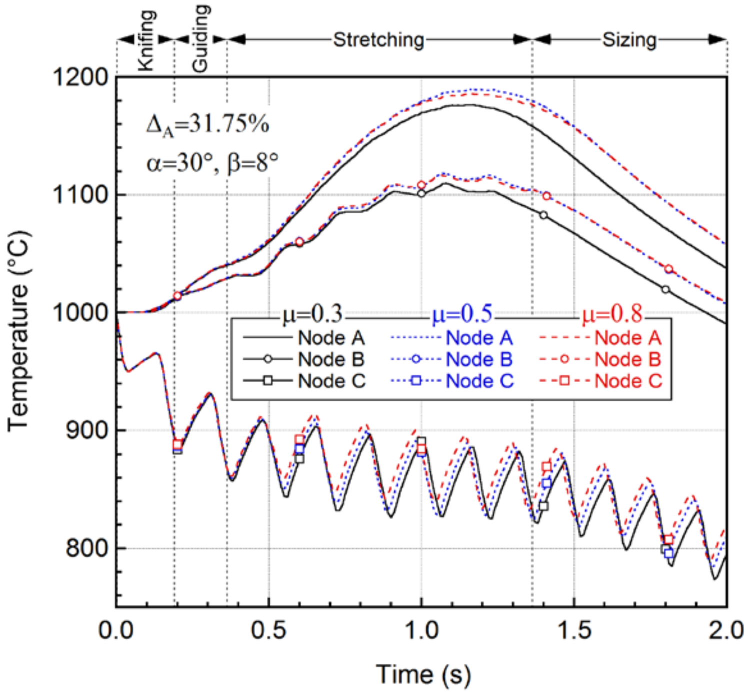

Figure 5.51. The temperature variations of nodes A, B and C for different friction coefficients (α=30°, β=8° and Δ_A=31.75%).

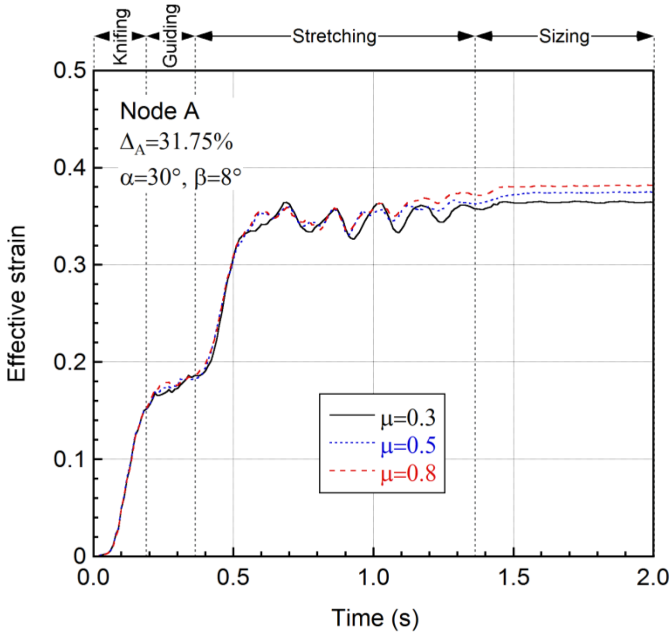

(a)

Figure 5.52. The effective strain variations of (a) node A, (b) node B and (c) node C at different friction coefficients (α=30°, β=8° and Δ_A=31.75%).

(cont. on next page)

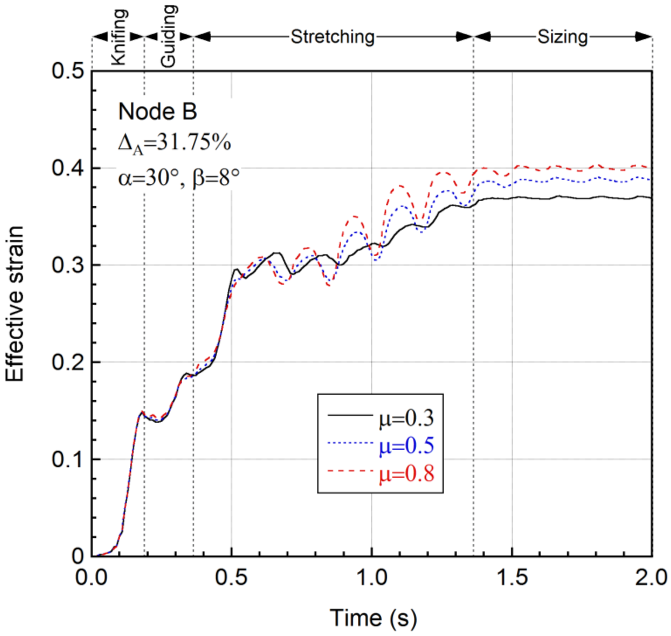

(b)

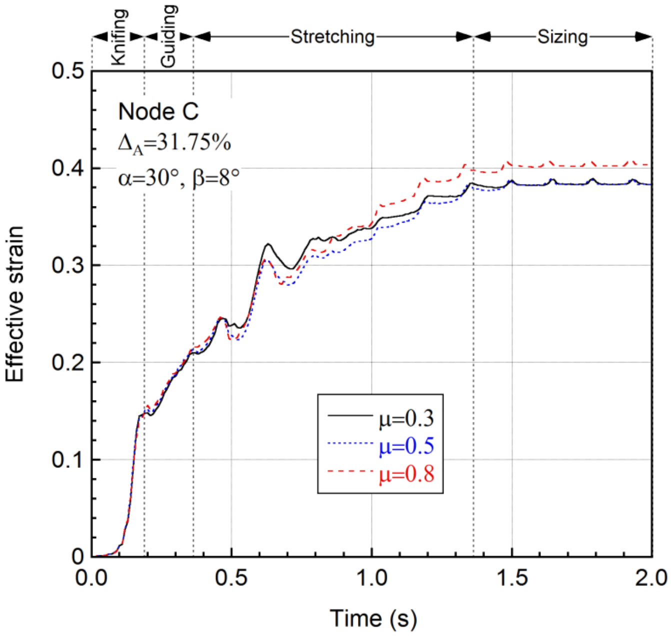

(c)

Figure 5.52. (cont.)

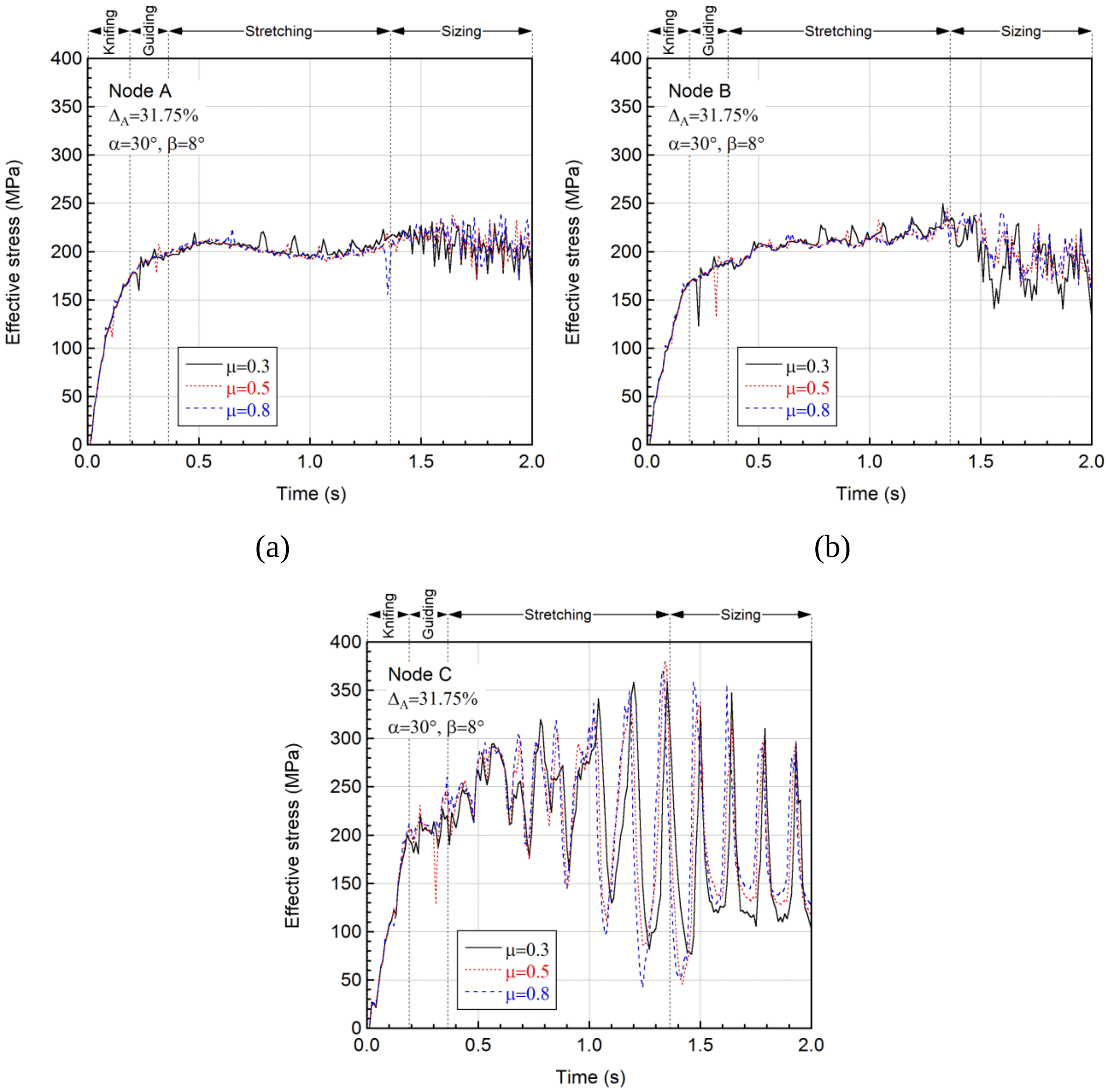

(a)

(b)

(c)

Figure 5.53. The effective stress variations of (a) node A, (b) node B and (c) node C at different friction coefficients (α=30°, β=8° and Δ_A=31.75%).

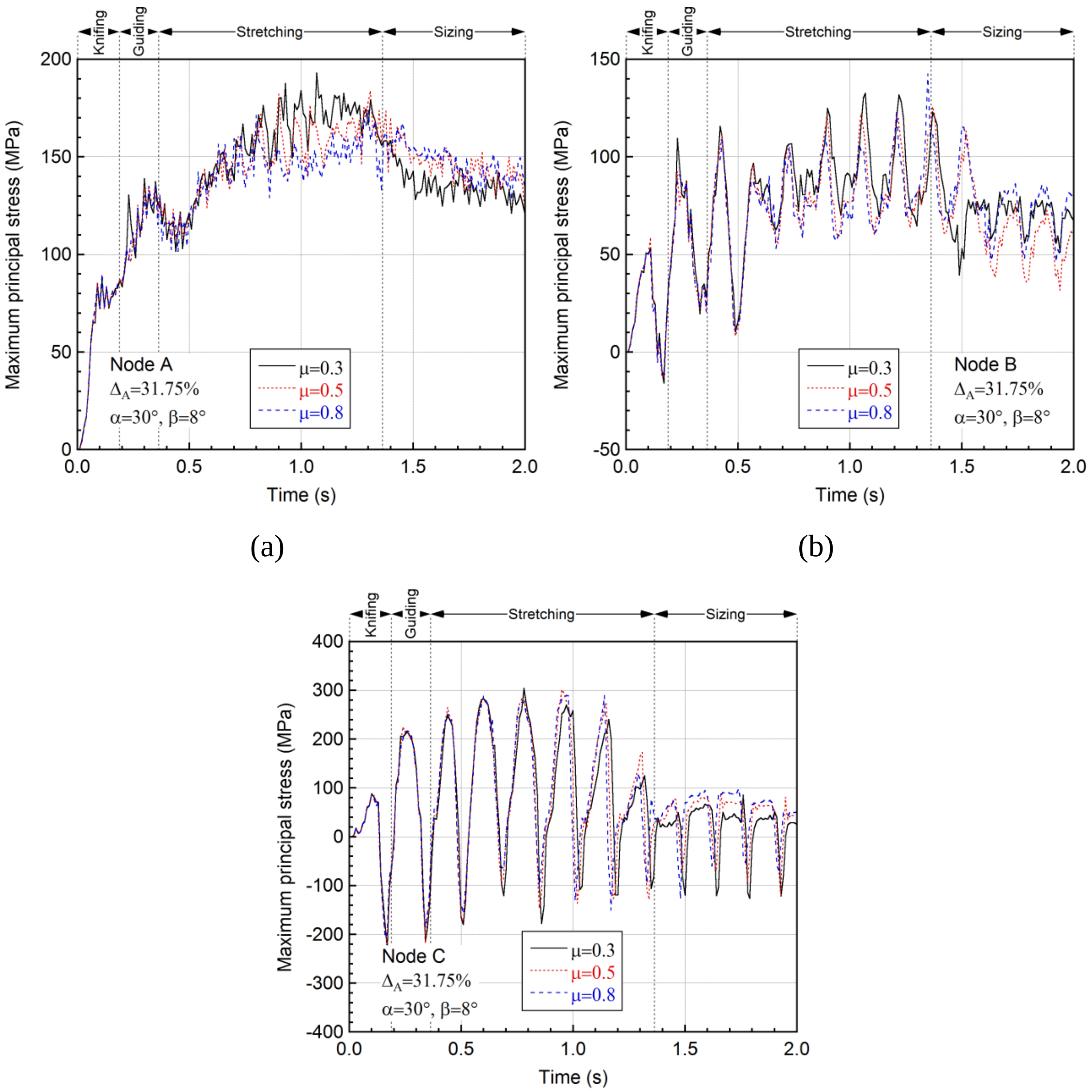

(a)

(b)

(c)

Figure 5.54. The maximum principal stress variations of (a) node A, (b) node B and (c) node C at different friction coefficients (α=30°, β=8° and Δ_A=31.75%).

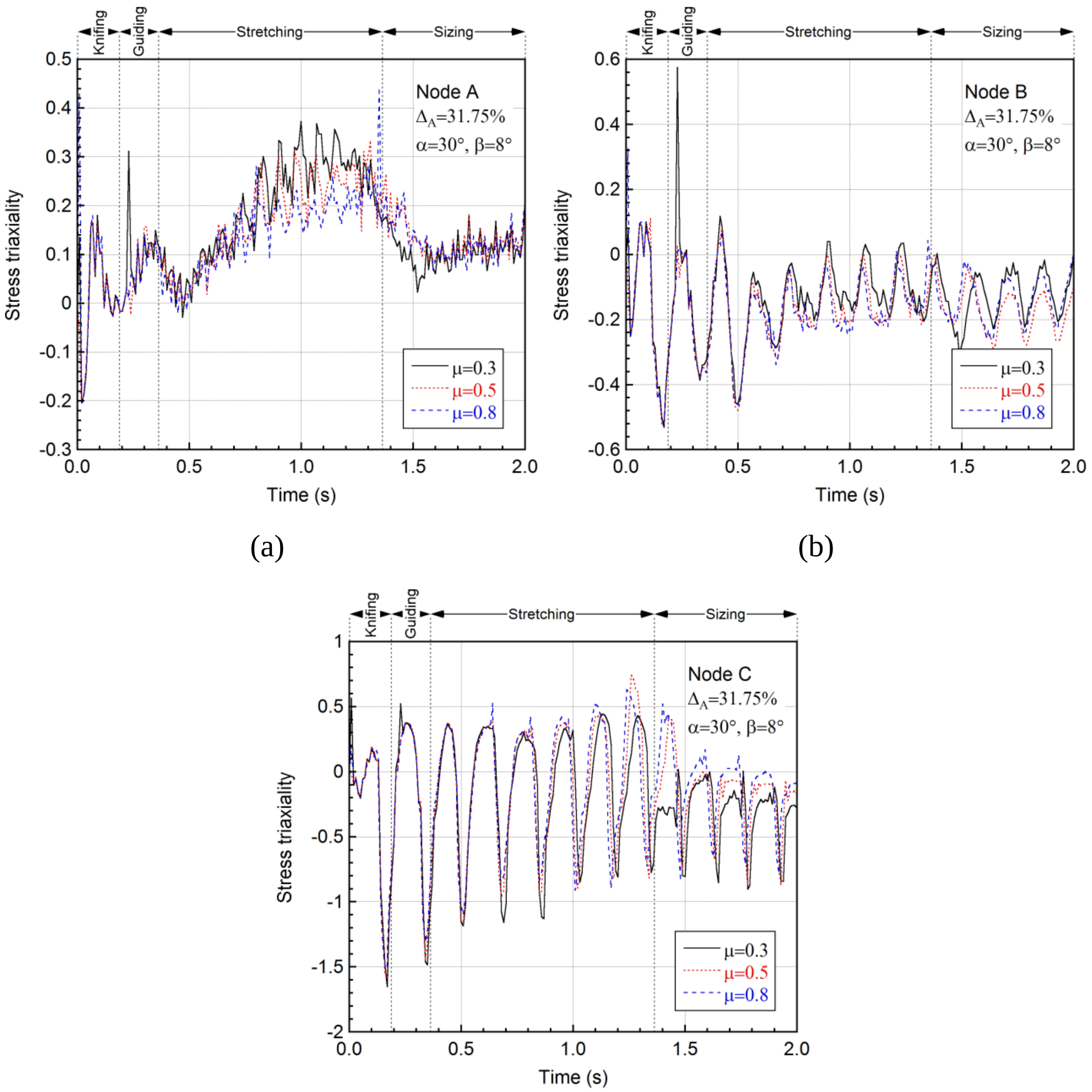

(a) (b)

(c)

Figure 5.55. The stress triaxiality variations of (a) node A, (b) node B and (c) node C at different friction coefficients (α=30°, β=8° and Δ_A=31.75%).

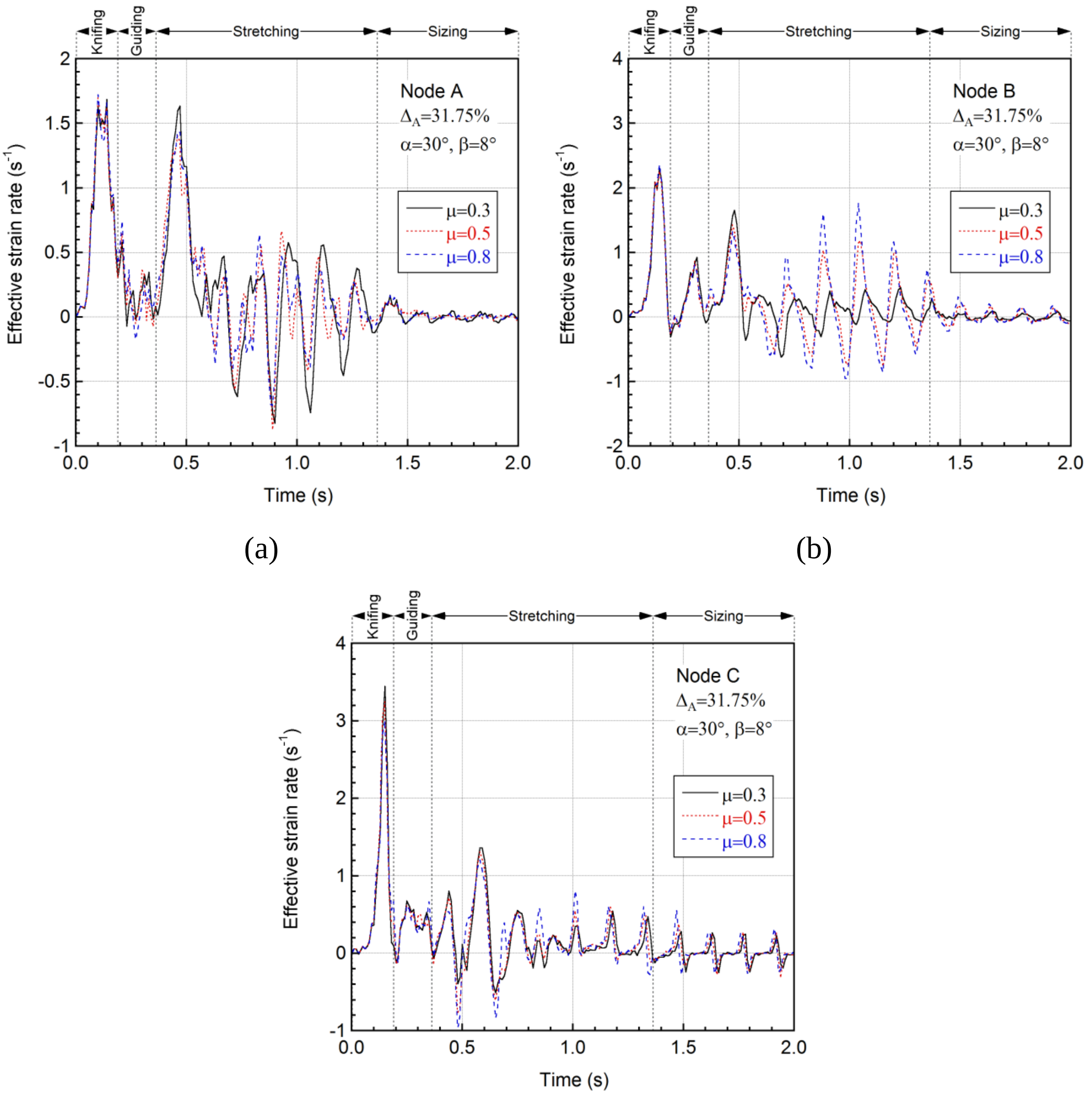

(a)

(b)

(c)

Figure 5.56. The effective strain rate variations of (a) node A, (b) node B and (c) node C at different friction coefficients (α=30°, β=8° and Δ_A=31.75%).

5.3. Tractor Shaft Model

The variations of the effective plastic strain, temperature and effective strain rate of the tractor shaft model are investigated for four different nodes on the workpiece as shown in Figure 5.57(a) and (b). These points are selected along the z-axis of the workpiece at the center, surface and shoulders.

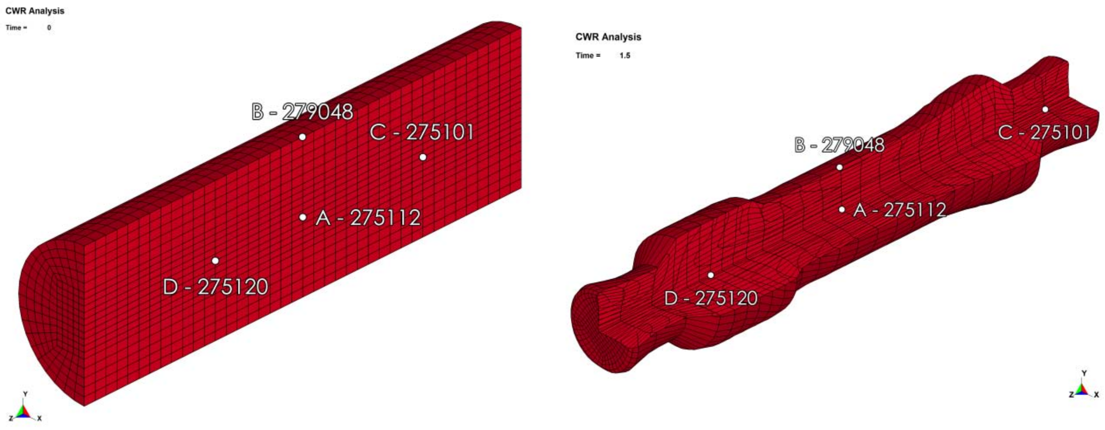

(a) (b)

Figure 5.57. The selected nodes on the tractor shaft (A, B, C and D): (a) t=0 s and (b) t=1.5 s.

5.3.1. AISI 1045 Steel

Figure 5.58(a) and (b) show the effective strain distribution of the workpiece at t=1 second. The strain values are the highest on the surface while the lowest on shoulders of the workpiece. In Figure 5.59(a) and (b), the workpiece temperature distribution is shown at t=1 s. The highest temperature is found at the center while the lowest is on the surface of the workpiece. Figure 5.60(a) and (b) show the effective strain and temperature distribution of the workpiece in yz cross-section at t=1.5 s (just before the cutting zone). At this time of the process, the workpiece shoulders form with the highest strain values. The center zone of the workpiece has average strain, while the zone between center and shoulders has the lowest strain values (Figure 5.60(a)). The highest temperature values are seen on the shoulders when t=1.5 s while the surface has the lowest strain (Figure 5.60(b)).

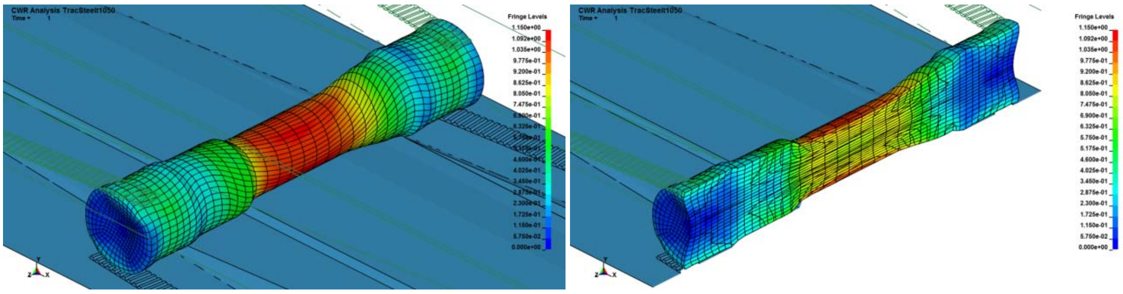

(a) (b)

Figure 5.58. The effective strain distribution of the workpiece (a) isometric view and (b) yz cross-section at t=1 s.

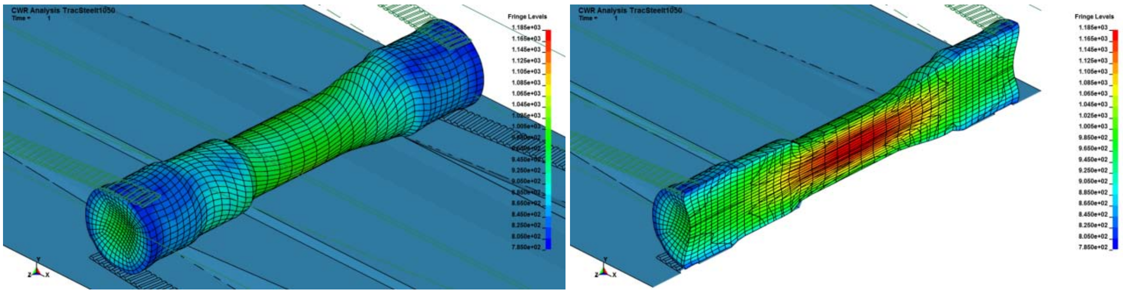

(a) (b)

Figure 5.59. The temperature distribution of the workpiece (a) isometric view and (b) yz cross-section at t=1 s.

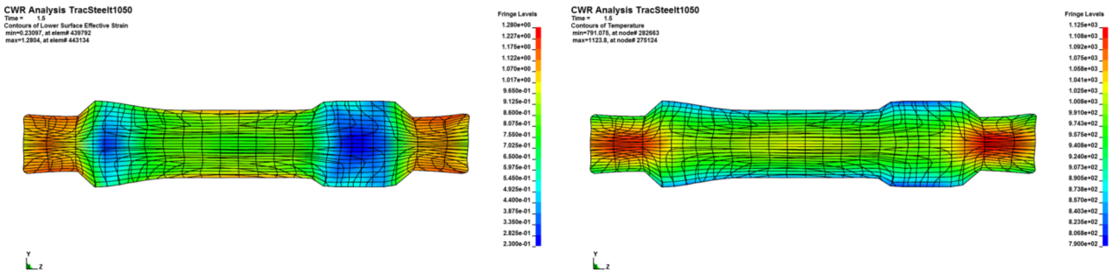

(a) (b)

Figure 5.60. The distribution of (a) effective strain and (b) temperature on the yz cross-section at t=1.5 s.

The effective strain at center and surface (nodes A and B) increases at the beginning and become constant later steps until the end of process (Figure 5.61(a)). The strain values at the shoulder point increase once more at the end of process, which shows that the workpiece has reached to the cutting zone. The highest temperature is found at the workpiece center (node A) (Figure 5.61(b)). In the same figure, the temperature of the shoulder (Node D) increases about 100 °C in stretching zone and at the end of the process, center and shoulder points are equal. In Figure 5.61(c), the effective strain rate value of center point (Node A) is shown to fluctuate at the beginning of stretching zone, showing the forming process while the strain rate of shoulder point (Node C) increases at the end of this zone, showing shoulder formation at this stage of process. The tool force is the highest in the knifing zone and at the later steps, stays constant up to cutting zone (Figure 5.61(d)).

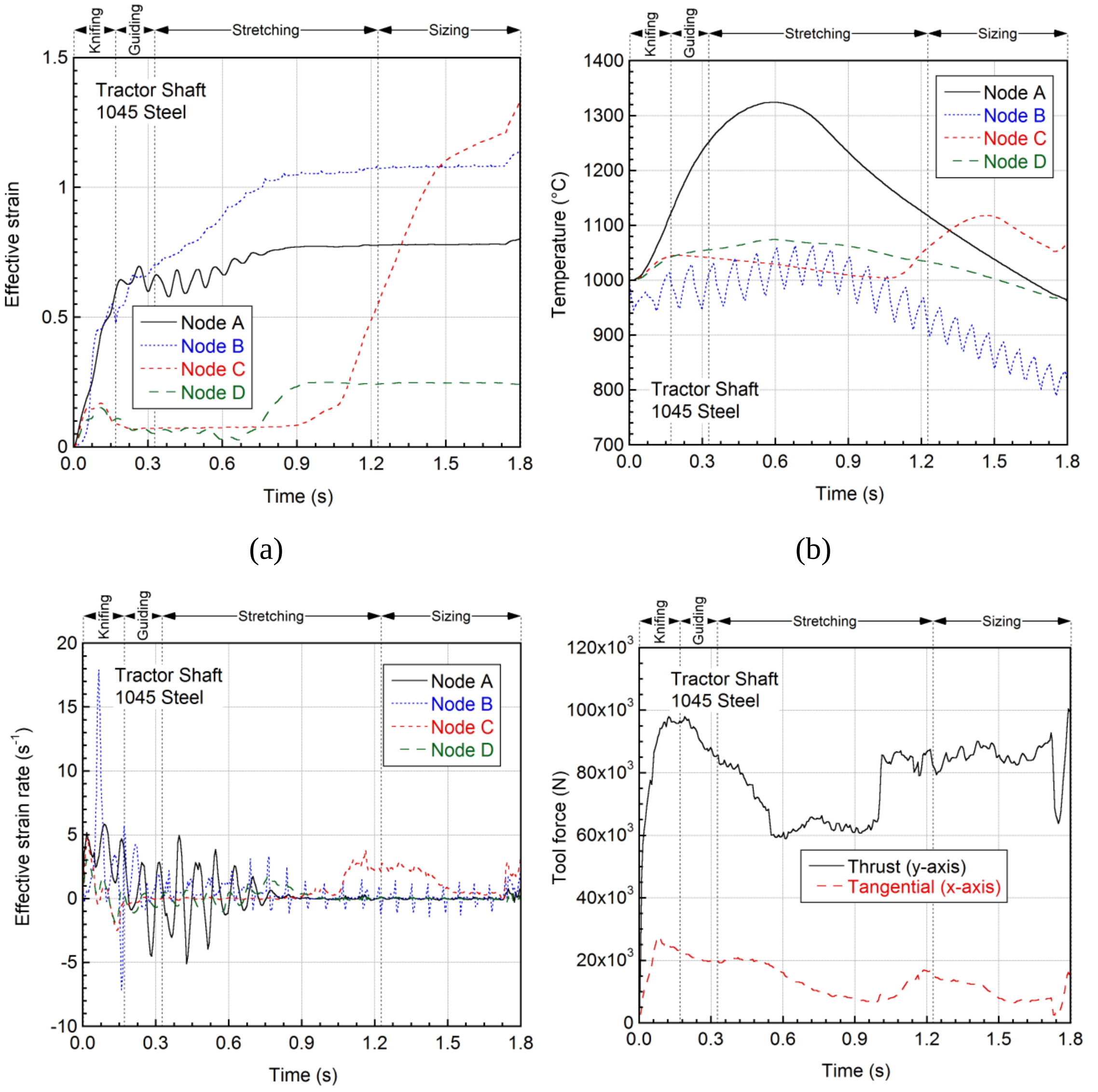

(a) (b)

(c) (d)

Figure 5.61. The variations of (a) effective plastic strain, (b) temperature (c) effective strain rate at nodes A, B, C and D, and (d) tool forces with respect to time.

5.3.2. Ti6Al4V

Figure 5.62(a) and (b) show the effective strain distribution of the workpiece when t=1 s. Similar to the steel workpiece, the strain values are highest on the surface. In Figure 5.63(a) and (b), the workpiece temperature distribution is shown at t=1 s. The highest temperature is found at the center, while the lowest is on the surface of the workpiece. Figure 5.64(a) and (b) show the effective strain and temperature distribution of the workpiece yz cross-section at t=1.5 s (just before the cutting zone), respectively. Similar to steel workpiece, the center zone of the workpiece has average strain values while the zone between center and shoulders has the lowest strain values (Figure 5.64(a)). The highest temperature values are also found on the shoulders at t=1.5 s while the surface has the lowest temperature (Figure 5.64(b)).

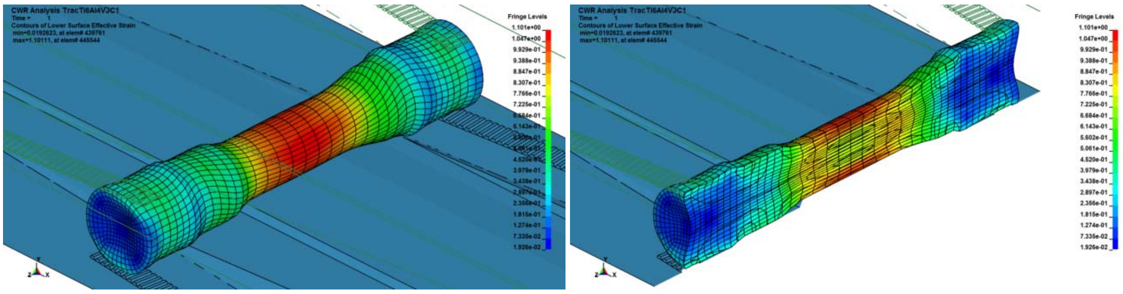

(a) (b)

Figure 5.62. The effective strain distribution of the workpiece (a) isometric view and (b) yz cross-section at t=1 s (JC-1 material model).

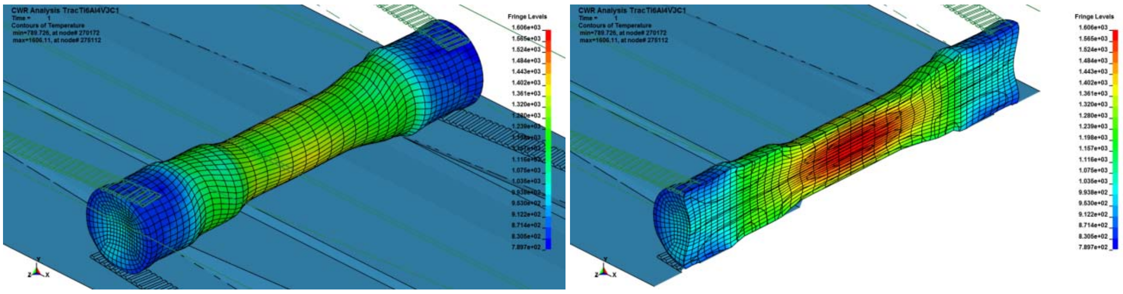

(a) (b)

Figure 5.63. The temperature distribution of the workpiece (a) isometric view and (b) yz cross-section at t=1 s (JC-1 material model).

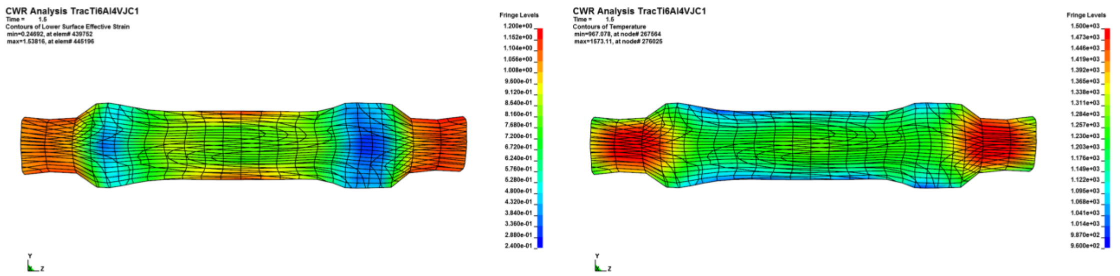

(a) (b)

Figure 5.64. The distribution of (a) effective strain and (b) temperature on the yz cross-section at t=1.5 s (JC-1 material model).

The effective strain at center and surface (nodes A and B) first increases and then stays constant until the end of process (Figure 5.65(a)). The strain values at shoulder point (Node C) increase once more at the end of process, which shows that the workpiece has reached to the cutting zone. The highest temperature variation is found on the workpiece center (node A) (Figure 5.65(b)). The extreme temperature increase in Ti6Al4V workpiece results from the high deformation forces converted into heat. In the same figure, the temperature of the shoulder (Node D) increases about 300 °C in stretching zone and at the end of the process, which is a result of conduction from the center. In Figure 5.65(c), the effective strain rate value of center point (Node A) is seen to fluctuate at the beginning of stretching zone, showing the forming process while the strain rate value of shoulder point (Node C) increases at the end of this zone, showing the shoulder formation at this stage of process. Finally, the tool forces are the highest in the knifing zone and at the later steps, stay almost constant up to cutting zone (Figure 5.65(d)).

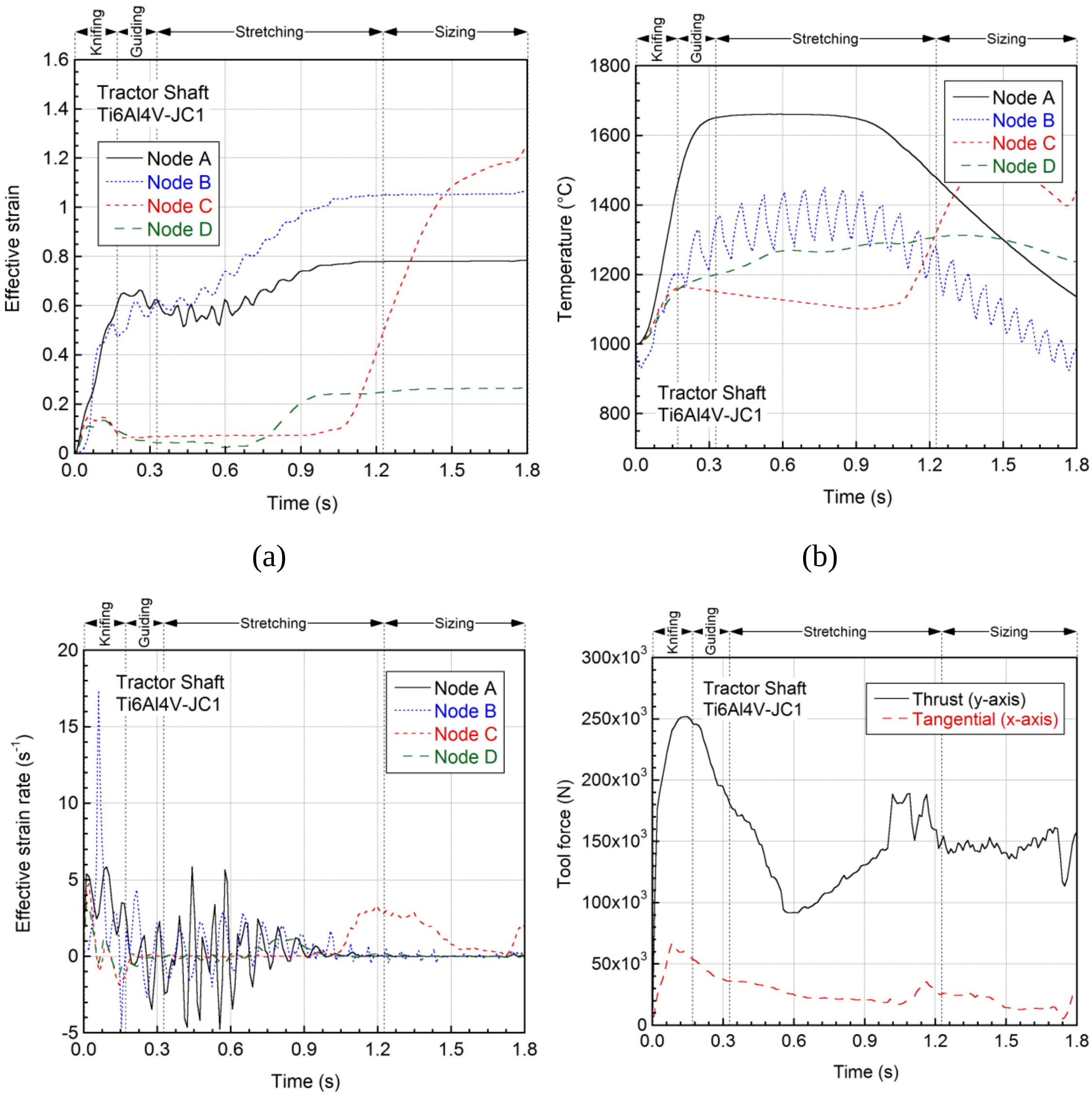

(a) (b)

(c) (d)

Figure 5.65. The variations of (a) effective plastic strain, (b) temperature (c) effective strain rate at nodes A, B, C and D, and (d) tool forces with respect to time (JC-1 material model).

5.4. Microscopic Study

The microstructure of 1045 steel workpiece before CWR process is shown in Figure 5.66(a), which is composed of ferrite (bcc) grains and pearlite (ferrite + cementite). Because of the hot rolling, at the surface of the workpiece a decarburized region, in which the alpha percentage is relatively high, is seen in Figure 5.66(b). The grain size is also seen to be smaller at the surface than the mid section of the workpiece. The grain size in the mid sections is greater than 100 μm. The temperature and equivalent strain distribution of the workpiece after CWR process are shown in Figure 5.67(a) and (b) respectively. The corresponding microstructures of the workpiece at point 1 (surface), 2 (mid near the edge), 3 (mid region) and 4 (thick region near the edge) in the same figure are shown sequentially in Figure 5.68(a-d). The grain size is greatly reduced near the surface of the workpiece, region 1 (Figure 5.68(a), after CWR process. This is expected since the equivalent strain and temperature are the highest at the surface. In region 2, Figure 5.68(b), still the grain size is smaller than the starting workpiece. Again, the equivalent strain and temperature are high in this region. In the mid sections, Region 3, the grains are elongated normal to the rolling direction (Figure 5.68(c)). Finally, in region 4, the grains are observed to be very large (Figure 5.68(d)), as the equivalent strain is relative low in this section. During, CWR process, dynamic recrystallization takes place. The recrystallization depends on the magnitude of the strain and the temperature and closely correlates with the numerically determined equivalent strain values. The tensile stress-strain behavior of the workpiece after and before CWR process is shown in Figure 5.69 for comparison. The tensile test specimens were machined from the mid sections of the workpiece (region 3). The increased ductility of the workpiece after CWR process is clearly seen in Figure 5.69. CWR process however does not affect the yield and ultimate tensile stress behavior of the workpiece.

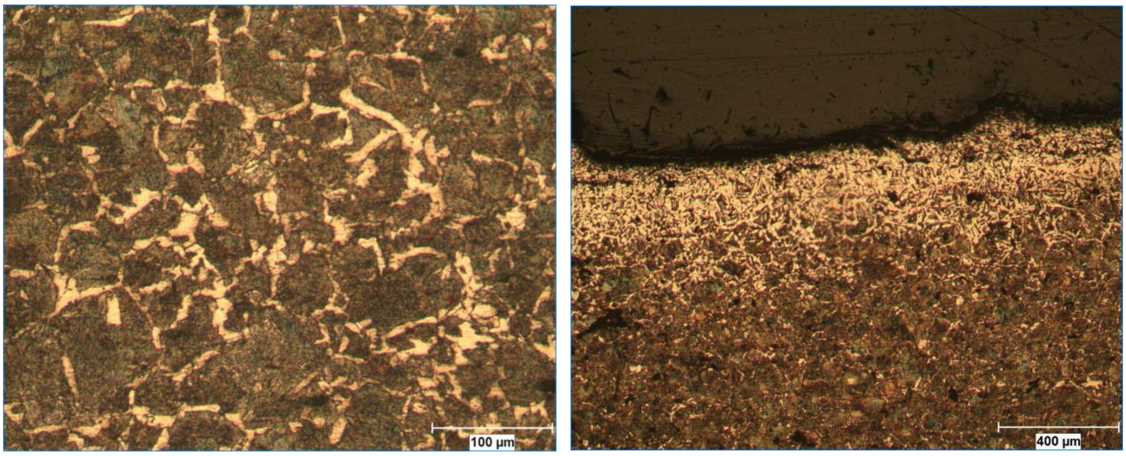

(a) (b)

Figure 5.66. The microstructure of 1045 workpiece before CWR process; (a) mid sections and (b) near the edge.

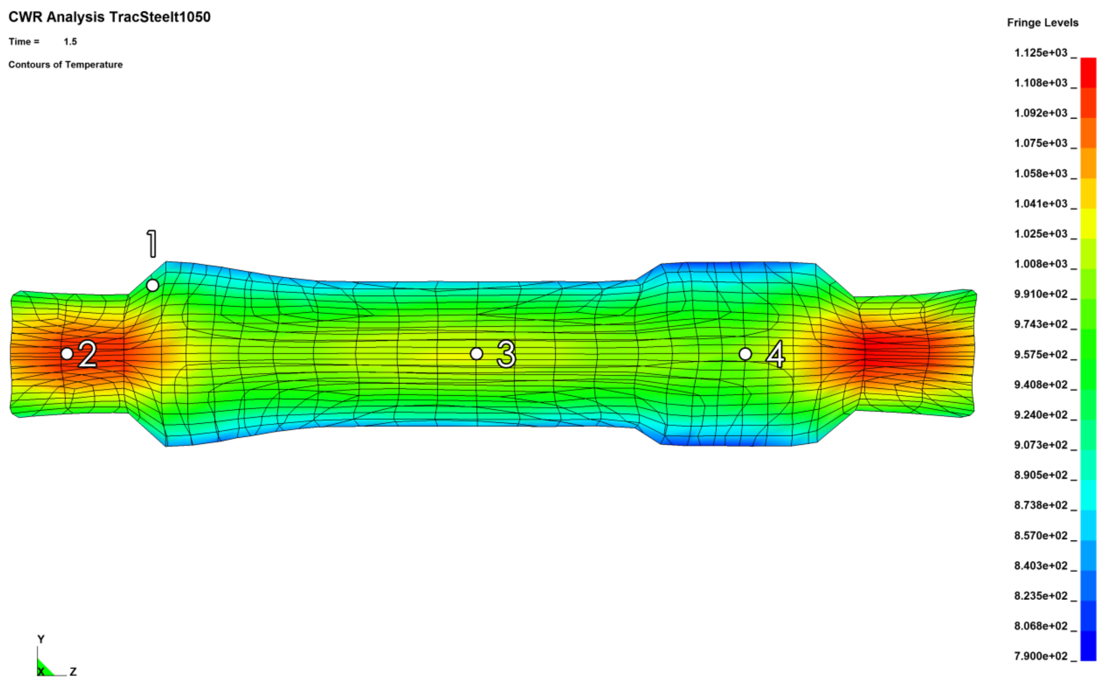

(a)

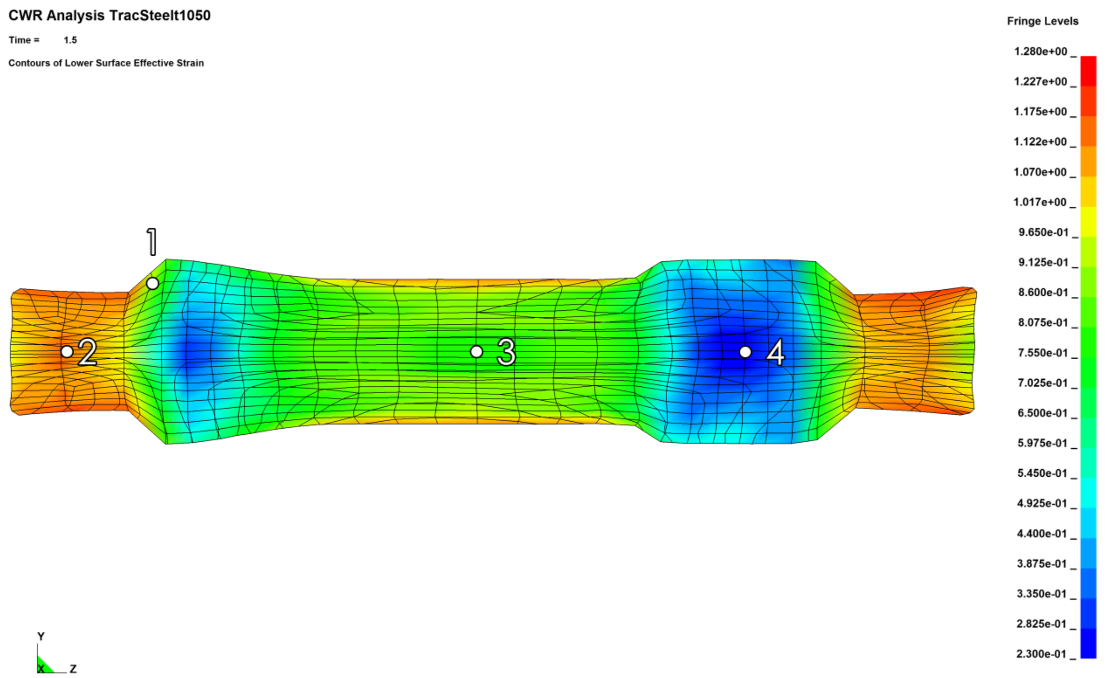

(b)

Figure 5.67. (a) Temperature and (b) equivalent strain distribution of 1045 steel workpiece at the end of CWR.

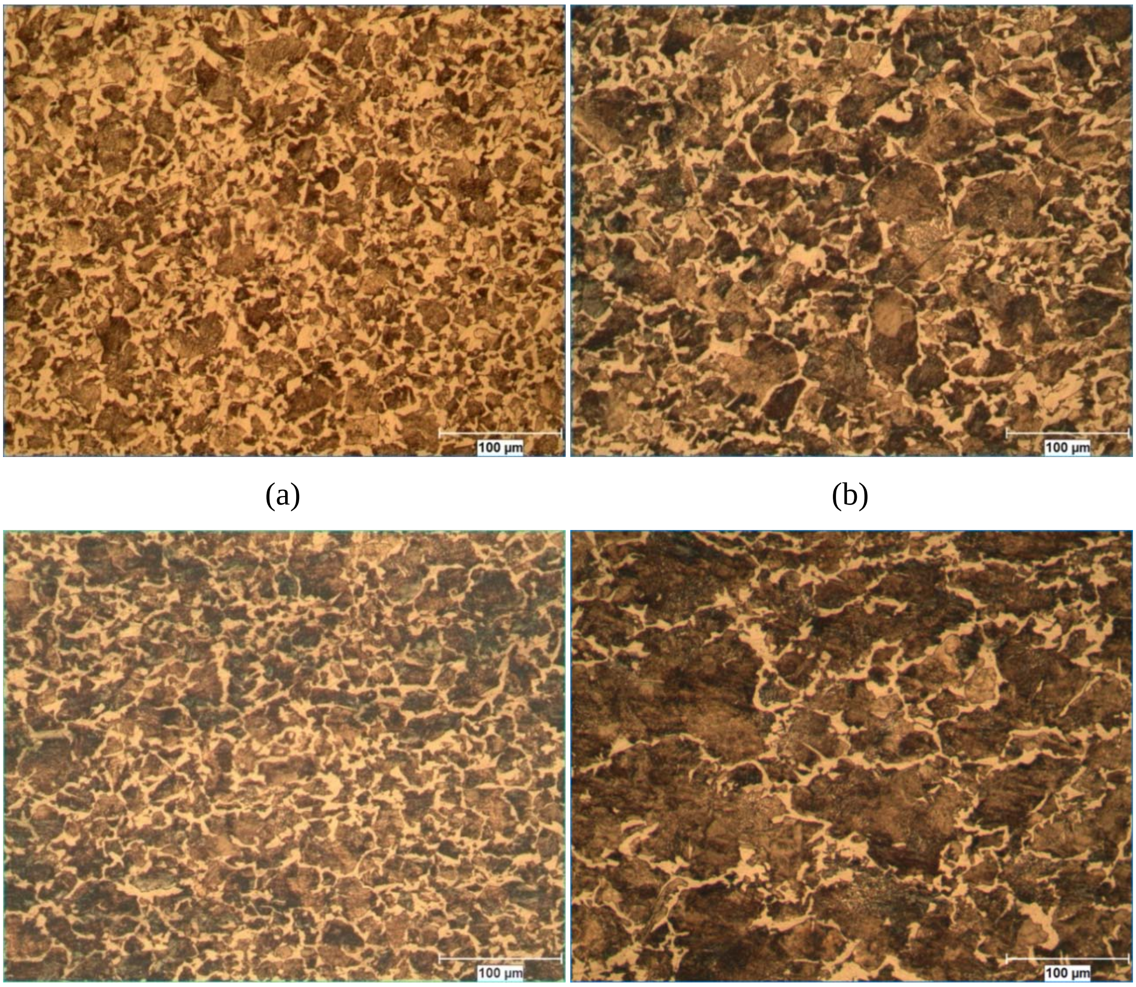

(a) (b)

(c) (d)

Figure 5.68. The microstructure of rolled 1045 steel: region (a) 1, (b) 2, (c) 3 and (d) 4.

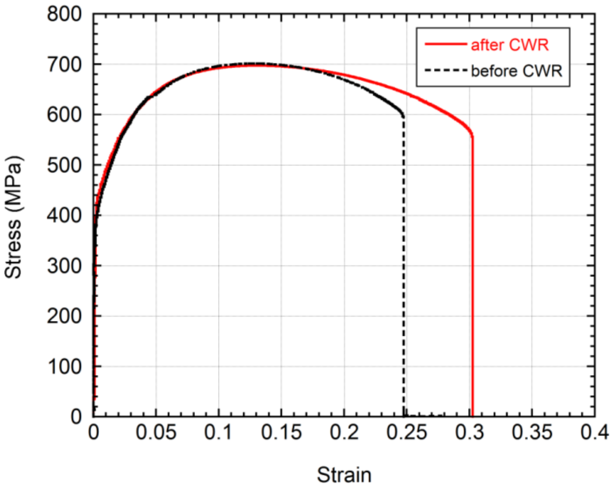

Figure 5.69. Tensile stress-strain curves of 1045 steel workpiece before after CWR.

Ti6Al4V bar used in CWR complied with ASTM F136 standard (Ti6Al4V ELI). The processing route of the bar is shown in Figure 5.70. In the first stage, the material is heated above β transus temperature (963 °C) in order to homogenize the material. In the second stage, the extrusion is performed below β transus temperature. In the last stage, the heat treatment at 700 °C for 1 h is applied. The macrostructure of the bar is shown in Figure 5.71(a-d) along the long axis of the bar (extrusion direction) and normal to the extrusion direction at various magnifications. The lamellar structure is clearly seen in Figure 5.71(b), composing of α (hcp) grains and α (hcp) + β (bcc) grain region. The beta phase is found around the α grains and elongated through the extrusion direction. The size of α grains is around 1-2 μm. The workpiece cross-section after CWR process at 1000 °C and the temperature and equivalent strain distribution are shown in Figure 5.72(a-c), respectively. The grain size greatly increases after CWR as seen in Figure 5.73(a). The grain size increase is also found to be largest in Region 4 since the equivalent strain is the smallest in this region. In the regions of the high equivalent strain, the grains are seen to be elongated normal to the rolling direction. The structure as is expected, after CWR at 1000 °C, transforms from α (hcp) + β (bcc) into Widmanstätten microstructure of colonies of β lathes (bcc and rich in V) and α platelets (hcp and rich in Al) as shown in Figure 5.73(b) and (c). Near the surface of the workpiece, the size and amount of α platelets increase as depicted in Figure 5.73(d). As oxygen is an α stabilizer, after CWR process an α rich region known as α casing forms.

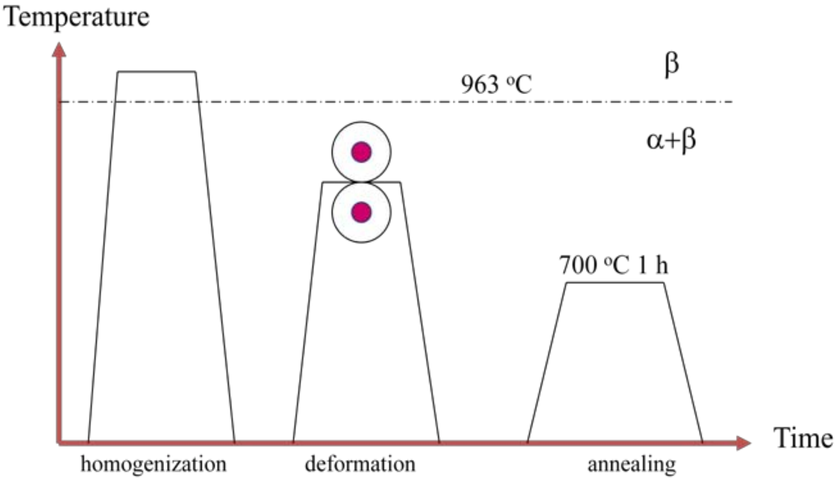

Figure 5.70. The processing route of Ti6Al4V bar.

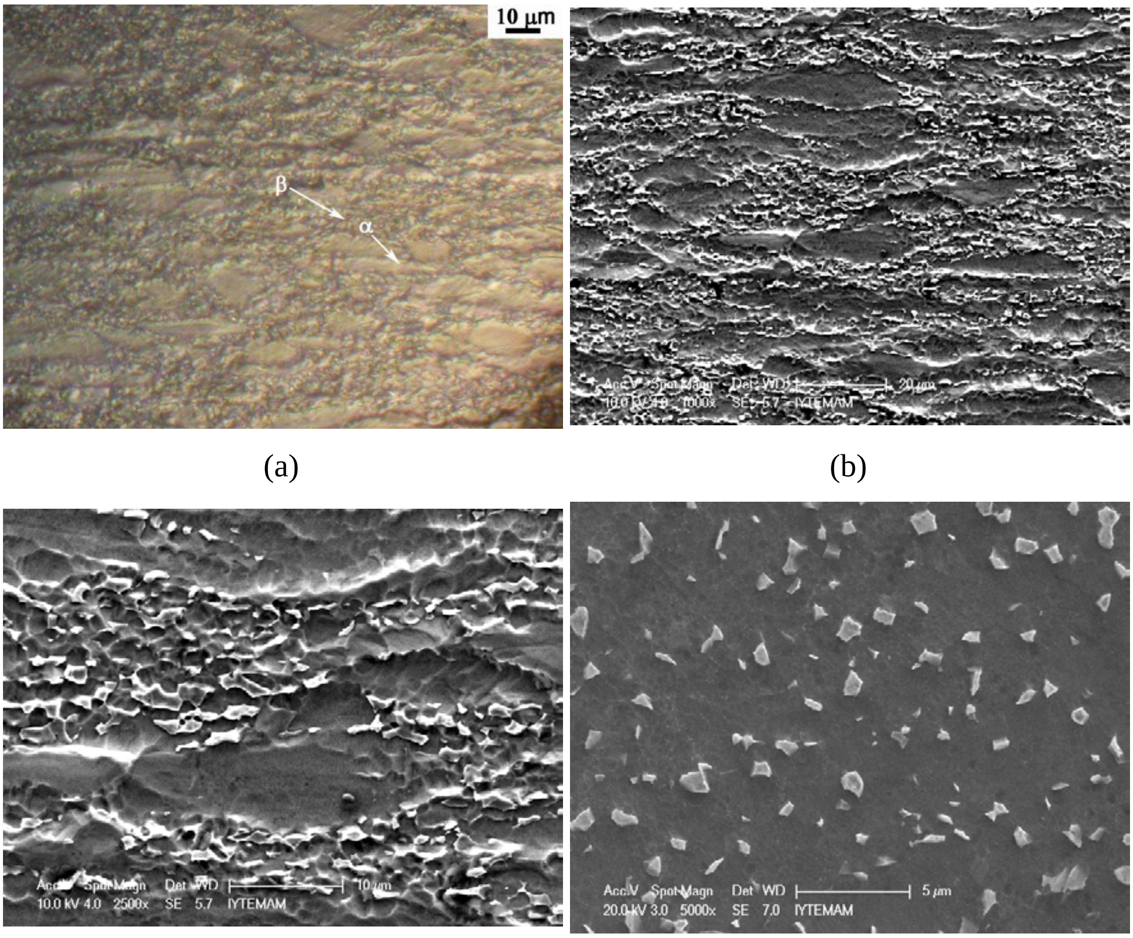

(a) (b)

(c) (d)

Figure 5.71. (a) Optical (and) (b) and (c) SEM micrographs showing microstructure along the bar and (d) SEM micrographs of the microstructure of the bar cross-section (normal to extrusion direction) .

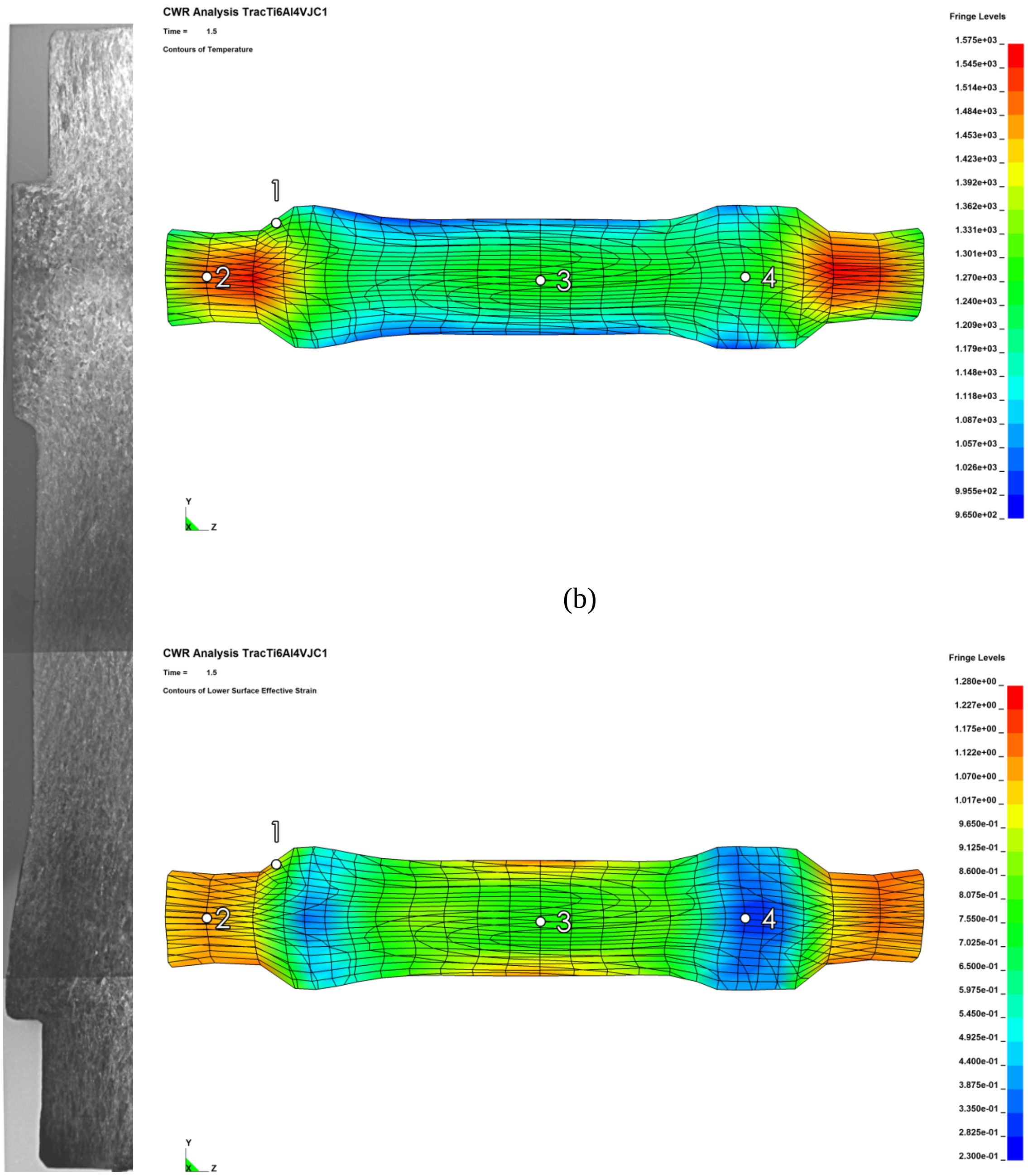

(b)

(a) (c)

Figure 5.72. (a) Half cross-section of Ti6Al4V workpiece after CWR at 1000 °C and (b) temperature and (c) equivalent strain distribution of the workpiece at the end of CWR.

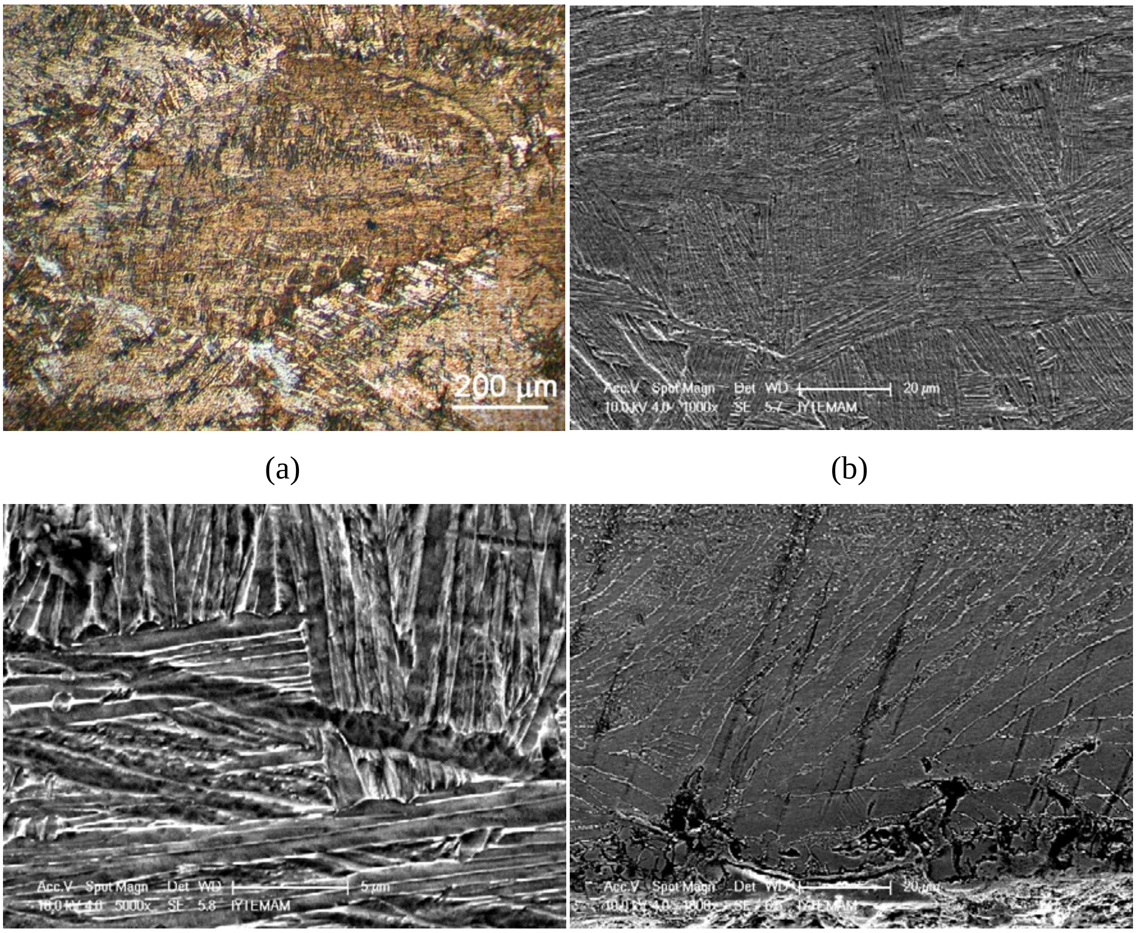

(a) (b)

(c) (d)

Figure 5.73. (a) Optical micrograph showing the grains and SEM micrographs showing (b) Widmanstätten structure, (c) β lathes and α platelets and (d) the microstructure near the surface of Ti6Al4V workpiece.

Figure 5.74(a) shows the microstructure of Ti6Al4V workpiece before CWR at 25 °C, the corresponding microstructure near the shoulder and extension regions are shown in Figure 5.74(b) and (c). The elongated β phase through normal to rolling direction confirms the higher deformability of bcc β phase in extensive deformation regions. The effect of CWR temperature on the microstructure is shown in Figure 5.75(a-d). As the CWR temperature increases, the size of the β phase increases which likely to increase the deformability of the work piece.

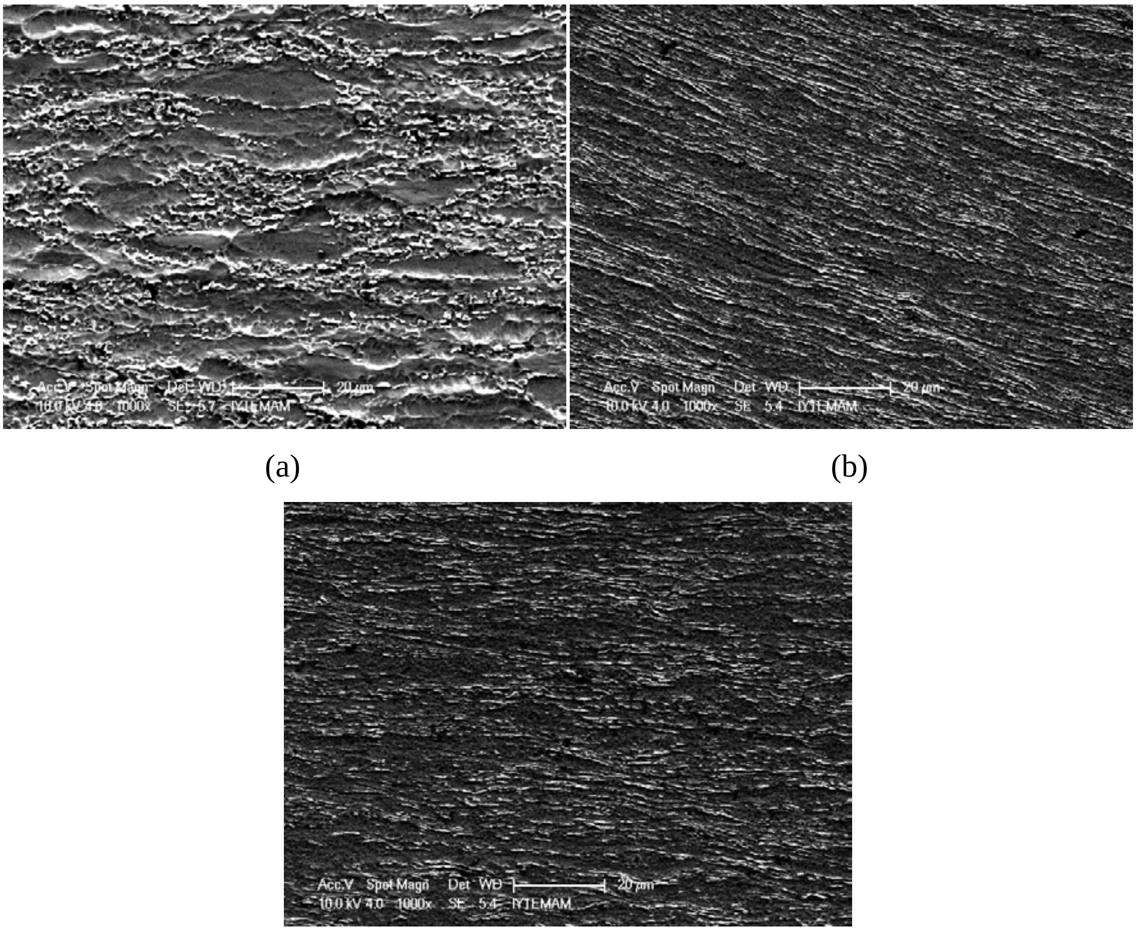

(a) (b)

(c)

Figure 5.74. The microstructure of Ti6Al4V (a) before and (b) after CWR at 25 C near the shoulder region and (c) in the extension region (white regions are β phase).

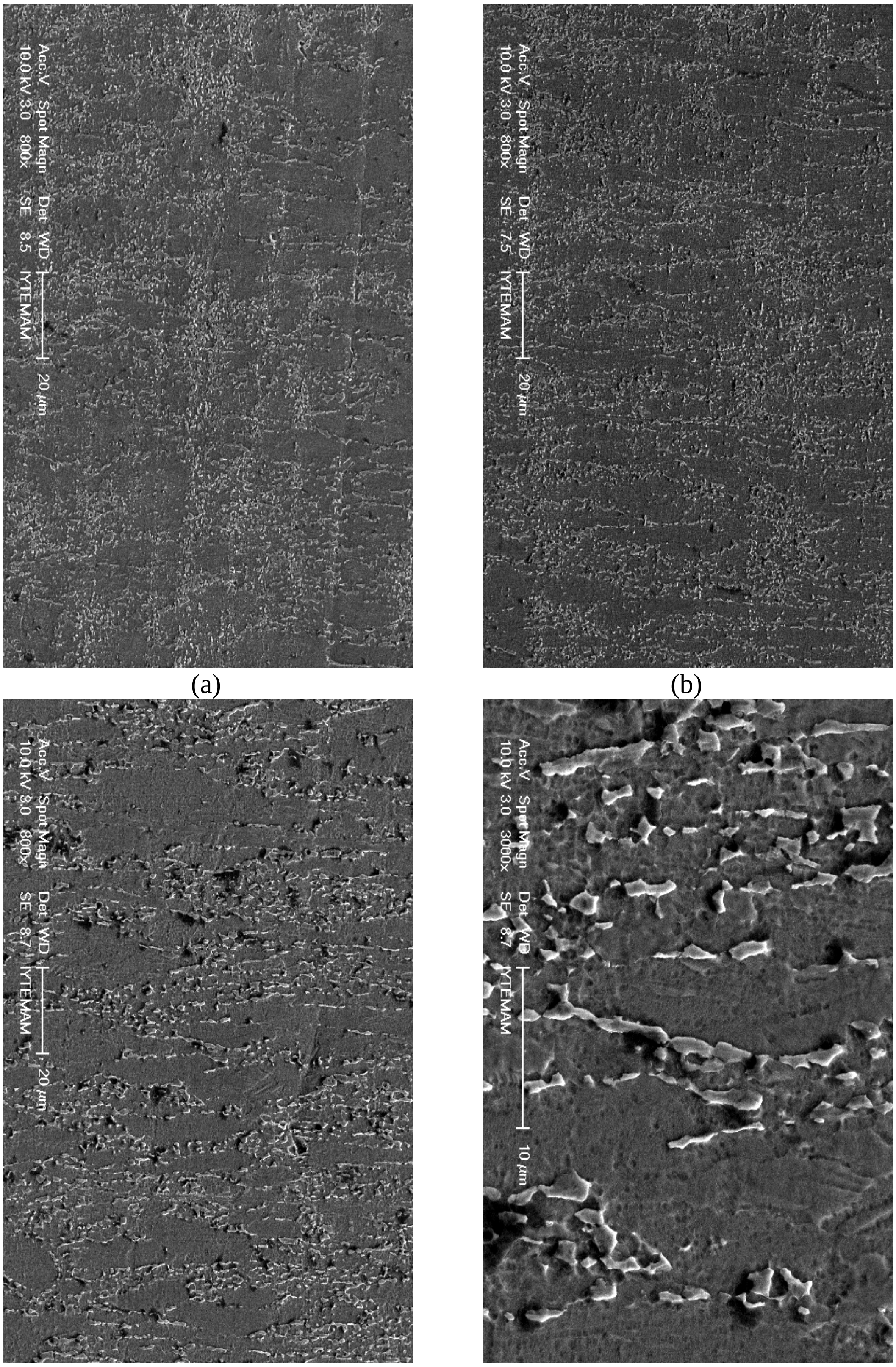

(a) (b)

(c) (d)

Figure 5.75. The microstructure of Ti6Al4V after CWR in the extension region at (a) 25, (b) 500 and (c) and (d) 750 °C (white regions are β phase).

5.5. Effect of Tool Velocity on Damage

The effect of the tool velocity (0.107, 0.215 and 0.422 m s^{-1}) on internal void formation of Ti6Al4V workpiece is investigated. The effective strain and stress triaxiality on the yz cross-section of the workpiece at the same deformation position are shown before and after fracture are shown in Figure 5.76(a-c) and Figure 5.77 (a-c), respectively. With increasing tool velocity, the fracture formation position on the tool decreases (Figure 5.78). The main reason for that is the increased stress triaxiality with increasing strain rate, leading to earlier fracture formation.

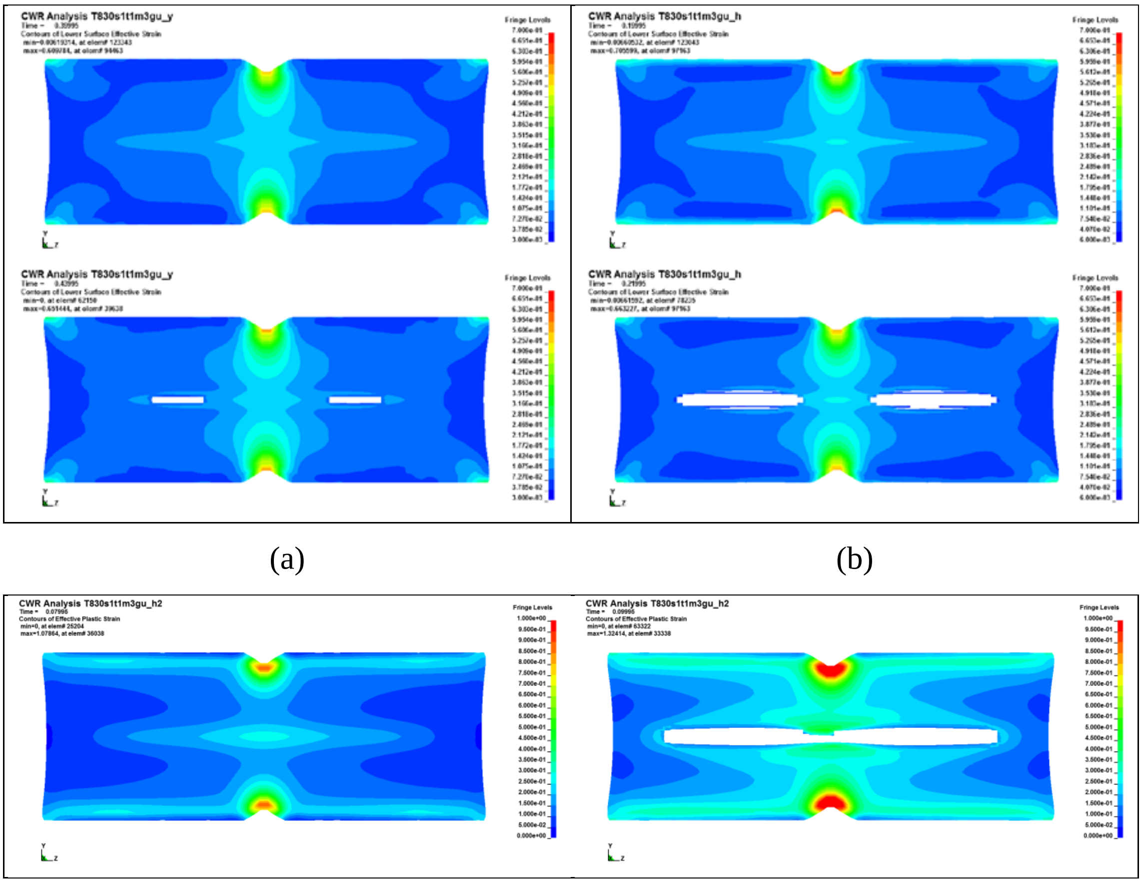

(a) (b)

(c)

Figure 5.76. The effective strain distribution and void formation at the tool velocity of (a) 0.107 m s^{-1}, (b) 0.215 m s^{-1} and (c) 0.422 m s^{-1}.

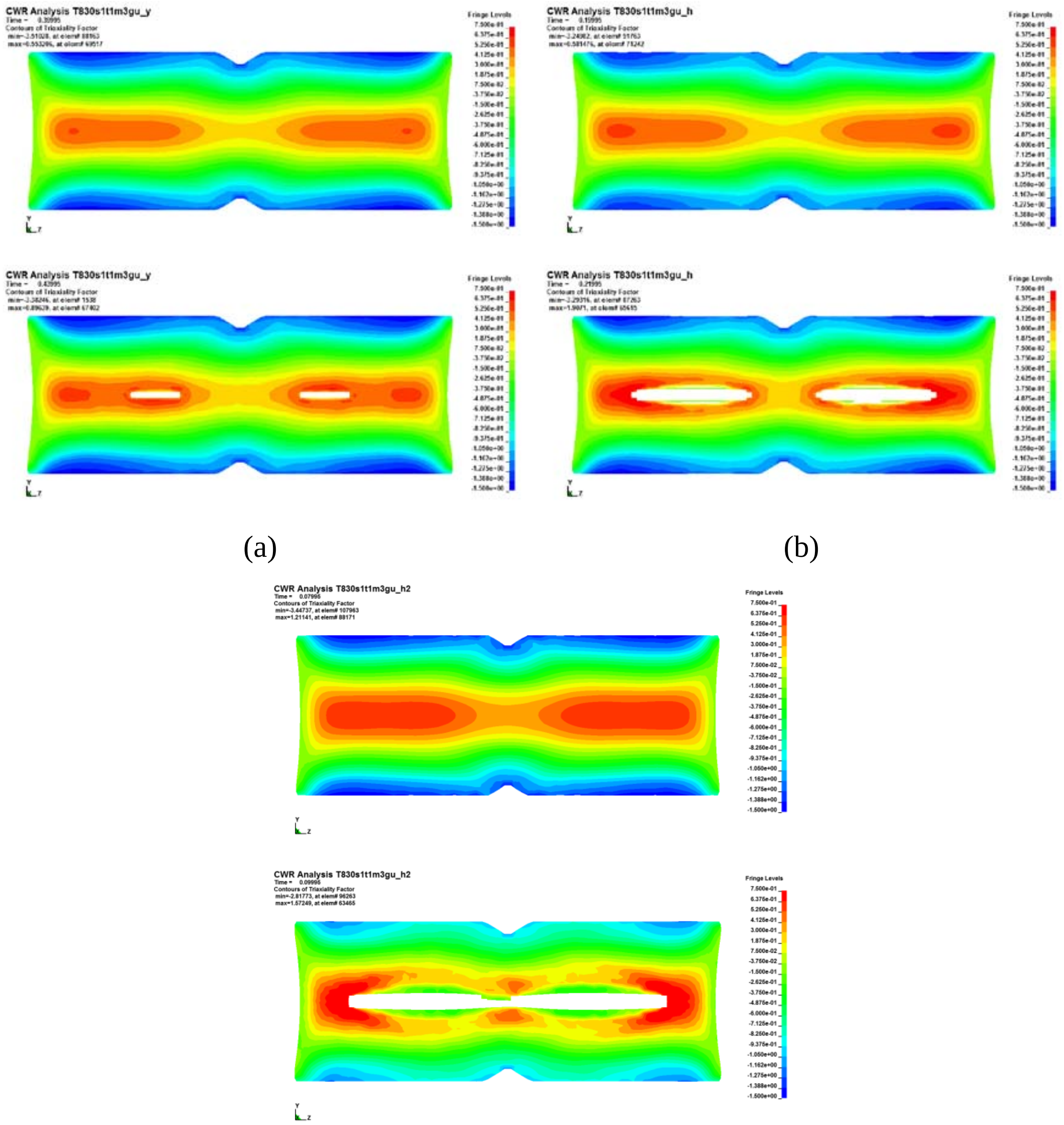

(a) (b)

(c)

Figure 5.77. The stress triaxiality distribution and void formation at tool velocity of (a) 0.107 m s^{-1}, (b) 0.215 m s^{-1} and (c) 0.422 m s^{-1}.

Figure 5.78 shows the stress triaxiality counters at the middle cross-section of the workpiece at various rolling times at different tool velocities. A major crack is seen to form in the maximum stress triaxiality at t=0.52 s for V_{tool}=0.107 m s^{-1} t=0.24 s for V_{tool}=0.215 m s^{-1} and t=0.1 s for V_{tool}=0.422 m s^{-1}. This crack elongates in a direction normal to the maximum stress triaxiality due to the tensile stresses. The above-explained phenomenon of cruciform shape crack formation agrees with the experimentally observed crack shape in CWR.

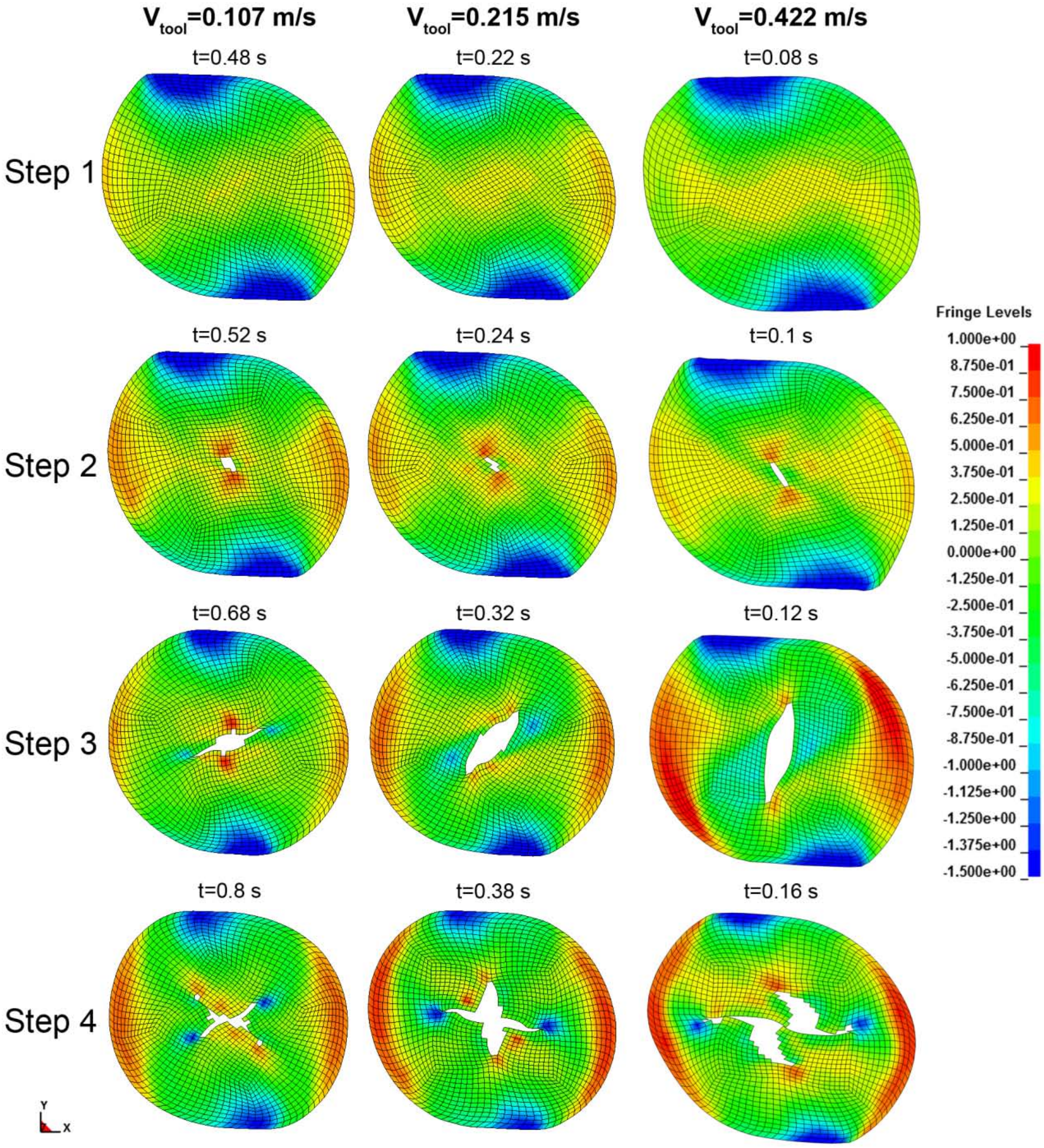

Figure 5.78. The stress triaxiality distribution on the xy cross-section of the workpiece at different steps for two different tool velocities.

CHAPTER 6

CONCLUSIONS

The CWR process was investigated both experimentally and numerically at different initial workpiece temperatures for AISI 1045 steel and Ti6Al4V alloy. The following main results may be emphasized,

1. Although the results of the present FEM analysis were only valid within the studied ranges of the CWR process parameters, the presented thermo-mechanical FEM analysis showed the general trends of the variations of the temperature, effective strain and stress, maximum principal stress, mean stress, stress triaxiality, and strain rate of the workpiece in the high and low temperature CWR of 1045 steel and Ti6Al4V alloy.
2. The present results also showed that the temperature distribution in the workpiece was non-uniform during CWR process. The highest temperature increase was found in the stretching zone, while the surface temperature of the workpiece was higher at the initial region of the deformation and it quickly cooled down as the deformation duration increased. When the initial temperature of the workpiece was relatively low, the workpiece temperature increased during CWR, a heating effect of the plastic deformation, while higher initial workpiece temperatures caused the cooling of the billet. A homogeneous temperature distribution would suffice a homogeneous microstructure of the final product
3. The most significant process parameters on the deformation in CWR were shown, for the studied range of parameters, to be area reduction and β. The effect of increasing area reduction was to increase the tangential force and to decrease the thrust force. It was further noted that the effect of area reduction on the forces was more pronounced in the stretching zone. The increase in β, on the other hand, both increased the tangential and the thrust force. It was also found that in the CWR process conducted at room temperature, the friction coefficient between tool and workpiece increased with the duration of the deformation as the contact surfaces were heated. The friction coefficient

was found not to affect the work piece deformation significantly after a value of 0.3.

4. The failure in CWR was shown to occur numerically in the midsections; the crack formed elongated in a direction normal to the maximum stress triaxiality due to the high tensile stresses, resulting in a cruciform shape crack formation, which agreed with the experimentally observed crack shapes.
5. A cyclic stress triaxiality distribution was found at the surface, while the stress triaxiality distribution at the center was positive throughout the deformation and increased as the deformation progressed. The cyclic nature of the stress was expected to result in axial annular crack at the center of the workpiece as previously shown.
6. CWR process induced a more homogeneous grain size distribution in 1045 steel rolled at elevated temperature, resulting in increased fracture strain. The initial workpiece temperature was found to have a great affect on the final microstructure of CWR Ti6Al4V alloy workpiece.

REFERENCES

[1] Y. Dong, *et al.*, "Analysis of interfacial slip in cross-wedge rolling: a numerical and phenomenological investigation," *Journal of Materials Processing Technology,* vol. 97, pp. 44-53, Jan 2000.

[2] Y. M. Dong, *et al.*, "Analysis of interfacial slip in cross-wedge rolling: an experimentally verified finite-element model," *Journal of Materials Processing Technology,* vol. 80-1, pp. 273-281, Aug-Sep 1998.

[3] Q. Li and M. Lovell, "On the critical interfacial friction of a two-roll CWR process," *Journal of Materials Processing Technology,* vol. 160, pp. 245-256, Mar 2005.

[4] Y. M. Dong, *et al.*, "Analysis of stress in cross wedge rolling with application to failure," *International Journal of Mechanical Sciences,* vol. 42, pp. 1233-1253, Jul 2000.

[5] Q. Li and M. R. Lovell, "The establishment of a failure criterion in cross wedge rolling," *International Journal of Advanced Manufacturing Technology,* vol. 24, pp. 180-189, Aug 2004.

[6] M. T. Wang, *et al.*, "A coupled thermal-mechanical and microstructural simulation of the cross wedge rolling process and experimental verification," *Materials Science and Engineering a-Structural Materials Properties Microstructure and Processing,* vol. 391, pp. 305-312, Jan 2005.

[7] X. T. Li, *et al.*, "The coupling thermal-mechanical and microstructural model for the FEM simulation of cross wedge rolling," *Journal of Materials Processing Technology,* vol. 172, pp. 202-207, Feb 2006.

[8] Y. F. Qiang and P. B. Song, "Analysis on temperature distribution in cross wedge rolling process with finite element method," in *3rd International Conference on Advanced Forming and Die Manufacturing Technology,* Busan, SOUTH KOREA, 2006, pp. 392-396.

[9] Z. H. Hu, *et al.*, "Skew rolling and cross wedge rolling principles, processes and machines," presented at the Metall. Ind. Press, Beijing, China, 1985.

[10] X. P. Fu and T. A. Dean, "Past developments, current applications and trends in the cross wedge rolling process," *International Journal of Machine Tools and Manufacture,* vol. 33, pp. 367–400, 1993.

[11] Z. Pater, "Theoretical method for estimation of mean pressure on contact area between rolling tools and workpiece in cross wedge rolling processes," *International Journal of Mechanical Sciences,* vol. 39, pp. 233-243, 1997.

[12] Y. Dong, *et al.*, "Analysis of interfacial slip in cross-wedge rolling: an experimentally verified finite-element model," *Journal of Materials Processing Technology,* vol. 80-81, pp. 273-281, 1998.

[13] F. Q. Ying and B. S. Pan, "Analysis on temperature distribution in cross wedge rolling process with finite element method," *Journal of Materials Processing Technology,* vol. 187-188, pp. 392-396, 2007.

[14] W. Johnson and A. G. Mamalis, "A survey of some physical defects arising in metal working processes," presented at the Proc 17th International MTDR Conference, London, U.K., 1977.

[15] Q. Li and M. Lovell, "Cross wedge rolling failure mechanisms and industrial application," *The International Journal of Advanced Manufacturing Technology,* vol. 37, pp. 265-278, 2008.

[16] M. Hayama, "Optimum working conditions in the cross rolling of stepped shaft," *Journal of Mechanical Working Technology,* vol. 3, pp. 31-46, 1979.

[17] S. Urankar, *et al.*, "Development of a critical friction model for cross wedge rolling hollow shafts," *Journal of Materials Processing Technology,* vol. 177, pp. 539-544, 2006.

[18] Z. Pater, *et al.*, "Study of the process stability of cross wedge rolling," *Journal of Materials Processing Technology,* vol. 92-93, pp. 458-462, 1999.

[19] H. Tsukamoto, *et al.*, *Advanced Technology of Plasticity II,* p. 936, 1984.

[20] Z. Pater, "A study of cross wedge rolling process," *Journal of Materials Processing Technology,* vol. 80-81, pp. 370-375, 1998.

[21] Q. Li and M. R. Lovell, "The establishment of a failure criterion in cross wedge rolling," *The International Journal of Advanced Manufacturing Technology,* vol. 24, pp. 180-189, 2004.

[22] Q. Li, *et al.*, "Investigation of the morphology of internal defects in cross wedge rolling," *Journal of Materials Processing Technology,* vol. 125-126, pp. 248-257, 2002.

[23] Z. Pater, "Theoretical and experimental analysis of cross wedge rolling process," *International Journal of Machine Tools and Manufacture,* vol. 40, pp. 49-63, 2000.

[24] S. Urankar, *et al.*, "Establishment of failure conditions for the cross-wedge rolling of hollow shafts," *Journal of Materials Processing Technology,* vol. 177, pp. 545-549, 2006.

[25] Z. Deng, *et al.*, "Influence of material properties and forming velocity on the interfacial slip characteristics of cross wedge rolling," *Journal of Manufacturing Science and Engineering-Transactions of the Asme,* vol. 123, pp. 647-653, Nov 2001.

[26] G. Fang, *et al.*, "Three-dimensional rigid-plastic finite element simulation for the two-roll cross-wedge rolling process," *Journal of Materials Processing Technology,* vol. 129, pp. 245-249, 2002.

[27] J. Bartnicki and Z. Pater, "The aspects of stability in cross-wedge rolling processes of hollowed shafts," *Journal of Materials Processing Technology,* vol. 155-156, pp. 1867-1873, 2004.

[28] J. Bartnicki and Z. Pater, "Numerical simulation of three-rolls cross-wedge rolling of hollowed shaft," *Journal of Materials Processing Technology,* vol. 164-165, pp. 1154-1159, 2005.

[29] Z. Pater, *et al.*, "Numerical modelling of cross-wedge rolling process of ball pin," *Journal of Materials Processing Technology,* vol. 164-165, pp. 1235-1240, 2005.

[30] M. Wang, *et al.*, "A coupled thermal-mechanical and microstructural simulation of the cross wedge rolling process and experimental verification," *Materials Science and Engineering A,* vol. 391, pp. 305-312, 2005.

[31] J. Zhao, *et al.*, "Study of stress distribution of forming slandering of automobile semi-axes with multi-wedge rolling by FEM simulation - art. no. 604247," in *ICMIT 2005: Control Systems and Robotics, Pts 1 and 2*. vol. 6042, Y. Wei, *et al.*, Eds., ed Bellingham: Spie-Int Soc Optical Engineering, 2005, pp. 4247-4247.

[32] Z. Pater, "Finite element analysis of cross wedge rolling," *Journal of Materials Processing Technology,* vol. 173, pp. 201-208, 2006.

[33] Z. Pater, *et al.*, "Cross-wedge rolling by means of one flat wedge and two shaped rolls," *Journal of Materials Processing Technology,* vol. 177, pp. 550-554, 2006.

[34] Y. Xiong, *et al.*, "Effect of warm cross-wedge rolling on microstructure and mechanical property of high carbon steel rods," *Materials Science and Engineering: A,* vol. 431, pp. 152-157, 2006.

[35] P. W. Bridgman, *Studies in large plastic flow and fracture*. Newyork: McGraw-Hill, 1952.

[36] E. Kiranli, Izmir Institute of Technology, 2009.

[37] A. M. Handbook, vol. Vol. 14: Forming and Forging ASM International, Metals Park, OH.

[38] J. O. Hallquist, *LS-DYNA Theory Manual*. Livermore: Livermore Software Technology Corporation (LSTC), 2006.

[39] *LS-DYNA Keyword User's Manual* vol. II: Livermore Software Technology Corporation (LSTC), 2007.